UC Berkeley
UC Berkeley Electronic Theses and Dissertations

Title

Climate change and wildland fire impacts on seasonal snow measurements

Permalink

https://escholarship.org/uc/item/0gw4887f

ISBN

9798288862724

Author

Cowherd, Marianne

Publication Date

2025-05-15

Peer reviewed|Thesis/dissertation

eScholarship.org Powered by the California Digital Library
University of California

Climate Change and Wildland Fire Impacts on Seasonal Snow Measurements

By

Marianne Cowherd

A dissertation submitted in partial satisfaction of the

requirements for the degree of

Doctor of Philosophy

in

Environmental Science, Policy, and Management

in the

Graduate Division

of the

University of California, Berkeley

Committee in charge:

Professor Manuela Girotto, Chair
Professor Scott Stephens
Professor Lara Kueppers
Dr. Andrew Schwartz

Spring 2025

Climate Change and Wildland Fire Impacts on Seasonal Snow Measurements

Copyright 2025
by
Marianne Cowherd

Abstract

Climate Change and Wildland Fire Impacts on Seasonal Snow Measurements

by

Marianne Cowherd

Doctor of Philosophy in Environmental Science, Policy, and Management

University of California, Berkeley

Professor Manuela Girotto, Chair

Snow is a vital water resource, contributing to supply, storage, and predictability for downstream uses. Our ability to track snow changes is linked to our ability to understand and represent the mechanisms behind snow accumulation and ablation as well as our ability to make useful observations. The relationship between measured snow properties and unmeasured snow properties is therefore a crucial gap between the actual water resource present and our ability to make optimal water management decisions. This work addresses the need to understand snow measurements and snowpack processes in the face of two prominent sources of change that challenge traditional snow measurement: climate change and wildland fire. First, I use an ensemble of Earth system models to show global shifts in the frequency, severity, and drivers of snow drought around the world. Warm snow droughts, in which a normal or high precipitation year still leads to a water storage deficit, represent an emerging threat to water management in many regions of the world. Second, I focus on snow droughts in the western United States using dynamically downscaled climate projections. This analysis of higher-resolution model outputs identifies spatial variability in snowpack response to climate change. This finding raises further questions on the use of snow observations at a specific location to predict values at a nearby location, as is traditionally done with snow pillow networks in the US and other countries. The strategic but static locations of snow pillows act as representatives of the state of snow water resources across the regions they are located. However, these locations may not react to climate change in the same manner as unmeasured locations, leading to a paradox: how can we know if the network is representative if we don't measure outside of the network? Third, I model the behavior of the snow pillow networks in the western United States in a future climate projection to estimate how useful traditional measurements will remain in a warmer future. By comparing the skill of models ranging from linear regression to convolutional neural networks and with input data from sparse snow pillow proxies to hypothetical dense snow water equivalent observations, I show the potential for addressing future snow management challenges. In particular, I show that explicit two-dimensional spatial correlations are a key component of successful predictions

under new climates. Finally, I present results from a field campaign in El Dorado County, California, showing that legacy snow course locations respond to fire in ways that are not representative of non-snow-course locations. Together, this work shows that the future of snowpack distributions and measurements will be nonstationary and increasingly driven by temperature rather than precipitation. Short-term change from wildland fire and long-term change from climate change demonstrate the need to adapt how we think about snowpack information, not just snowpack quantity, to disturbance.

Contents

List of Figures

List of Tables

Acknowledgments

"I think Michigan keeps you sane and on an even keel through the ups and downs. In Michigan, I do fireworks, shovel snow, and live life." – Jeff Daniels

I am grateful to my advisor, Manuela Girotto, for her incredible flexibility throughout my meanders in graduate school. Thank you for supporting me in taking so many chances, for many many rounds of feedback, and for always being able to tell me what I needed to hear. My co-advisor, Scott Stephens, provided me with early field work experience in Yosemite and a welcoming experience in the lab to talk about fire every week. Lara Kueppers pushed me to consider plants in all their functions; thank you for the creative and constructive conversations and for my first push into climate science. Andrew Schwartz: thank you for welcoming me at the Snow Lab and for your excitement about studying snow. In addition to my committee, Dan Feldman has been an excellent supervisor and collaborator. Thank you for your attention to detail, excitement about the big picture, and for believing in the science and in me.

Most of this work was done with funding from the Department of Energy Computational Sciences Graduate Fellowship. I am deeply grateful for the opportunities, freedom, and support I received from the CSGF to the staff at the Krell Institute who facilitated this. I received additional support from the H2H8 graduate grant, ESPM starter and summer grants, and the Peder Sather Center. Teaching was a meaningful part of these years; thank you to my co-instructors, teaching supervisors, and the UC graduate union.

My dissertation research explores the impacts of climate change and wildland fire on water. While I am grateful for the opportunity to do meaningful work, I am sad to need to acknowledge the ongoing suffering that the processes described in this work are causing. The people suffering from the effects of anthropogenic climate change and those injured or displaced by the Caldor Fire are unfortunately part of this dissertation; I wish you weren't.

Research is a team sport. One of my favorite parts of graduate school was assisting with other people's field projects. Zack Steel, Gabrielle Boisramé, and Gabe Lewis let me tag along to the Illilouette and were always available for an *in situ* ecohydrology discussion. Thank you to the SnowEx Albedo group for teaching me to use a field spec and get a snowmobile out of a tree well. To my labmates and work friends, Will Rudisill, Andrew Johnson, Sabrina Chui, Ann Scheliga, Eric Romero, Fatemeh Zakeri, Carlos Wang, Gaby May Lagunes, Chloe Faehndrich, Mel Baldino, Stefano Casirati, and Grace Carlson: I have learned so much from you and I'm looking forward to many more years of projects together. Ruby Leung, thank you for guiding me through a summer of learning about how we actually do and interpret climate modeling. I feel extremely fortunate to have landed at the Central Sierra Snow Lab for so many years and it is the people, of course, that make a place what it is, and at CSSL that means Andrew Schwartz and Megan Mason, who are excellent snow scientists, field buddies, and friends beyond that. Thank you to Stefan Rahimi for teaching me about downscaling and for your endless positivity. Grazie mille to Marco Mazzolini, for taking me up, down, and around Norway and for the thankless tasks of lidar and workshop (co)registration. I would not have even tried to go to graduate school if it weren't for

mentorship from Inhan Lee, the first person who believed I was a scientist; Galen Egan, who taught me how to do research and is a great friend to boot; and Oliver Fringer, who always pushed me to aim high.

Soccer is also a team sport and a great source of joy for me during graduate school; thank you to Women et al., Muppets FC, SLAY, Real Madrid, and Furnace Fingers. Grayson Melby spent more time in the snow with me than anyone else, for work and fun and in all kinds of weather and terrain – thank you for always sending the spicy parts first. Thank you to Aliza Beverage, Marissa Brown, Nick Choksi, Saher Daredia, Massimo Pascale, Emma Turtelboom, Chris Leboa, Kareem El-Badry, and Sara Tabin for making Berkeley and Pasadena feel like home. My parents, Anne Heise and Doug Cowherd and sister, Allison Cowherd, are the best family in the world. Finally, an infinite thank you to Isaac Malsky for your years of support, kindness, and humor, and for being the person that you are.

Chapter 1

Introduction

"All things are from water and all things are resolved into water." - Thales

1.1 Motivation

Climate change is impacting our water resource systems by changing how, where, and when precipitation falls (Trenberth, 2011); the effectiveness of water storage (Brekke et al., 2009); and the accuracy with which we can assess water resources (Cowherd et al., 2024). Snow is a crucial component of the water supply and storage system, accounting for over 70% of the fresh water resource in the Western United States (Li et al., 2017) and providing trillions of dollars of value to agriculture and urban systems worldwide (Sturm et al., 2017). In most places with significant snow-driven water supplies, the storage capacity of snow is historically much larger than that of human-constructed reservoirs, all without construction or maintenance cost (Mankin et al., 2015) or the environmental tradeoffs associated with constructed reservoirs. As global temperatures rise, snow volumes are declining (Aragon & Hill, 2024; Cowherd et al., 2023; Gottlieb & Mankin, 2024; Hale et al., 2023), decreasing in variability (Marshall et al., 2019), yielding less streamflow forecasting predictability (Livneh & Badger, 2020), and becoming less predictable from current observational networks (Cowherd et al., 2024). Low, variable, and unpredictable snow means that not only are we threatened by under-supply of fresh water from snowpack, but we also may become worse at managing the snow resource we do have in future climates.

Water-related decision making, primarily by undertaken by government agencies, relies on accurate and interpretable snow information. This entails synthesizing ground-based observations of snow depth and water equivalent with satellite and reanalysis estimates of weather variables through empirical, process-based models to produce streamflow forecasts. The observation-to-management pipeline requires an understanding of the processes that drive snowpack accumulation and ablation as well as the scales of variability in time and space. Any underlying change to components of this pipeline, especially in decades-long snowpack statistics (i.e., snow droughts) and the relationship between point measurements

and unmeasured surrounding conditions, is a threat to our ability to make accurate water management decisions.

1.2 Background

1.2.1 Snow measurements

Snowfall and subsequent evolution of snow on the Earth surface produce the snowpack we observe at a given point in space and time. The primary properties of a snowpack that are important for hydrology and climate forcing are fractional snow-covered area (fSCA), albedo, snow depth, and snow water equivalent (SWE). These properties vary greatly in observability and are therefore reported at vastly different scales and resolutions. All snow property retrievals are affected by counfounding factors in sensor observations, including atmosheric property heterogeneity, slope angle effects and terrain shading in complex terrain, vegetation, and signal-masking in the passive microwave range by liquid water in the snowpack. These interferences vary significantly in space and time: atmospheric models are calibrated at low elevations and require updates for mountain regions, slope effects are more meaningful in mountains, terrain shading depends on the look angle of a satellite relative to the relevant features, canopy cover is highest at mid-latitude and -elevation while tussocks impact snow depth estimates in tundra regions, and wet snowpacks are more common in local springtime at low-latitude and -elevation.

In general, fSCA is the most straightforward to observe using multispectral remote sensing and is therefore the most available snow-related quantity everywhere on Earth, frequently, and at high spatial resolution (Bormann et al., 2018). Albedo is similarly available, but the higher need for spectral precision and high sensitivity to confounding factors make albedo data much more uncertain.

Snow depth requires moving from two dimensions to three, and is therefore more limited in the current technological landscape. Ground based measurements (e.g., depth probes, laser or sonic returns) are accurate, but point-based. Spaceborne lidar (e.g., ICESat-2) provide swaths of depth observations, but are incomplete in space and time and require a coregistration processes that is often challenging or unsatisfactory over complex terrain. Airborne lidar (e.g., Airborne Snow Observatories, Painter et al. (2016)) is more spatially complete by virtue of being closer to the surface, but is limited to infrequent retrievals over select US basins. Emerging global, gridded, and frequent snow depth efforts (e.g., CSNOW, Lievens et al. (2021)) rely on microwave-band remote sensing and promise to fill many aforementioned gaps, but struggle with degenerate retrievals under wet snow conditions.

Finally, SWE – the water content of a snowpack and the single most important quantity for snow hydrology applications – remains impossible to directly retrieve from satellites. Ground-based observations remain the standard for high-quality SWE measurements; these typically come from manual measurements of a snowpack or from in-ground scales called snow pillows that report real-time snow masses from strategic points. A global SWE obser-

vation remains elusive; many efforts use a combination of snow depth estimates and ground measurements to provide modeled gridded SWE products.

Many other properties of snow, while not explicitly discussed here due to their smaller impact on water availability, do affect the relationship between depth and SWE (i.e., density), melt speed and variability, and hazard or transport-related snow physics. Snow pits are a traditional method for conducting standardized snow measurements for many purposes. Figure 1.1 shows a snow pit from the UC Berkeley Central Sierra Snow Laboratory in Soda Springs, California, highlighting density measurements using a 10-cm wedge cutter; pits can also include any selection of observations, including hardness, grain size and type, temperature, and layer identification. For each measurement, a sample of snow of known volume is removed from a profile normal to the cut-away surface and then weighed to retrieve the density. There is a finite spatial resolution due to the measurement device and essentially defined by the measurement device. However, cutter-based density measurements are theoretically simple and robust measurements which deliver meaningful information about a snowpack (e.g., vertical variability and total water content).

In the United States, most operational water management in snowy regions relies on information from automated snow pillows installed at strategic locations (Serreze et al., 1999). This network of snow telemetry (SNOTEL) and state-managed snow pillows provides point measurements of SWE that are then used to update local models of basin-wide SWE. These stations, most of which were installed in the 1980s and 90s, were placed to provide insight into interannual snowpack volume variations, not to track the impacts of climate change on snowpack distribution (Montoya et al., 2014). Interpreting network-based observations requires that we place them in statistical context. Nonstationarity fundamentally challenges this (Milly et al., 2008): how can we place new observations in the context of an underlying natural distribution if that distribution is actively shifting? The types of snowpack change we observe and expect from climate change – range shift and altered spatial distributions (Lapp et al., 2005; Mote, 2006) – are not well-observed by point measurements at static locations (Cowherd et al., 2024; Montoya et al., 2014). Our current ability to predict the total volume and sub-basin location of snow, therefore, is limited by our understanding of the drivers of snowfall and the response of snow distribution to climate change.

1.2.2 Change, spatial scales, and nonstationarity

Generally, the larger the distance considered, the higher the inter-annual variability in snow characteristics (i.e., the lower the correlation between annual values). For example, the microtopographical impacts on snow distribution within a single slope are generally present relative to the overall snowfall of the year, as are the moderate-scale impacts of aspect. However, the total snowfall can be highly variable from year to year. From a measurement and observations perspective, these points are extremely important when interpreting observations; we generally expect the relationships between observation sites and the basin as a whole to persist across years and it is therefore notable when this is not the case. Figure 1.2

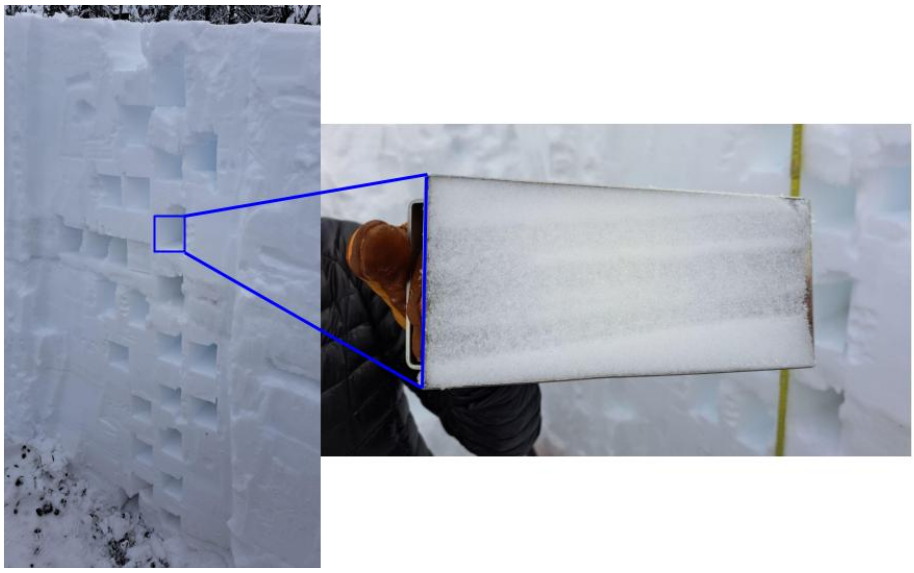

Figure 1.1: A density profile taken in a snow pit at the Central Sierra Snow Lab in Soda Springs, California, USA in winter 2023. The left image shows the entire snow pit with density measurements removed. The right shows one density sample removed, highlighting ice layers within the profile.

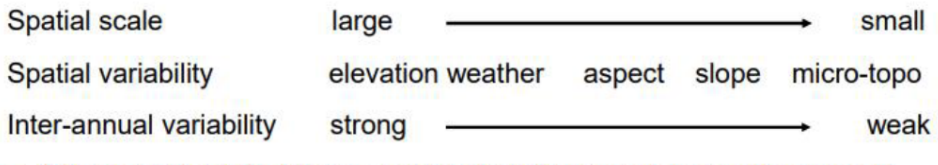

Figure 1.2: The relevant scales of snowpack variation.

summarizes the causes and correlations of spatial and temporal scales of variation commonly observed in snow.

Nonstationarity refers to a system where the statistical characteristics of the distribution (e.g., mean, standard deviation) change (e.g., in time, in space). In hydrology, a meaningful amount of predictability depends on temporal stationarity. That is, the relative values of quantities in a system are preserved when the absolute values change. Stationarity also implies that additional measurements of a quantity bring our understanding of the mean and standard deviation closer to the true underlying mean and standard deviation (i.e., the central limit theorem for normal distributions). In a nonstationary environment, the underlying distribution is shifting while we are taking measurements, so not only will the central limit theorem not lead us to the true mean of the past distribution, but we will also

be unable to observe the mean of the current distribution. Milly et al. (2008) explores the applications of hydrologic nonstationarity through the lens of adapting water management to climate change and human development and elucidates the need for a "successor" framework within which to manage water in the future.

In this dissertation, I address nonstationarity through the lens of point-scale snow measurements and their responses to both climate change and local wildland fires. Climate change and fire are substantially different in their temporal and spatial scales: climate change acts over decades on the entire global climate system while wildland fires occur in weeks to months within geographically isolated regions of a few million hectares at the very largest. The mechanisms of impact on snow are also different, with climate driving changes in air and land temperature, precipitation, and humidity and fire altering the structural and spectral properties of the land surface and surrounding vegetation. However, the shared challenge of adapting snow measurements to change and the fact that climate change has increased the geographic extent of wildland fires to overlap more with seasonal snow connects them.

1.2.3 Climate change and snow

Despite its immense value, the reservoir service of mountains across the West is under threat from anthropogenic warming and human management decisions. Storing water as snow and ice depends on one primary payment from humans: maintaining sufficiently cold temperatures. Snow is both influenced by climate change and has a strong global climate feedback. Global climate change science depends on accurately understanding the snow albedo feedback in which a biased-high snow coverage in an Earth system model increases the reflectivity of the Earth, which decreases the net radiation into the planet and weakens any warming effect. This in turn makes following years more likely to have widespread snow, completing the feedback cycle. Accurate albedo (and snow cover) estimates are therefore crucial to understanding both the actual and potential warming effects of greenhouse gases in the atmosphere (Hall, 2004).

Changes in snow accumulation and melt under climate change are complicated by contradictory effects: warmer temperatures reduce snowfall fractions and enhance melt, but the higher atmospheric water-holding capacity with warmer temperatures could also increase snowfall rates (Yamada et al., 2014). Further, much of the mid-latitude snowpack that provides water to large population centers is sensitive to storm patterns (Immerzeel et al., 2020). Climate-driven circulation shifts could cause changes in snowfall that are not predictable from local temperature (Henderson et al., 2018).

April 1, traditionally a sentinel date for interannual comparisons of SWE and a standard benchmark for operational water supply predictions in the US, now underpredicts peak SWE in most American basins (Bohr & Aguado, 2001). Rain-on-snow and mid-winter melt periods, once rare, are now common enough to define a new standard for the shapes of SWE time series to include punctuated, sharp losses throughout the winter (López-Moreno et al., 2024; McCabe et al., 2007). A suite of modeling predictions using likely global emissions

scenarios predicts a transition to a new normal of low- to no-snow winters in the Sierra Nevada in the coming 30-60 years (Siirila-Woodburn et al., 2021).

The Clausius-Clapeyron relation describes the increase in saturation vapor pressure with temperature; corresponding observations and theory work have shown a lesser but corollary relationship between temperature and precipitation (e.g., Vergara-Temprado et al., 2021). While phase change dominates long-term trends (O'Gorman & Schneider, 2009; Ombadi et al., 2023), snowfall's response to climate change involves both thermodynamic and dynamic processes (Emori & Brown, 2005), with observations showing locally varied responses (O'Gorman, 2014; Pfahl et al., 2017). For example, in the California Sierra Nevada, winter snowfall occurs primarily through large storms whose characteristics depend on atmospheric circulation patterns - for instance, South Pacific atmospheric rivers bring warmer, wetter conditions than North Pacific storms (Kim et al., 2013). The interactions between the shifting global energy balance and regional weather patterns are location-specific and result in trends observable over the course of decades punctuated by interannual and local variability that may defy overall trends.

1.2.4 Wildland fire and snow

Local nonstationary snowpacks can also occur as the result of discrete disturbance to the land surface, separate from climate or weather variability. These disturbance events, such as drought, bark beetle kill, logging, and wildland fires, have their own drivers and characteristics, but all create situations where the processes within the vegetation-hydrology relationship are meaningfully altered in a specific place over shorter time scales – from years (drought, beetle kill, logging) to months (wildland fire). These events provide a useful complement to climate change when considering changing snowpack patterns and strategies for strategically measuring seasonal snow. In this work, I and collaborators study one wildland fire in the western United State as such a case.

Forests are an integral component of the mountain hydrology system because vegetation and snow interact where they coexist, which is the majority of the seasonal snow zone. Forest-snow interactions are complex and multidirectional; similar tree disturbance scenarios can induce opposite responses in snow distribution, amount, and melt timing (Belmecheri et al., 2016; Gergel et al., 2017). Frequent-fire Western forests are denser than they likely were at any point in history (Bernal et al., 2022; Knight et al., 2022) because of widespread fire suppression, so snow that persists until spring melt is heavily tapped by vegetation before flowing into streams. Warmer temperatures also increase vapor pressure deficit, so more snow sublimates during the winter, the same vegetation mass transpires more water, and more surface and soil water evaporates. This, in the context of increasing frequency and severity of wildland fires (Miller et al., 2009), introduces a major source of uncertainty as to how forests will modulate snow accumulation and ablation in the future (Attiwill & Binkley, 2013; Boon, 2012). Complexity is also an opportunity: forests present a pathway to address threats to snow through wildland fire-oriented research and management (Hanak & Lund, 2012).

Understanding the wildfire-snowpack relationship is crucial to active water management in a future increasingly impacted by climate change (Robinne et al., 2021). Current water distribution decisions are made on incomplete seasonal snowpack information and hydrologic modeling predictions based on landscapes of the past, yet the occurrence of megafires has increased in recent years and is expected to continue to increase (Miller et al., 2009; Williams et al., 2019). Wildfires impact snow hydrology in burn scars, but the behavior of these mechanisms in large gaps and in high-severity megafire gaps likely differs from that in smaller or less-severe fires. In particular, despite accounting for a large portion of the world's burned area, there is a dearth of empirical data on the impacts of large burn scars on snow hydrology, even across well observed mountain ranges such as the Sierra Nevada.

1.3 Dissertation structure

The chapters in this dissertation are linked by a common question: how does nonstationarity in the cryosphere affect human water management?

In Chapter 2, I and collaborators, explore a range of projections for the future of snow drought from CMIP6. Snow drought, a statistical classification of SWE deficit, is a sentinel of climate change's impacts on human hydrology. It is also a lens through which to examine the role of nonstationarity in environmental and climate sciences. We find that the frequency and severity of snow droughts are expected to increase around the world and that the role of temperature (as opposed to precipitation) will increase in turn. Interpreting a temperature-driven snow drought, for example in a year with normal or above-average precipitation, is an emerging climate threat that is only understandable when the storage and climate forcing roles of snow are considered as important independent of total water volume supply.

In Chapter 3, I and collaborators use downscaled climate model data to study how precipitation and temperature drive snow drought in western US mountain ranges at high spatial resolution. In this work, the concepts from Chapter 2 are applied at a sufficiently high resolution as to apply to management-relevant scales. This work finds a higher dependence on atmospheric water supply in leeward slopes, with the strength of this dependence decreasing toward the end of the 21st century. In windward slopes and in end-of-century decades, local temperature is a stronger driver of snow drought. Taken together, these findings signal that the competing effects of warming on snowfall – a decrease from phase change from rain to snow and an increase from higher atmospheric water vapor – do shift toward an unbalance in favor of net lower snow in most regions within the current century.

In Chapter 4, I and collaborators analyze the ability of the current ground-based snow measurement network to represent future snow conditions. As climate change shifts the spatial distribution of snowpack, mostly to higher elevations, but also within elevation bands, the static snow measurement network is less able to provide actionable snow information. However, algorithmic advances, specifically the use of two-dimensional machine learning frameworks, can compensate for this skill loss by learning spatial autocorrelations at multiple

scales. In this chapter, we quantify potential benefits from implementing such algorithms for distributed snowpack prediction.

In Chapter 5, I and collaborators address a much more discrete source of change: wildland fire. In this work, we evaluate results from a field campaign in the Caldor Fire burned area in El Dorado County, California. After the fire, the burned portions of the South Fork American River basin displayed greater sensitivity to both snow accumulation and ablation events than unburned regions, including the unburned snow measurement stations in the basin.

Taken together, these chapters show that change at many scales, from global climate shift to local wildland fire, affect snowpack statistics and spatial distributions. These shifting distributions occur in the context of a static measurement network and an empirically driven decision making context; one or both of these conditions must adapt to the change at hand in order to continue to make beneficial water management decisions. The pace and scale of these shifts will increase in the future and have meaningful local variability. The conclusion summarizes this work and contains remarks on the future of this work. Finally, Appendices A and B contain supplementary materials for chapters 4 and 5, respectively.

1.4 Methodological notes

The phrase "to the best of our knowledge" implies different methods and levels of certainties depending on the scale and qualities — both temporal and spatial — at which we hope to have an answer. In the context of snow, we are able to be the most certain in our answers when we consider the recent past at short time scales and in areas in which we have high-quality field measurements. Time travel, the technical details of which are quite beyond the scope of this dissertation, would allow similar levels of certainty in the distant past. However, at present, we approximate time travel into the past with the ground– and remote–based measurement records those who came before us have produced with the limitations, charms, and quirks of their era. To predict the future, we use large ensembles of simulations, notably the six iterations and thousands of member models, replicants, and scenarios of the Coupled Model Intercomparison Project (CMIP). In this work, Earth System Models (ESMs) participating in CMIP6 are used to approximate current projections of what the future will look like and to estimate uncertainty of that future. This use of multi-model spread to estimate uncertainty combines uncertainty from differences in model mechanics between ESMs with natural inter-annual variability within the model that extends beyond broader climate trends. Further, the specific scenarios selected represent a choice of expected future atmospheric carbon dioxide concentrations as the result of policy decisions, as well as other factors such as aerosol emissions.

Chapter 2

Evolution of global snow drought characteristics from 1850 to 2100[1]

"Getting an inch of snow is like winning 10 cents in the lottery" - Bill Watterson, via Calvin

2.1 Abstract

Seasonal snow is an integral part of the global water supply and storage system. Snow droughts impact ecological, agricultural, and urban systems by altering the amount and timing of meltwater delivery. These droughts are characterized by a lack of on-the-ground snow (snow water equivalent, SWE) that can be caused by low total precipitation (dry drought) or low proportion of precipitation falling as snowfall (warm drought), often combined with an early melt. The standardized SWE index (SWEI) ranks the current status of SWE for a given location compared to a baseline condition and identifies the existence, but not the cause, of snow drought. In this work, we use estimates of SWE, temperature, and precipitation from nine coupled model intercomparison project phase 6 (CMIP6) models to quantify the frequency, severity, and type of snow droughts globally for historical and future scenarios. Compared to a historical baseline (1850–1900) total snow drought frequency more than doubles under socio-economic pathway (SSP)2-4.5 and SSP5-8.5; all of the increase in snow drought frequency comes from an increase in warm droughts. The probability distribution of future SWEI in major snowy basins around the world are likely to be centered on more negative values, which corresponds to more severe drought and, with only moderate changes in distribution spread, more frequent drought. CMIP6 simulations pinpoint snow drought as an emerging global threat to water resources and highlight the need to explore higher resolution future models that better capture complex mountain topography, wildland fires, and snow-forest interactions.

[1]This chapter was published as Cowherd, M., Leung, L.R., & Girotto, M. (2023) Evolution of global snow drought characteristics from 1850 to 2100. *Environmental Research Letters, 18(6)*, 064043. and is reproduced here with permission of the authors.

2.2 Introduction

The direct importance of snow as a water source is concentrated in high-latitude and mid-to-high-elevation watersheds (Barnett et al., 2005) which feed 1-2 billion people (Immerzeel et al., 2020; Qin et al., 2020). In contrast to rainfall, snowfall has a hysteresis between precipitation and runoff, during which it provides two primary services: self-storage of water and indirect global climate control by increasing global albedo and insulating methane-storing peatlands. Estimates of the economic value of snow are on the order of trillions of dollars in the Western United States alone (Sturm et al., 2017).

However, global climate change threatens the future global snow resource by altering precipitation patterns in space and time and by increasing temperature, which shifts precipitation from snow to rain and advances melt timing (Daly et al., 2010; Mudryk et al., 2020; Zhu et al., 2021). Observations of trends to date and modeling of future land-climate interactions demonstrate the threat of climate change to all of the world's major mountain water towers: the Western US (e.g., Cho et al., 2021; Marshall et al., 2019; Rhoades et al., 2022; Rhoades et al., 2018), the Andes (Bozkurt et al., 2018; Rhoades et al., 2022), the European Alps (e.g., Coppola et al., 2018), the Pan-Tibetan Highlands (e.g., Immerzeel et al., 2010; Kraaijenbrink et al., 2021), and the Australian Alps (e.g., McGowan et al., 2018). Models also predict an increase in the interannual variability of the timing of peak snow water equivalent (SWE), which corresponds to decreased consistency in melt and streamflow timing, as well as a decreased ability of water managers to predict season-long water availability (Marshall et al., 2019).

Snow droughts are periods of anomalously low snow defined in relation to local historical SWE volume (Harpold et al., 2017). Snow droughts threaten the water security of snow-fed watersheds around the world by changing the amount and timing of snowmelt (Siirila-Woodburn et al., 2021). In conjunction with low total water supply from a meteorological drought, a snow drought imparts additional challenges by changing the timing of downstream water availability, often advancing spring melt, especially in lower-elevation regions of a watershed (Segura, 2021). Snow droughts may also coincide with and contribute to other types of droughts such as meteorological droughts (i.e., lack of precipitation) and hydrological droughts (i.e., lack of water in a system). However, when compared with other drought types, snow droughts present a unique challenge in that the occurrence of the drought and the impact of the drought may be separated in time. Further, multi-year snow droughts have compounding impacts, and snow droughts interact with other ecological processes, including temperature-mediated evaporation rates and vegetation death from drought and wildland fires (Bales et al., 2018).

Snow drought is the result of the many processes involved in snow accumulation and ablation, making some common metrics for drought, such as total precipitation and soil or streamflow water deficit, necessary but insufficient for identifying snow drought. Understanding the proximate cause of snow drought leads to insight into mechanisms for preventing and managing future droughts. However, precise and unanimous definitions of snow drought, including how to best describe its existence, cause, and impacts, vary between science appli-

cations. Gottlieb and Mankin (2021) conducted an intercomparison of snow drought metrics based on a suite of observational and reanalysis snow products to show differences in identification of commonly used metrics. Namely, while all definitions of snow drought use local SWE as the sole value of interest, some definitions use metrics including peak SWE percentile (Rhoades et al., 2022; Siirila-Woodburn et al., 2021), binary peak SWE comparison to the climatological mean (Dierauer et al., 2019), April 1 SWE comparison to the climatological mean (Harpold et al., 2017), Snow Water Equivalent Index (SWEI) score on the US Drought Monitor scale (Huning & AghaKouchak, 2020), and peak SWE amount and timing (Margulis et al., 2016b; Marshall et al., 2019).

Global observations of SWE from satellite remote sensing are available with global coverage beginning in the late 1980's and regional reanalysis-based estimates are available from the mid 1900s's (e.g., Muñoz-Sabater et al., 2021). From these records, a global trend of increasing snow droughts, especially in some mountainous regions with large agricultural importance, is clear, although there is large variation between high-snow regions (Huning & AghaKouchak, 2020). Extending the observed global spatial variations from the recent past to the modeled future places regional snow drought trends (e.g., Dierauer et al., 2021; Immerzeel et al., 2020; Rhoades et al., 2022; Siirila-Woodburn et al., 2021) in the context of global change.

Observations of snow droughts in the late 1900s and early 2000s indicate three primary categories of snow drought: warm, dry, and warm and dry (Dierauer et al., 2019; Harpold et al., 2017). Warm snow droughts occur when precipitation falls as rain rather than snow and is characterized by low on-the-ground SWE in years or months with non-drought levels of total precipitation (Harpold et al., 2017; Hatchett & McEvoy, 2018). Warm droughts may not trigger drought ratings on standard meteorological drought metrics, such as the Standardized Precipitation Index (SPI). However, more of the watershed's precipitation will run off, infiltrate, or evaporate rapidly after falling, rather than being stored in-place as snowpack until melt, which leads to early flows in streams and increased reliance on dams for storage (Flint et al., 2018). Dry snow droughts occur when abnormally low SWE results from low overall precipitation (Harpold et al., 2017). The snow percentage may be normal or even high, but the overall low total precipitation leads to snow drought. Dry snow droughts are often also identified by SPI and other precipitation–based drought metrics. Defining snow drought is particularly important when comparing classifications from disparate data sources, including satellite observations, *in situ* monitoring, and climate models in the context of known biases and random error.

The global warming trend, particularly the potential elevated warming at higher altitudes (e.g., Palazzi et al., 2019; You et al., 2019), and expected approximately monotonic continuation of that trend into the future provide a clear mechanism for increasing warm snow droughts in the future. The speed of this increase in different regions as well as changing spatial and temporal patterns, however, is uncertain. Identifying the characteristics of the expected drought increase, including spatial patterns, frequency, magnitude, and duration of future snow droughts, lends additional nuance and provides a framework for response to hydrologic change at the level at which it is managed.

In this study, we leverage a suite of CMIP6 SWE simulations (Eyring et al., 2016) to track and describe the emergence of snow droughts around the world in the recent past (1850-2015) and in future (2015-2100) climate scenarios. We apply frameworks for describing warm and dry snow droughts (Dierauer et al., 2021; Heldmyer et al., 2023; Huning & AghaKouchak, 2020) to CMIP6 model outputs and use a multi-model ensemble to track trends in global and regional SWE and identify changes in the frequency and character of snow droughts in major basins around the world.

2.3 Methods

2.3.1 Data

We use CMIP6 climate model data from nine models that provide historical and future simulations under both SSP2-4.5 and SSP5-8.5. The list of models and data citations are in Table 2.1. The historical runs of CMIP6 models simulate global climate variables from 1850 to 2014 using prescribed CO_2 from recorded data and other natural and anthropogenic forcings, and each model is evaluated against relevant observational and reanalysis datasets (references in Table 2.1). Future climate scenarios (from 2015-2100) for each model are forced by CO_2 levels and other forcings from the Shared Socio-Economic Pathway (SSP) standard (Gidden et al., 2019; Meinshausen et al., 2020). The equilibrium climate sensitivity (ECS in Table 2.1) represents the change in temperature predicted from a doubling in the atmospheric CO_2 concentration and can be used to compare climate models. In this work, we use data from two SSPs representing a range of possible future climates: SSP2-4.5 and SSP5-8.5. SSP2-4.5 is an intermediate emissions scenario in which greenhouse gas emissions maintain current levels through 2050 and then decrease. SSP5-8.5 is a very high-emissions, high-fossil fuel development scenario for the global climate that would result in approximately 4°C warming by 2100. Both SSP2-4.5 and SSP5-8.5 contain assumptions about how human activity in the future will impact the global environment; the selection of these two scenarios here explores a range of possible future snow drought conditions and demonstrates the sensitivity of model–generated predictions to these assumptions. To maintain consistency between models, we only analyzed CMIP6 simulations through the end of the century (2100) even if longer-term simulations were available for some of the models.

Kouki et al. (2022) show a wet bias in SWE across the Coupled Model Intercomparison Project Phase 6 (CMIP6) models when compared to satellite and observational data, with large inter-model variance in the size of the bias. Temperature and precipitation bias explain some, but not all of the wet bias in SWE. Despite biases in modeling SWE, the impacts of a warming climate may still be credibly simulated by CMIP6 models because of the established link between temperature and SWE in the historical data. Using absolute measures of SWE combined with relative drought statistics allows the impacts of global change to be examined through comparisons to an established baseline.

For the snow drought analysis, we used monthly values of the standard CMIP6 variables

Table 2.1: List of models used in this study for all variables and all of the historical, SSP2-4.5, and SSP5-8.5 experiments. The model name shown is the full CMIP6 acronym for the specific model version. All model outputs are monthly resolution. [a]Commonwealth Scientific and Industrial Research Organisation; [b]Beijing Climate Center; [c]National Center for Atmospheric Research; [d]National Oceanographic and Atmospheric Administration Geophysical Fluid Dynamics Laboratory; [e]Institut Pierre-Simon Laplace; [f]Japan Agency for Marine-Earth Science and Technology, Atmosphere and Ocean Research Institute (The University of Tokyo), and National Institute for Environmental Studies; [g]Meteorological Research Institute; [h]Joint Weather and Climate Program: Met Office and National Environmental Research Council.

Institution	**Model**	**ECS** [°C]	**Citation**
CSIRO[a]	ACCESS–CM2	3.3	Dix et al. (2019a,b,c)
BCC[b]	BCC–CSM2–MR	4.1	Wu et al. (2018), Xin et al (2019a,b)
NCAR[c]	CESM2–WACCM	5.3	Danabasoglu (2019a,b,c)
NOAA[d]	GFDL–ESM4	4.1	Krasting et al. (2018), John et al. (2018a, b)
NOAA	GFDL–CM4	5.0	Guo et al. (2018a,b,c)
IPSL[e]	IPSL–CM6A–LR	5.0	Boucher et al. (2019a,b, 2021)
MIROC[f]	MIROC6	3.7	Tatebe et al. (2018), Shiogama et al. (2019a,b)
MRI[g]	MRI–ESM2–0	4.0	Yukimoto et al. (2019a,b,c)
JWCRP[h]	UKESM–1–0–LL	5.3	Tang et al., (2019), Shim et al. (2020, 2021)

for SWE ('snw', in kg m^{-2}, equivalent to mm), precipitation ('pr', in kg m^{-2} s^{-1}), and near-surface (2-m) air temperature ('tas', in Kelvin). For each model, we computed the average of all ensemble members available at download time. Intra-model variability of SWE (i.e., the standard deviation of all parallel ensemble runs) of the SWE variable is small relative to inter-model variability (Kouki et al., 2022), long-term trends, and the absolute values of the model results. All model outputs were accessed using `Pangeo` software tools in python and regridded from the native resolution to a 160x320-pixel (1.125–degree) global grid using the conservative regridding algorithm in the `xESMF` package in python. Native resolution of model outputs varies slightly between models.

2.3.2 Drought definitions

We collate SWE from each of the CMIP6 models listed in Table 2.1 to compute snow drought statistics globally from 1850 to 2100 and under each SSP2-4.5 and SSP5-8.5 for each model individually and compute the multi-model mean. Regions with low (<10 mm cumulative SWE per year) SWE were masked, as were glaciated or ice sheet-covered regions with more than 10 percent land ice covered (from the 'stfgif' variable in CMIP6 outputs). We then calculate SWEI for each pixel to characterize the existence of snow drought in a given location at a given month. SWEI is a statistical metric calculated from monthly SWE values (Huning

& AghaKouchak, 2020):

$$\mathrm{SWEI} = \phi^{-1}\Big[p\Big(\sum_{k=-2}^{0} \mathrm{SWE}_k\Big)\Big] \tag{2.1}$$

where ϕ^{-1} is the inverse normal distribution and p is the Gringorten plotting position (Gringorten, 1963):

$$p = \frac{i - 0.44}{N + 0.12} \tag{2.2}$$

where i is the ith term in the ranked list of all three-month cumulative SWE summations, and N is the total number of summations in the sample. This produces a scaled value representative of the relative extremity of the snowpack water storage at a given pixel for a given time frame. For further analysis of trends, distributions, and classification, we selected the SWEI for the month of peak SWE for the year for each pixel; all further mention of annual SWEI refers to this. In this study, we construct the plotting distribution with respect to a baseline time period of 1850–1900 for a given pixel, i.e., the mean SWEI in that period is 0 and all other years are relative to that period. The value of SWEI for a year is sensitive to the selection of a baseline time frame; the baseline time frame in this case was selected to illustrate the trend in SWE starting in the 1900's. Acknowledging this non-stationarity permits comparisons on the magnitude and direction of change over time, not the exact predicted values for on-the-ground snow mass.

Classifications of snow drought categories, following Dierauer et al. (2019) and Shrestha et al. (2021) assign a category to a given snow drought. The 3-month cumulative temperature anomaly (anom(T)) and 3-month cumulative precipitation anomaly (anom(P)) are pixel-wise difference from the 1850–1900 monthly mean, where the value for each month is the cumulative sum of the preceding 3-month period. We set -0.8 as the cutoff for defining a snow drought, as in Shrestha et al. (2021) and use sign of (anom(P)) and (anom(T)) to categorize droughts as warm and/or dry:

$$\begin{aligned}
&\mathrm{SWEI}_j < -0.8 \text{ and } \mathrm{anom}(T) > 0. \text{ and } \mathrm{anom}(P) \geq 0. : \text{warm} \\
&\mathrm{SWEI}_j < -0.8 \text{ and } \mathrm{anom}(T) > 0. \text{ and } \mathrm{anom}(P) < 0 : \text{warm and dry} \\
&\mathrm{SWEI}_j < -0.8 \text{ and } \mathrm{anom}(T) \leq 0. \text{ and } \mathrm{anom}(P) < 0. : \text{dry} \\
&\mathrm{SWEI}_j < -0.8 \text{ and } \mathrm{anom}(T) \leq 0. \text{ and } \mathrm{anom}(P) \geq 0. : \text{neither}
\end{aligned} \tag{2.3}$$

For each model, we conduct classification on a yearly basis, using the SWEI, anom(P) and ($anom$)T for the month of peak SWE for each year. This peak annual metric was selected to match the time scale of snow water management while allowing each pixel to have an independent climatology. Classifications are computed separately for each model (i.e., the SWEI computed from a model are classified using that model's anom(T) and anom(P)), and resulting statistics are averaged to produce multi-model statistics.

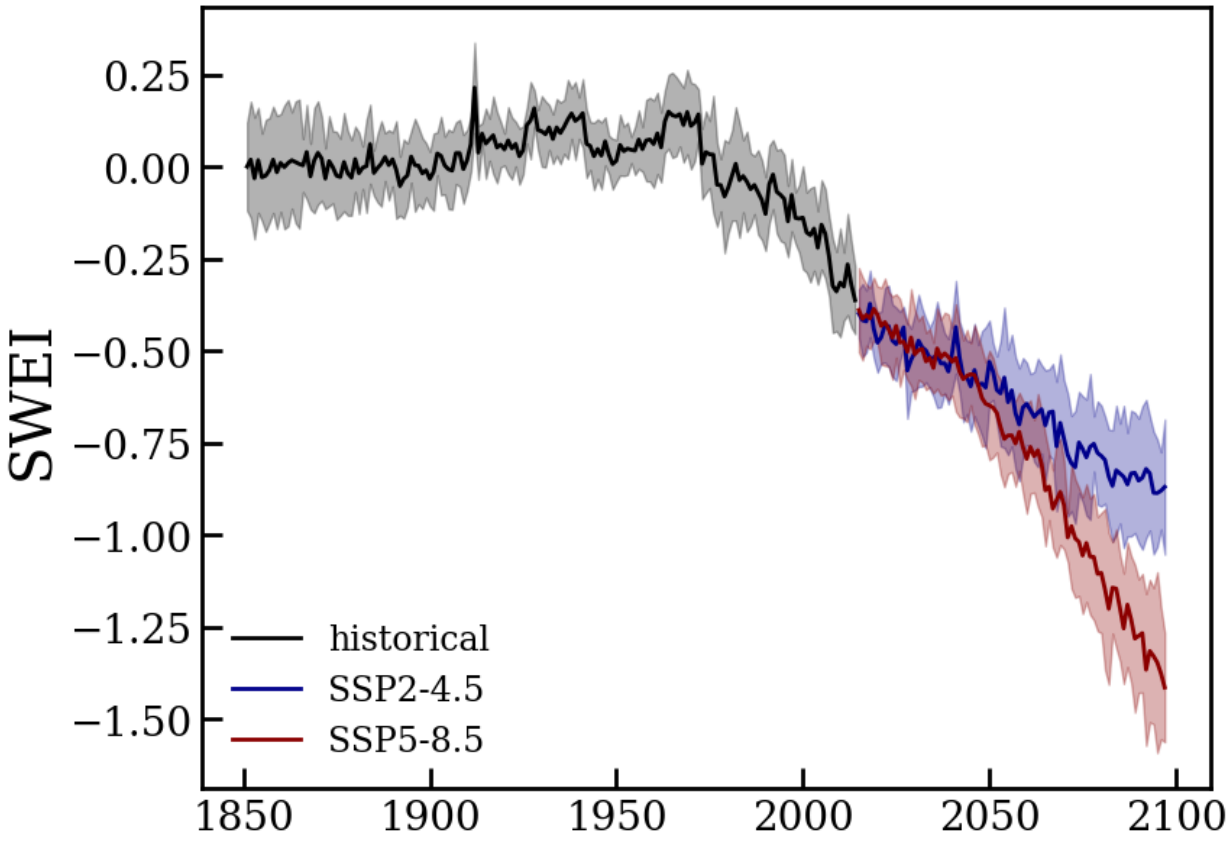

Figure 2.1: Global average snow water equivalent index (SWEI) multi-model mean for nine CMIP6 models for historical (black), SSP2-4.5 (blue), and SSP5-8.5 (red). The 95% confidence interval in the multi-model mean for each experimental era is shaded.

2.4 Results and Discussion

Under SSP2-4.5 and SSP5-8.5, annual SWEI is predicted to decrease and the frequency of snow droughts is predicted to increase in most regions of the world. Figure 2.1 shows the multi-model mean SWEI in historical and future scenarios with 1850–1900 as the baseline distribution of SWE in a given grid cell. The SWEI values within the baseline thus, by construction, oscillate around zero. While both climate scenarios show a continuation of the decrease in SWEI that historical simulations indicate starting around 1980, the two model scenarios diverge in SWEI predictions for the first time around 2040 and continue diverging through the end of the model era in 2100. In addition, global, annual means do not predict snow drought occurrence at a given location or month, but rather predict distributions of SWEI values in the future global climate.

The global SWEI trends in Figure 2.1 have a smaller confidence interval (i.e., more

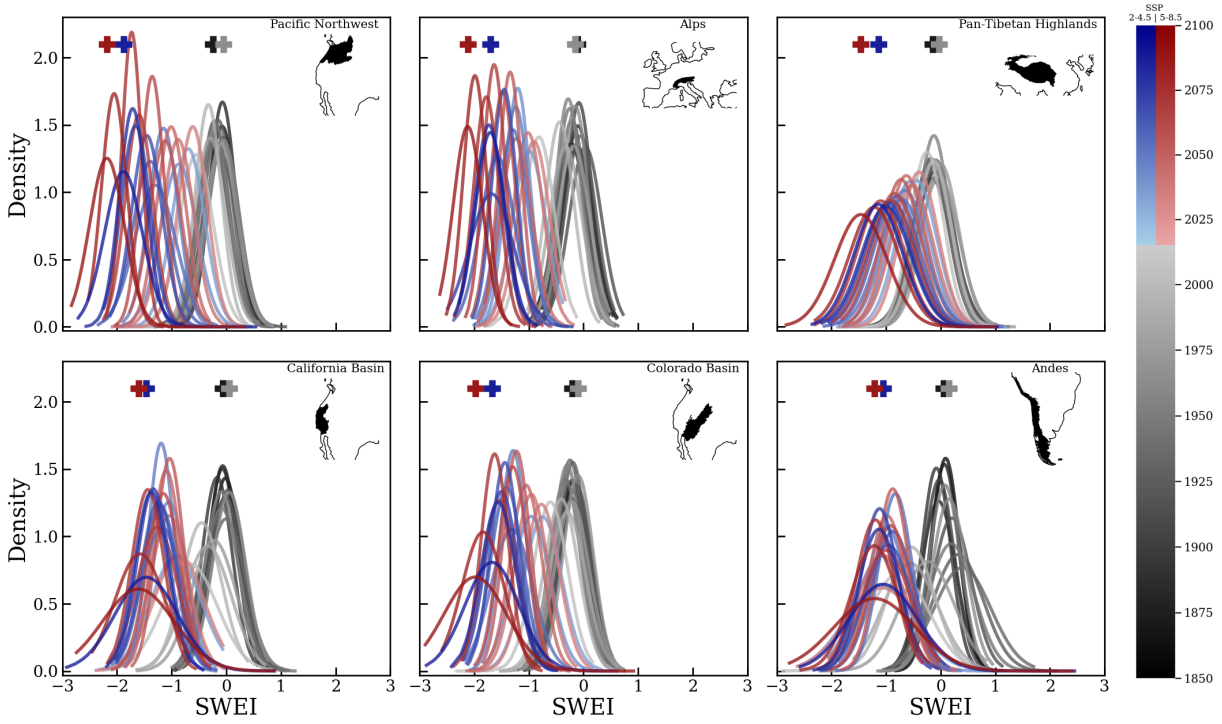

Figure 2.2: Distribution of SWEI in major global water tower basins (maps inset) from the multi-model mean of historical (black, 1850-2014), SSP2-4.5 (blue, 2015-2100), and SSP5-8.5 (red, 2015-2100) simulations. Each distribution is a fitted normal distribution to the values of SWEI for grid cells within the basin for the ten-year period inclusive of the first year and exclusive of the terminal year. The location of the mean of the distribution for the decades that include the end of the baseline period (1850-1900; black), the end of the historical experiment (2005-2015; gray), and the end of the future climate scenarios (2090-2100; blue and red for SSP2-4.5 and SSP5-8.5, respectively) are indicated as crosses above the distributions.

agreement between models) than the SWE values in the models, as the change over time is related to each model's sensitivity to climate in driving changes in snow processes, separate from the time-independent biases known in many models.

Figure 2.2 shows the distribution of SWEI for each decade from 1850 to 2100 in major global snow-dominated basins. There are no major trends over the historical period, as shown by the overlap of black lines in all panels. The mean SWEI values for the end of each time period — baseline, historical, SSP2-4.5, and SSP5-8.5 — are indicated by crosses above the distributions and show a small shift in distributions between the baseline and historical periods followed by significant shifts by end-of-century in future climate scenarios. In all basins, the distribution of SWEI values shifts to a more negative mean in both SSP2-4.5 and SSP5-8.5. Four basins, the Pacific Northwest, Alps, California Basin, and Colorado Basin, show no meaningful change to the width of the SWEI distribution (i.e., standard deviation), while the Pan-Tibetan Highlands show an increased spread and the Andes show a decreased spread. Individual models (not shown) predict similar patterns, but with more variance in the change in width of SWEI distributions.

Figure 2.3 shows averages of snow drought frequency for the Northern Hemisphere and the Andes for the baseline period of 1850-1900 (left) and the change between the baseline and 1960-2010 (center left), 2050-2100 under SSP2-4.5 (center right), and 2050-2100 under SSP5-8.5 (right). The total snow drought distribution (panels m–p) is the sum of the warm (panels 1-d), warm and dry (panels e–h), and dry (panels i–l) columns. The baseline frequencies are shown as occurrence per year of single-year snow drought while subsequent time periods are the difference (i.e., $P(\text{SWEI}< -0.8)_{\text{category},t} - P(\text{SWEI}< -0.8)_{\text{category},baseline}$ for time period t). The frequency of snow droughts is predicted to increase in all snowy regions of the northern hemisphere and the Andes, by an average of 0.31 $\pm$ 0.25 (0.39$\pm$ 0.22, error is the intermodel standard deviation) by 2100 for SSP2-4.5 (SSP5-8.5) compared with the historical baseline. The global increase in snow droughts represents an increase over most of the area of historical seasonal snow, with the notable exception of northeast Asia, which shows a decrease in all forms of snow drought in both future climate scenarios. That region had the highest historical rate of snow drought and is also projected to have increased snow in the future due to precipitation increases and protection from above-0 warming at high latitudes. Finnegan and Miller (2022) found increases in snowfall and snow cover extent between 60 and 70° N in this region in RCP8.5 climate projections, despite general warming trends and threats to permafrost insulation.

The majority (>99%) of this modeled increase is due to an increase in warm drought or warm and dry drought. Dry drought alone is predicted to decrease by an average of 3.2 (3.5)%. Of the increase in drought, 68% $\pm$16 (87 % $\pm$ 22) is attributed to warm drought alone. Warm and dry droughts account for the remaining increase in drought, although the spatial distribution of warm and dry drought is much more varied than of warm or dry drought, with the majority of the warm and dry drought increase occurring in the Alps and parts of the Himalaya, with decreases in northern North America and eastern Asia. The Pan-Tibetan Highlands are the only region to see an increase in dry drought, possibly due to historical very low rates of dry drought. In historical model runs, more than 95% of

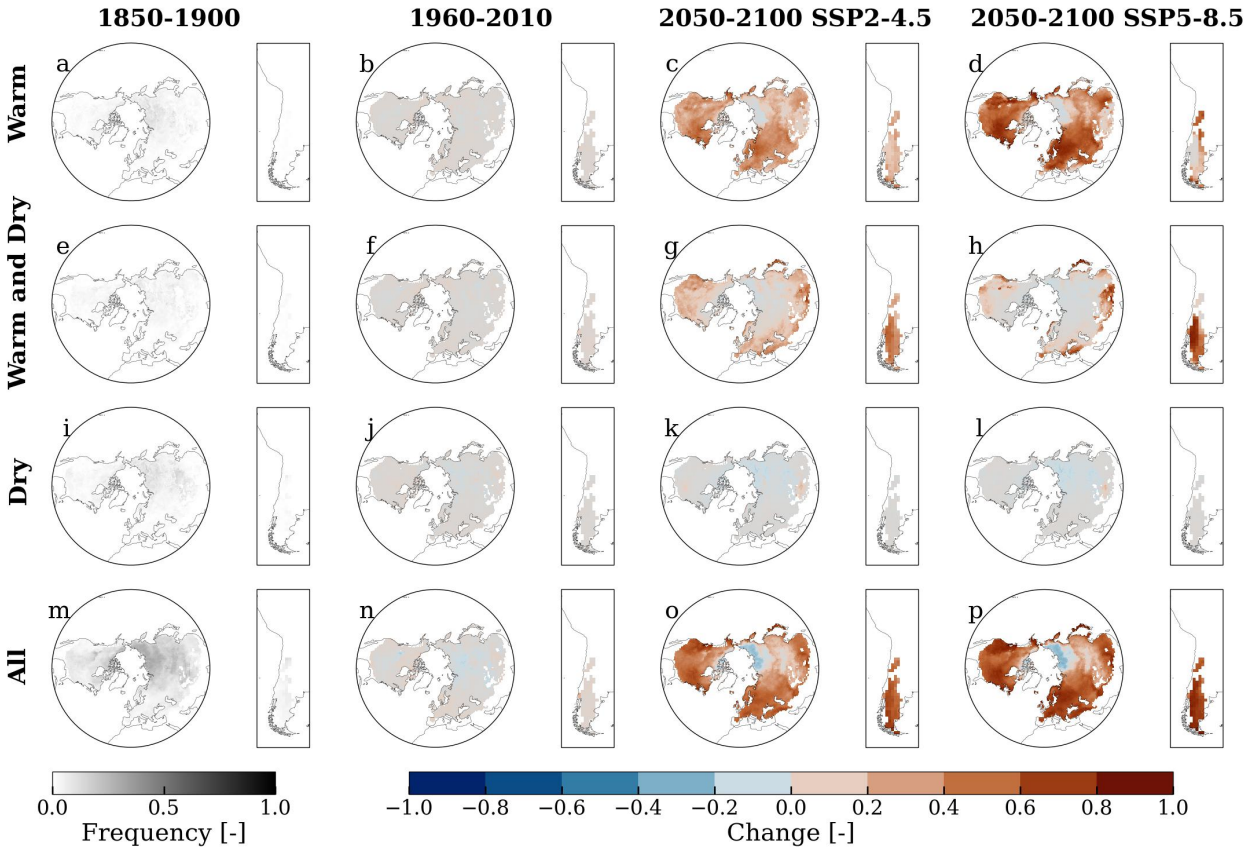

Figure 2.3: Frequency (occurrence per year) for the baseline period (left) and difference from this frequency in 1965-2015 (left center), 2050-2100 under SSP2-4.5 (right center), and 2050-2100 under SSP5-8.5 (right). Each row corresponds to a category of snow drought: warm (a–d), warm and dry (e–h), dry (i–l), and all categories (m–p) from the intermodel mean of snow, temperature, and precipitation as in Equation 2.3. Snow droughts with neither warm nor dry conditions accounted for a small proportion of total snow droughts (<3%) and are not shown.

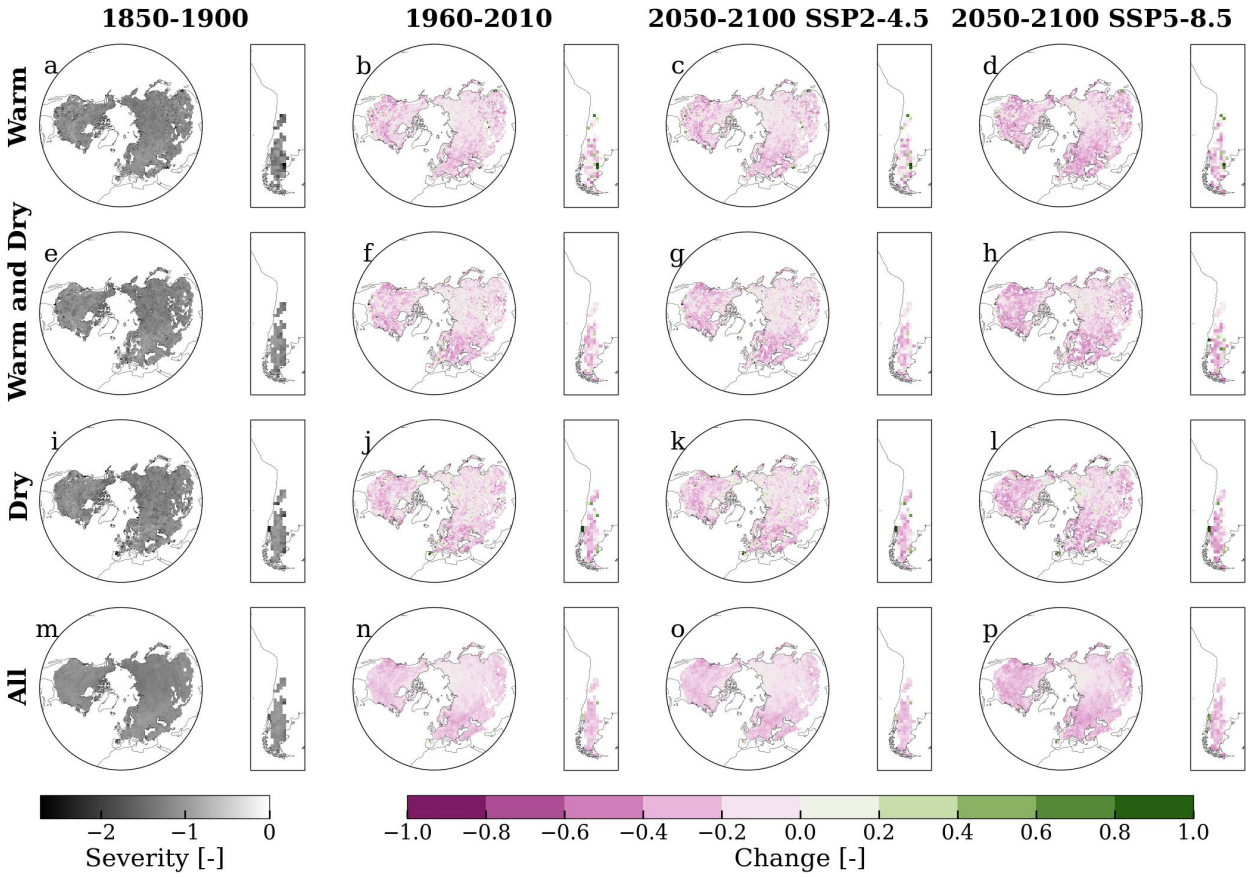

Figure 2.4: Average SWEI of drought years for the baseline period (left) and difference from this in 1965-2015 (left center), 2050-2100 under SSP2-4.5 (right center), and 2050-2100 under SSP5-8.5 (right); i.e., $\text{SWEI}_{\text{category},t}$ – $\text{P(snow drought)}_{\text{category},baseline}$ for each time period t. Negative change (pink) indicates more severe snow droughts in the relevant period than in the baseline period. Each row corresponds to a category of snow drought: warm (a–d), warm and dry (e–h), dry (i–l), and all categories (m–p) snow droughts from the intermodel mean of snow, temperature, and precipitation as in Equation 2.3. Only values that are classified as drought (i.e., SWEI < -0.8) are included.

snow droughts fit at least one of these criteria (i.e., very few snow droughts are in a year which is not anomalously warm and/or dry). The remaining ∼5% occurred in regions with extremely low total snowfall and therefore the drought classification is likely the result of the plotting position method's use of relative ranking, rather than relative magnitude to identify droughts. The largest increases in drought frequency occur in the northern latitudes in the northern hemisphere and in the extreme north and south regions of the Andes. The Pan-Tibetan Highlands, which to date have not had large snow droughts in historical observations or simulations, show more snow droughts in more than half of the years by the end of the century in the SSP5-8.5 scenario. The spatial patterns of frequency increase are consistent between SSP2-4.5 and SSP5-8.5, with a moderate range expansion in SSP5-8.5 compared to SSP2-4.5, especially as both show significant frequency increases in mountainous areas around the world. Work on previous versions of the CMIP6 models used in this study, when used to drive local hydrologic models in the American Southwest (i.e., overlapping the Colorado and California basins) show increases in below–10th–percentile snow years of more than 200% by end of century (Cayan et al., 2010).

Figure 2.4 shows the average severity of snow droughts in the baseline period and the difference between each subsequent time period and the baseline, as in Figure 2.3. Average severity indicates the expected SWEI value for a year given that there there is a drought of the relevant category while frequency (Figure 2.3) implies the probability of drought of the category. Negative change in severity (pink) indicates that the average snow drought is more severe than the average snow drought in the same pixel in the baseline period. Only years in which a snow drought occurs (i.e., SWEI <-0.8 and of the specified type) are included in severity metrics. Snow droughts historically have been approximately equally severe whether dry or warm. Under SSP2-4.5 and SSP5-8.5, warm and warm and dry droughts increase in severity more than dry droughts. SSP2-4.5 shows smaller increases in all parts of the world than SSP5-8.5. Notably, regions with expected increases in frequency (Figure 2.3) show a corresponding increase in severity; these patterns are similar in SSP2-4.5 and SSP5-8.5, but larger magnitude in SSP5-8.5. By end-of-century, the average change in snow drought severity is -0.17±0.32 (-0.79±0.30) in SSP2-4.5 (SSP5-8.5). As with frequency, there is no notable increase in the severity of dry snow droughts but there is an increase in warm and dry droughts and warm droughts, with hotspots in North American mountains and northern latitudes, the Andes, and the Pan–Tibetan highlands, and moderate increases in severity in the Alps. When combined, Figures 2.3 and 2.4 show an increase in the frequency and severity in snow droughts in the Northern Hemisphere and Andes since the 1850-1900 period, with the largest changes in severity and frequency occurring in the same locations. Table 2.2 shows the average of all pixels considered for each panel in Figures 2.3 and 2.4. The relative frequency of snow drought types over time has transitioned from slightly more dry than warm (1850-1900) to slightly more warm than dry (1960-2010), and is predicted to continue to much more warm than dry in both future climate scenarios. The severity of snow droughts of all types is approximately equal, with warm droughts increasing in severity slightly faster than other types.

The coarse resolution of global models precludes sensitivity to local patterns, including

Table 2.2: Frequency and severity of warm , warm and dry, dry, and all snow droughts for each era and experiment shown in Figures 2.3 and 2.4. Neither warm nor dry snow droughts compose a small proportion of snow droughts and are not shown in the table.

	1850-1900	**1960-2010**	**SSP2-4.5**	**SSP5-8.5**
		Frequency		
Warm	0.038	0.041	0.297	0.453
Warm and dry	0.027	0.027	0.120	0.062
Dry	0.043	0.035	0.010	0.002
All	0.133	0.124	0.438	0.519
		Severity		
Warm	-1.200	-1.207	-1.462	-1.478
Warm and dry	-1.203	-1.216	-1.459	-1.437
Dry	-1.218	-1.201	-1.426	-1.385
All	-1.180	-1.179	-1.457	-1.477

fine-scale response to topography within the model. However, multi-scale modeling work has shown that coarse-resolution models generally reproduce regional patterns in precipitation and temperature (Ukkola et al., 2020). Further, SWEI is a relative index, not a predictor of a specific value of SWE on a certain date at a location.

2.5 Conclusions

Global fully coupled models in CMIP6 predict consistently, dramatically decreasing SWEI. In most regions, including the world's major water towers, SWEI distributions were relatively stationary from 1850–1900; satellite and *in situ* data from some of these regions over some time frames supports a general historical stationarity. Since 1950, snow drought severity and frequency has slightly increased and SWEI distributions are predicted to shift further negative, toward more frequent and severe snow drought, in 2015-2100. This trend, while not surprising given the known global temperature increase, motivates the consideration of defining a drought in the context of an evolving baseline. In this study, we put current and future changes in the context of a static historical baseline rather than the moving–window approach that, while frequently used operationally, can obscure long–term trends in favor of highlighting short-term variability (Milly et al., 2008).

Previous work on snow disappearance rates has focused on high-resolution predictions that accurately represent the role of topography in distribution of precipitation and energy transfer. This global, low-resolution analysis contextualizes local predictions in global and regional trends. In particular, the emergence of warm droughts as a dominant snow drought category in most regions of the world in the future indicates that the snow droughts of the future may have different characteristics than those of the past. Historically, snow droughts have been more dry than warm in continental climate zones (Dierauer et al., 2019). In

maritime climates, where the elevation of the snow-rain transition has larger variability, snow droughts have historically been warm or both warm and dry, but at lower frequency than in future predictions. In recent decades, dry and warm snow droughts contribute approximately equally to snow drought frequency in most regions, although warm snow droughts are more severe on average. Under SSP2-4.5 and SSP5-8.5, dry snow droughts are predicted to slightly decrease in most areas while warm snow droughts significantly increase in the majority of the historically snowy areas of the world. This analysis of climate models shows that from 1850 to the present day, snow droughts have shifted from drier to warmer, and that trend is predicted to continue in the future.

Snow drought should be considered parallel to meteorological drought, i.e., meteorological drought can produce snow drought but it is not necessary for snow drought. Meteorological droughts are predicted to increase in CMIP6 simulations with similar trends as the snow drought trends shown here (Ukkola et al., 2020). Warm snow droughts create both a challenge and an opportunity: lack of concurrent meteorological drought may lead to underestimation of the severity of the drought, but the water missing from snowpack is more likely to be locally available than in the case of a dry snow drought. Further, warm snow droughts have been observed to produce lower precipitation–streamflow ratios in the United States (Berghuijs et al., 2014) and Central Asia (Li et al., 2020). The low-precipitation high-temperature conditions that cause warm and dry snow droughts also correspond to more extreme streamflow deficits than either condition in isolation (Dierauer et al., 2018). In other words, snow droughts in the future may be less likely to co-occur with meteorological droughts, but are likely to be more frequent and severe, with potentially higher streamflow impacts. The impacts of climate change on water storage within the hydrological system are many and strong (Christensen et al., 2004). Whether a snow drought is warm, dry, or both, is important in the context of interactions with other types of droughts and therefore the agricultural and societal impacts of drought.

2.6 Open Research

The CMIP6 model results used in this work are available from the Earth System Grid Federation and were accessed using the `pangeo` package for python. The code for this project is available at https://github.com/mariannecowherd/snow_drought.

Chapter 3

Surface and atmosphere drivers of snow drought are topography-dependent[1]

"The object of the engine is in fact to give the utmost practical efficiency to the resources of numerical interpretations of the higher science of analysis, while it uses the processes and combinations of this latter." – Ada Lovelace

3.1 Abstract

In regions reliant on snowfall for water resources, warming temperatures diminish the storage capacity of snowpack, leading to an increased threat of snow droughts. To understand the implications of climate change on snow droughts in the Western United States, we examine nine dynamically downscaled Earth system models at 9 and 45km resolution from 1980 to 2100 to quantify projected snow drought frequency, type, and severity under the SSP3-7.0 scenario. Snow drought frequency increases on average in most parts of the region, with an increasing proportion of snow droughts co-occurring with warm temperature anomalies. However, higher elevation (above 3000 m a.s.l.) regions of the Sierra Nevada show slight increases in peak snow with increases in temperature on the order of centimeters per degree of warming. We use linear models to quantify the sensitivity of modeled snowfall to vapor transport and temperature. Vapor transport is a stronger driver of snowfall trends and interannual variability along eastern (leeward) slopes of the major mountain ranges in the Western United States, while temperature dominates the signal on the western (windward) slopes. Lastly, we show that the regional sensitivity of snowfall to vapor transport decreases and the sensitivity to temperature increases throughout the 21st century.

[1]This chapter was submitted for publication as Cowherd, M., Rahimi, S., Vargas Zeppetello, L., and Girotto, M. in 2024 and is reproduced here with permission of the authors.

3.2 Introduction

The global supply of fresh water for economic and ecological activity is under threat from climate change (Konapala et al., 2020; Vorosmarty et al., 2000). This threat is exacerbated in regions that rely on snowfall for water resources. In many of the most populous and agriculturally active regions of the world, snowpack is an important water storage source (Immerzeel et al., 2010), as a large portion of available freshwater originates as snow and the storage capacity of artificial reservoirs is often insufficient to meet demand (Christensen et al., 2004; Oki & Kanae, 2006; Pedro-Monzonís et al., 2015).

In the Western United States (WUS), snow provides ∼53% of the total freshwater runoff per year (Li et al., 2017) while simultaneously providing natural water storage in winter months. In years of meteorological drought (i.e., low precipitation) snow water storage still provides delayed release of stored water, the effects of which are only sometimes included in other drought metrics (Staudinger et al., 2014). Snow droughts are therefore a critical category of drought to track.

Defining snow drought independently of meteorological or streamflow drought is useful and relevant in snow-fed catchments, as it reflects the expected within-water-year availability of snowmelt. Further categorizing snow droughts by their causes – high temperature (warm), low precipitation (dry), or both (warm and dry) – allows for identification of when snow drought and meteorological drought do or do not coincide and provides insight on the impacts of the snow drought (Cowherd et al., 2023; Harpold et al., 2017; Hatchett & McEvoy, 2018). In particular, warm snow droughts may not be identified as potentially hazardous water resource years by tracking traditional precipitation-dependent drought metrics, such as the standardized precipitation index, but lead to lower than expected snow accumulation and consequently spring and summer streamflow. High precipitation during a warm snow drought can lead to higher risk of rain-on-snow events, which may in turn increase flood risk while complicating spring melt modeling (Andradóttir et al., 2021). López-Moreno et al. (2021) found that snowmelt during rain-on-snow events increases by on average 16% per degree of warming, independent of an increase in the frequency and spatial extent of those events. In contrast, the water management and ecological impacts of dry snow droughts (i.e., through low year-round streamflow, decreased artificial reservoir storage, low soil moisture, and reduced groundwater recharge) are more straightforward to predict than warm droughts, yet difficult to manage (Argus et al., 2017; Dierauer et al., 2019; Harpold et al., 2017). Snow drought years are expected to increase in frequency and severity in future climates, mostly due to rising mean temperatures (Cowherd et al., 2023; Dierauer et al., 2021; Siirila-Woodburn et al., 2021). At the same time, some higher latitudes regions have observed snow increases under recent warming, likely due to increased total precipitation (Box et al., 2019; Cohen et al., 2012).

Snow drought is an inherently heterogeneous, multi-scale problem (Roberts-Pierel et al., 2024; Shrestha et al., 2021). Earth System models (ESMs) primarily run at spatial resolutions over 100 km over land, thus representing the regional conditions that produce smaller-scale, heterogeneous snow droughts and deluges. Especially in the WUS, where most

seasonal snow is found in mountain regions with complex topography, a 100-250 km grid cell cannot represent realistic patterns. For example, the Sierra Nevada rain shadow effect that deposits precipitation from Pacific Ocean-originating atmospheric rivers on the windward (western) slope of the mountain range, leaving the leeward (eastern) side high and dry, occurs on a scale of under 100 km (Leung & Ghan, 1998; Rhoades et al., 2016). This orographic pattern in the Sierra Nevada has already been observed to change as precipitation changes phase due to warming (Pavelsky et al., 2012), but the impacts of even greater climate shifts, such as those expected by the end of the 21st century, are unknown (Hawkins & Sutton, 2011). In addition, snow drought definitions are sensitive to baselines (e.g., pre-industrial, the prior 30 years) and the processes of underlying natural variability at those time scales.

Defining snow drought by peak SWE incorporates both accumulation and ablation and is insensitive to changes in peak timing. However, warmer climates are expected to produce snow time series with many midwinter peaks (Harpold & Brooks, 2018; Marshall et al., 2019), motivating an examination of total snowfall in addition to peak SWE (e.g., Aragon & Hill, 2024; Marshall et al., 2019; Musselman et al., 2017). The increase in saturation vapor pressure is responsible for increased precipitation under climate change scenarios and could lead to a decrease in dry snow droughts, as long as part of the region is below freezing. Warming increases the rainfall fraction of a given precipitation event and the snow-to-rain transition elevation, and could lead to an increase in snow droughts. The potential for warmer climates to increase snowfall (or cold-season precipitation of any phase) has not manifested in observations to date but is projected to appear in the 2060s or beyond in the Western US (Williams et al., 2024), with large variations by region (Krasting et al., 2013) and model uncertainty.

Ensembles of ESM simulations provide a window into the possible climate conditions and dynamics of a future impacted by elevated atmospheric carbon dioxide concentrations. However, most global, long-term Earth system modeling projects contend with irreducible climate uncertainties: internal climate variability, structural uncertainty from different choices within each ESM, and scenario uncertainty from the difference between the hypothesized and actual future (Hawkins & Sutton, 2011). As shown in Hawkins and Sutton (2011), the contribution of each type of uncertainty to projection uncertainty changes with output variable and in time. There is also an inherent computational trade-off between finer spatial resolution and computing expense. Post-ESM-run bias correction is an effective approach to constrain the outputs of global models (Risser et al., 2024); the challenge of resolution can be addressed through downscaling raw ESM outputs. This is generally conducted either by establishing correlations between historical higher-resolution distributions of quantities of interest and their native-resolution ESM counterparts (i.e., statistical downscaling) or by using a ESM outputs to force higher-resolution simulations of a regional climate model (RCM) for a smaller domain (i.e., dynamical downscaling, Ekström et al., 2015). Dynamical downscaling explicitly simulates feedbacks within the model and does not explicitly prescribe stationarity into future experiments (Walton et al., 2020; Xue et al., 2014). Taken together, dynamical downscaling and bias correction are possible and promising methods for preserving the information conveyed by a ESM while attaining high-resolution realism (Wang et al.,

2004; Xu et al., 2021; Zhao et al., 2020).

For snow applications, dynamical downscaling with the Weather Research and Forecasting (WRF) model as the RCM applied to ESMs (Rahimi et al., 2024a) and reanalysis (He et al., 2019; Rahimi et al., 2022) show good agreement, but reflect the known biases of both the ESM and reanalysis products when compared to ground-based measurements (Broxton et al., 2016; Risser et al., 2024). Dynamical downscaling is based on regional climate model dynamics and therefore has the potential to change both the values and trends in a given variable compared to the raw ESM output (Xue et al., 2014). For extreme events, such as snow droughts or deluges (Marshall et al., 2024), both the value and the trend are important in making predictions of future changes based on Earth system models. Future snow drought estimates at low resolution reflect the general atmospheric patterns that typically produce warm or dry snow droughts (e.g., Cowherd et al., 2023). Dynamical downscaling in addition to bias correction is particularly suited to studies of mountainous seasonal snow as hypsometry implies that most midlatitude snowy areas are relatively small in horizontal space (Rahimi et al., 2024b).

In this study, we use dynamically downscaled outputs from an ensemble of WRF simulations to understand high-resolution (45- and 9-km), snow drought predictions for the WUS to address the following questions: How will the frequency, severity, and category of snow drought change in the future based on an aggressive but plausible emissions trajectory? How is snowfall sensitive to temperature change at different starting temperatures? Since temperature can increase atmospheric water vapor capacity and also increase the fraction of rain, how do these effects combine and manifest in models of snowfall and as a function of elevation? In Section 3.3, we describe the downscaled ESM ensemble for four WUS domains and define the snow drought metrics and categories used for the rest of the work. In Section 3.4.1 we explore how snow drought frequency, severity, and type change in future climate scenario under Shared Socioeconomic Pathway 3-7.0 (SSP3). In particular, we compare outputs at various resolutions to understand the sensitivity of snow drought trends to modeled output. In Section 3.4.2, we consider regional and topographical drivers of snow changes in mid-century and end-of-century warming scenarios, including over the Great Basin divide. In Section 3.4.3, we construct a simple model of interannual snowfall variance driven by vapor transport and surface temperature. In Section 3.6 we consider these results and their limitations in the context of previous and potential future work.

3.3 Data and Methods

3.3.1 Data

This study uses the Western United States Dynamically Downscaled Dataset (WUS-D3, Rahimi et al., 2024a), wherein output from an ensemble of nine Coupled Model Intercomparison Project 6 (CMIP6) ESMs have been dynamically downscaled to the Western US with the regional climate model Weather Research and Forecasting Model (WRF, Powers

et al. (2017)). Table 3.3.1 reports each ESM specification used here. Native ESM outputs were bias corrected following Bruyère et al. (2014) as detailed in Rahimi et al. (2024b), in which the ESM outputs are decomposed as a historical climatological mean plus a deviation from that mean, then compared to the same construction from the ERA5 reference of the same output. The monthly difference between the ESM and reference climatological means is considered bias and is removed to produce forcing data for WRF model runs over the WUS. The transient evolution of chemical emissions and land-use/land coverage are implicitly included in the native ESM outputs through their effects on temperature, humidity, and winds. All pre-2015 ESM experiments in this project use historical CMIP6 emissions, while 2015-2100 experiments follow the SSP3-7.0 emissions trajectory. SSP3-7.0 is a scenario introduced in CMIP6 with high aerosols and 7 W m^{-2} radiatie forcing by 2100 due to low-mitigation and increasing CO_2 emissions through end-of-century (O'Neill et al., 2016). The downscaled data set for this scenario therefore represents a range of plausible futures within the SSP3-7.0 framework. Downscaling through WRF produced multiple, higher resolution outputs than the parent ESMs as well as a rich suite of output variables.

The WUS-D3 methodology and snow output have been previously compared to observational and reanalysis data (Rahimi et al., 2024b; Rahimi et al., 2022). These studies found that the 9-km bias-corrected simulations compare well to the snow telemetry (SNOTEL) snow pillow network in the WUS, with only slight offsets in peak amount and melt timing when comparing SNOTEL data to the grid cells that contain the SNOTEL station. We therefore expect the results from these models to represent some of the best available predictions of climate dynamics for the WUS while overcoming some of the known challenges in Earth system modeling, namely wet-bias feedback and problems associated with coarse resolution. While higher resolution products for small regions are available and can be much more closely validated, the full WUS simulations produced from dynamical downscaling allow for a comprehensive comparison across regions of the WUS. Figure 3.1 shows the domains used in this study: a large domain including the entire WUS, parts of Canada and Mexico, and the eastern Pacific Ocean at 45-km grid length and a subset over the continental WUS at 9-km grid length. The two additional subdomains over the US Sierra Nevada and the Middle Rockies, outlined in black, indicate the US Environmental Protection Agency ecoregion boundaries of two mountain ranges studied here in further detail.

3.3.2 Definition of snow drought

We use the Standardized Snow Water Equivalent Index (SWEI) as a metric for the relative SWE condition at a given grid cell in a given year. SWEI, as defined in Huning and AghaKouchak (2020), is a standardization of SWE observations at a location in time that uses an empirical plotting position to represent the relative rank of SWE values. We calculate SWEI on a three-month basis to capture persistence as in Huning and AghaKouchak (2020):

$$\mathrm{SWEI}_i = \phi^{-1}\Big[p\Big(\sum_{k=i-2}^{i} \mathrm{SWE}k\Big)\Big] \tag{3.1}$$

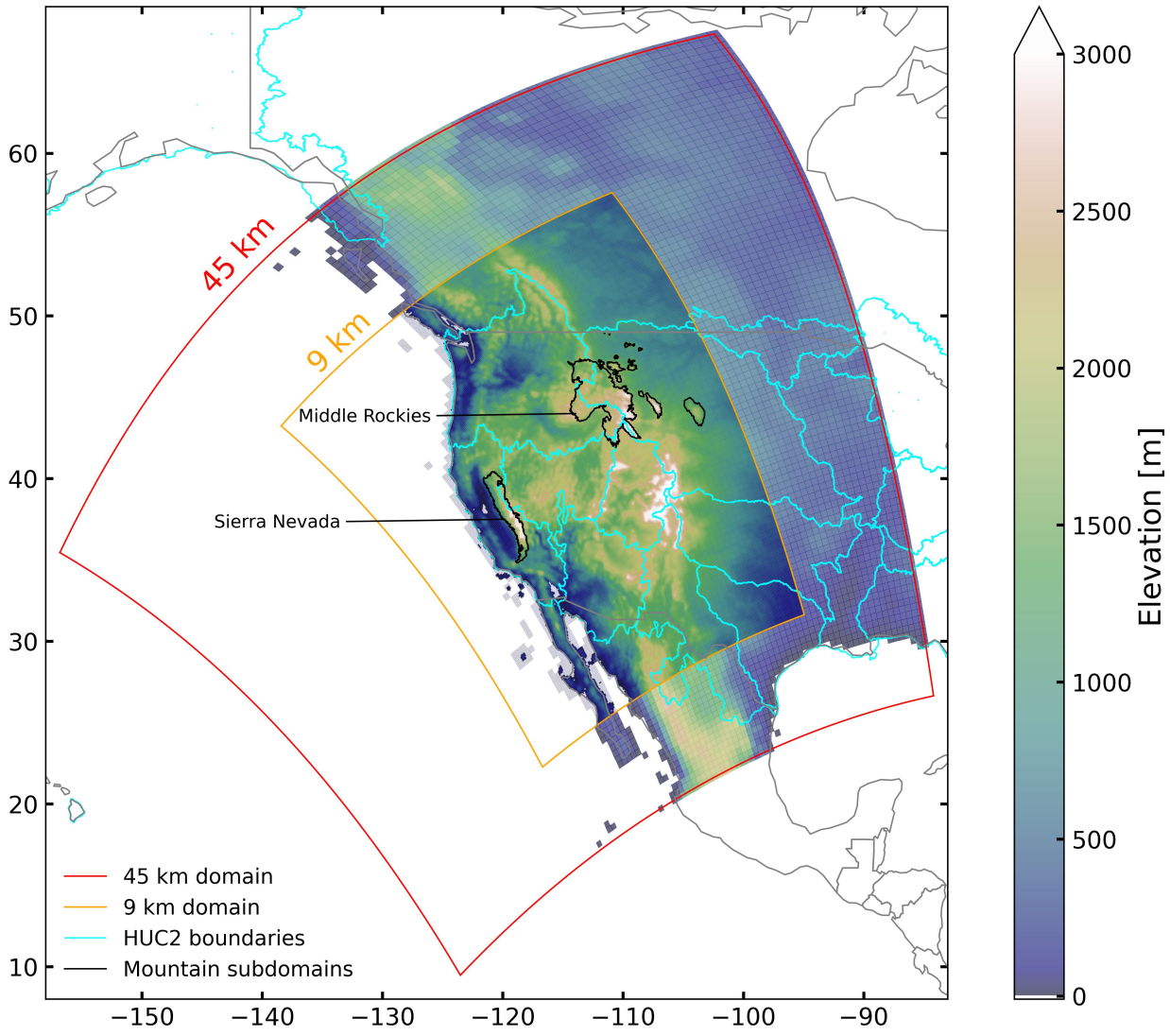

Figure 3.1: Land elevation [m a.s.l.] for the downscaled model domains at the resolution indicated by domain. The 45-km domain (red) encompasses all of the Western United States and portions of Canada, Mexico, and the eastern Pacific Ocean. The 9-km domain (orange) includes the Western United States. Hydrologic Unit Code level 2 basins are overlain in light blue. The Sierra Nevada and Middle Rockies mountain ranges are outlined in black.

Table 3.1: ESM specifications for the ensemble of simulations used in the study. References and resolution reflect the raw ESM runs for historical and SSP3-7.0 from the CMIP6 ensemble and are expressed as latitude-longitude near the equator.

ESM	**Variant**	**Resolution [°]**	**References (historical; SSP3-7.0)**
ACCESS-CM2	r5i1p1f1	1.25×1.25	Dix et al., 2019a, 2019b
CanESM5	r1i1p2f1	2.8×2.8	Swart et al., 2019a, 2019b
CESM2	r11i1p1f1	0.94×1.25	Danabasoglu, 2019a, 2019b
CNRM-ESM2-1	r1i1p1f2	1.4×1.4	Seferian, 2018; Voldoire, 2019
EC–Earth3	r1i1p1f1	0.7×0.7	EC-Earth-Consortium, 2019a, 2019b
EC–Earth3-Veg	r1i1p1f1	0.7×0.7	EC-Earth-Consortium, 2019c, 2020
FGOALS-g3	r1i1p1f1	2×2	Li et al., 2019b, 2019c
MPI-ESM1-2-LR	r7i1p1f1	1.9×1.9	Pongratz et al., 2019; Wieners et al., 2019
UKESM1-0-LL	r2i1p1f2	1.25×1.25	Good et al., 2019; Tang et al., 2019b

where ϕ^{-1} is the inverse normal distribution as a quantile function and p is the Gringorten plotting position, $p = \frac{i-0.44}{N+0.12}$, where i is the i^{th} term in the ranked list of all annual peak SWE values, and N is the total number of years in the sample. We further restrict the SWEI calculations to only reflect the peak SWE volume for a given water year, as in Cowherd et al. (2023) in order to focus on measuring the impacts of winter-season snow processes.

In this study, we use the 30-year period from 1980-2010 as the baseline due to the time period covered in WUS-D3. As the choice of baseline controls all calculated metrics for future droughts, it is important to consider SWEI values as relative to a baseline, not as absolute indicators of what might be considered a drought by any given management agency in the year in which it is reported.

As with the widely used standardized precipitation index that defines meteorological droughts, SWEI cutoffs are used to categorize the existence of snow droughts: SWEI values of less than -0.8 indicate the presence of a snow drought. The frequency of snow drought is the fraction of years in a given time frame with SWEI<-0.8; the value of SWEI is the severity, with more severe SWE deficit indicated by more negative SWEI. Variations in SWEI indicate the severity of a drought in terms of volume of SWE missing, not in storage time; accumulating sequential SWEI values indicate multi-year snow drought. Conversely high positive SWEI values indicate relatively wet SWE years, which can be caused by high precipitation and/or low temperatures (e.g., Marshall et al., 2024).

All snow droughts were categorized as warm, dry, or warm and dry by their co-occurrence with temperature and/or precipitation anomalies from the downscaled outputs, accumulated between October and April of each water year. The precipitation and/or temperature anomaly values were defined as the difference from the average winter cumulative value at that pixel for 1980-2010 (the same baseline as used in the SWEI calculations), for a given ESM. These categories, as qualitatively described in Harpold et al. (2017), indicating the

correspondence between the main meteorological drivers of snow drought (i.e., temperature and precipitation) and on-the-ground snow deficit.

Next, we defined a global temperature change time series using the global mean raw ESM 2-meter air temperature field ('tas'). The change from 1980-2010 baseline in global average temperature was used to normalize changes in peak snow volume and frequency of snow drought per degree of warming. Normalized change per degree of warming allows for inter-decade and inter-SSP comparison of snow changes. However, near-range changes (i.e., before 2040) suffer from near-zero denominator and cannot be examined with this metric; rather, SWEI is more meaningful.

3.3.3 Topographic controls on snow change

In addition to varying in time, snow drought varies in geographic and topographic space. We use the WRF elevation for each resolution to examine geographic variance in snow drought frequency and severity. In particular, to examine how high-resolution future Earth system models, we considered two sub-domains, Sierra Nevada and Middle Rockies, as shown in Figure 3.1. Then, at each grid cell, we compute end-of-century change in peak SWE per degree of global temperature change ($\Delta\text{SWE}\Delta\text{T}^{-1}$) in mm C^{-1}. We then compare $\Delta\text{SWE}\Delta\text{T}^{-1}$ across elevation bands at both 45 km and 9 km resolutions.

3.3.4 Temperature-driven mechanisms of snowfall change

Snow drought trends are driven by both precipitation and temperature anomalies; this is explicit in our snow drought categorization framework. However, the warm vs. dry snow drought framework implicitly combines two mechanisms through which temperature changes snow accumulation: 1) increasing the saturation vapor pressure of the atmosphere, and 2) changing hydrometeor phase from snowfall to rainfall.

We disentangle the contributions of increased temperature to snow accumulation by modeling the dependence of snowfall interannual variability to zonal integrated vapor transport (IVT) and local positive degree days (PDD). IVT, a vector representation of full-column atmospheric water vapor transport, represents the volume of water vapor in the atmosphere as well as its convergence (Rasmusson, 1967). PDD reacts to global warming on large time or spatial scales and represents local weather and topography at the grid cell level.

We use the zonal IVT from the 3-dimensional 'ivt' variable in WRF, approximating the atmospheric water vapor flux convergence. Water-annual wintertime (set to November 1–April 1) PDD sums for each grid cell and represents the local interannual variability in surface temperature. We then fit a set of three linear models for each pixel:

$$SF = a \times IVT + c, \tag{3.2}$$

$$SF = b \times PDD + c, \tag{3.3}$$

and

$$SF = a \times IVT + b \times PDD + c \tag{3.4}$$

where SF is annual snowfall and a, b, and c are fitting parameters. Eq. 3.2 models snowfall as a linear function of IVT, Eq. 3.3 models snowfall as a linear function of PDD, and Equations 3.4 models snowfall as a linear combination of both. We then repeat this process with a detrended anomaly for SF, IVT, and PDD. The normalized detrended anomaly of a term X, indicated X', is computed by first removing a linear trend from the data and then taking $X' = \text{minmax}(X - \overline{X(t)})$ for a given scalar X where $\overline{X(t)}$ is the linear trend of the data and minmax is the rescaling to a range of [0,1]. The trend removal, when applied across the 30-year analysis period, removes the signal from long-term warming, leaving only interannual deviations. Trend removal, anomaly calculation, and linear models are all computed over a moving 30-year window for each pixel individually. We then quantify performance of each model on a pixel-by-pixel basis, within the 30-year time window, with an R^2 correlation coefficient. In each case, the R^2 value represents the fraction of annual snowfall variance that can be explained as a linear function of IVT, PDD, or both combined. In the detrended case, these models only track the interannual variability independent from the underlying long-term trend.

3.4 Results

3.4.1 Temporal and spatial snow drought trends

Downscaled climate simulations across the WUS show increases in snow drought frequency and severity throughout the 21st century. Figure 3.2 shows, for the Sierra Nevada and Middle Rockies regions, the fraction of land area in drought, normal, or wet conditions, averaged between all ESMs used in this study. For each of the 45-km (left) and 9-km (center) grid length ensembles, the proportion of land area in snow drought (red, orange, or yellow) or normal-to-wet (light gray, dark gray, or purple), is shown over the time domain of the model ensemble. The expansion of snow drought categories in later years reflects increasing frequency of snow droughts across the region as well as the expansion of snow drought conditions into new areas. Categorization of snow drought condition follows the SWEI-based cutoffs described in Section 3.3.2, with non-drought conditions split into low normal ($-0.8 < \text{SWEI} \leq 0$), high normal ($0 \leq \text{SWEI} < 0.8$), and wet ($0.8 \leq \text{SWEI}$). This split reflects percentile-based categorization in prior work (e.g., Siirila-Woodburn et al., 2021) while maintaining reference to a drought-specific metric.

In both regions, historical snow drought proportion is, by construction, low at all resolutions. Increases are mostly due to warm and warm and dry snow drought; total dry snow drought area slightly decreases in this time frame. The right column (c, f) for both regions shows the fraction of total snow drought in each category, i.e., the probability that a snow drought is caused by precipitation, temperature, or both given that a snow drought occurs in that year. While the historical fraction of dry snow drought is higher in Middle Rockies than in Sierra Nevada, this value in both regions decreases to near zero at the end

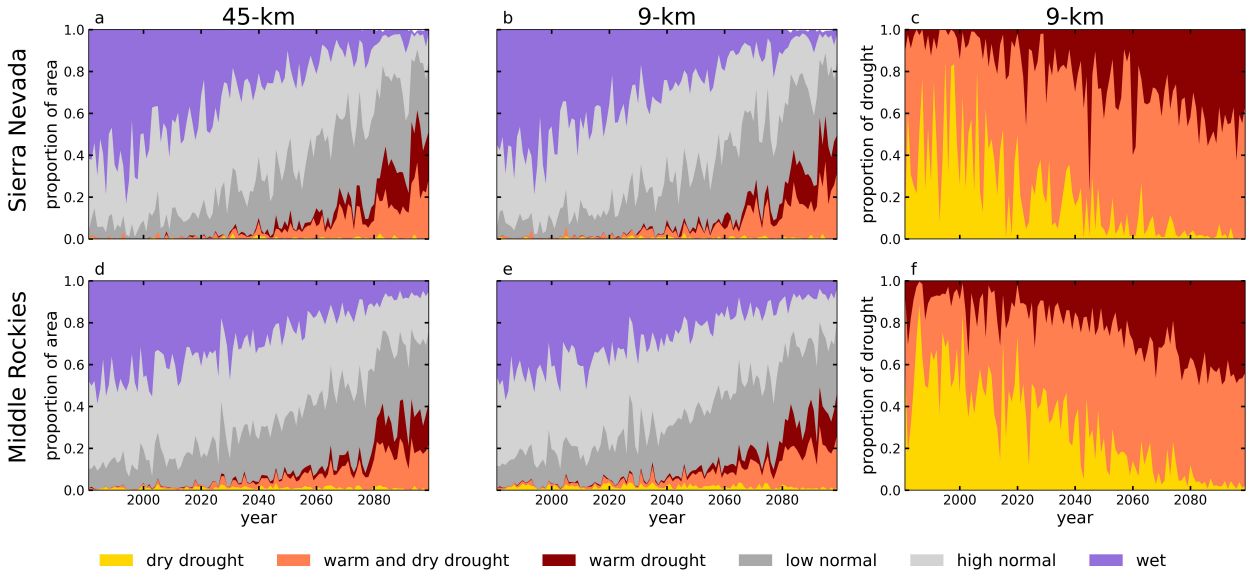

Figure 3.2: Annual percentage of land in snow conditions defined by SWEI: wet (purple, SWEI > 0.8), high normal (light gray, $0 <$ SWEI ≤ 0.8), low normal (dark gray, $-0.8 <$ SWEI ≤ 0), snow drought by category(warm: red, warm and dry: orange, or dry: yellow; SWEI ≤ -0.8). Panels a-c show results for the Sierra Nevada and d-f show the Middle Rockies. Panels c and f show the proportion of the total snow drought in a given year contributed by each snow drought type.

of the century (Figure 3.2c, f). By then, approximately 60% of snow droughts are warm and dry, with the remaining 40% corresponding to temperature anomaly alone. In other words, temperature dominates the snow drought signal but aridity still plays a meaningful role. The 45- and 9-km products show similar proportions of the total area in each category of SWEI throughout the time domain (Figure 3.2a,b,d,e), indicating that droughts statistics are moderately insensitive to coarsening resolution at these scales.

Figure 3.3a shows baseline snow drought frequency as fractional chance of a drought occurring in a given year from 1980-2010 (the baseline period). Panels b and c show the ensemble average change in snow drought frequency for 2030-60 and 2070-2100, respectively. Panels d-f show the standard deviation of the frequency in each time period, computed across the 30-year time period and across all ESMs. Overall snow drought frequency increases by the end of the century in all regions of the WUS. Frequency in all cases includes snow droughts from all causes – warm, dry, and both. The uncertainty, as estimated by the standard deviation amongst ESMs, however, increases at mid-century compared to baseline, then decreases by the end of the century. This variance includes structural and internal variability but not scenario uncertainty. The contracting range of drought frequency at end-of-century is likely due to the insensitivity of the frequency metric to increasingly severe snow

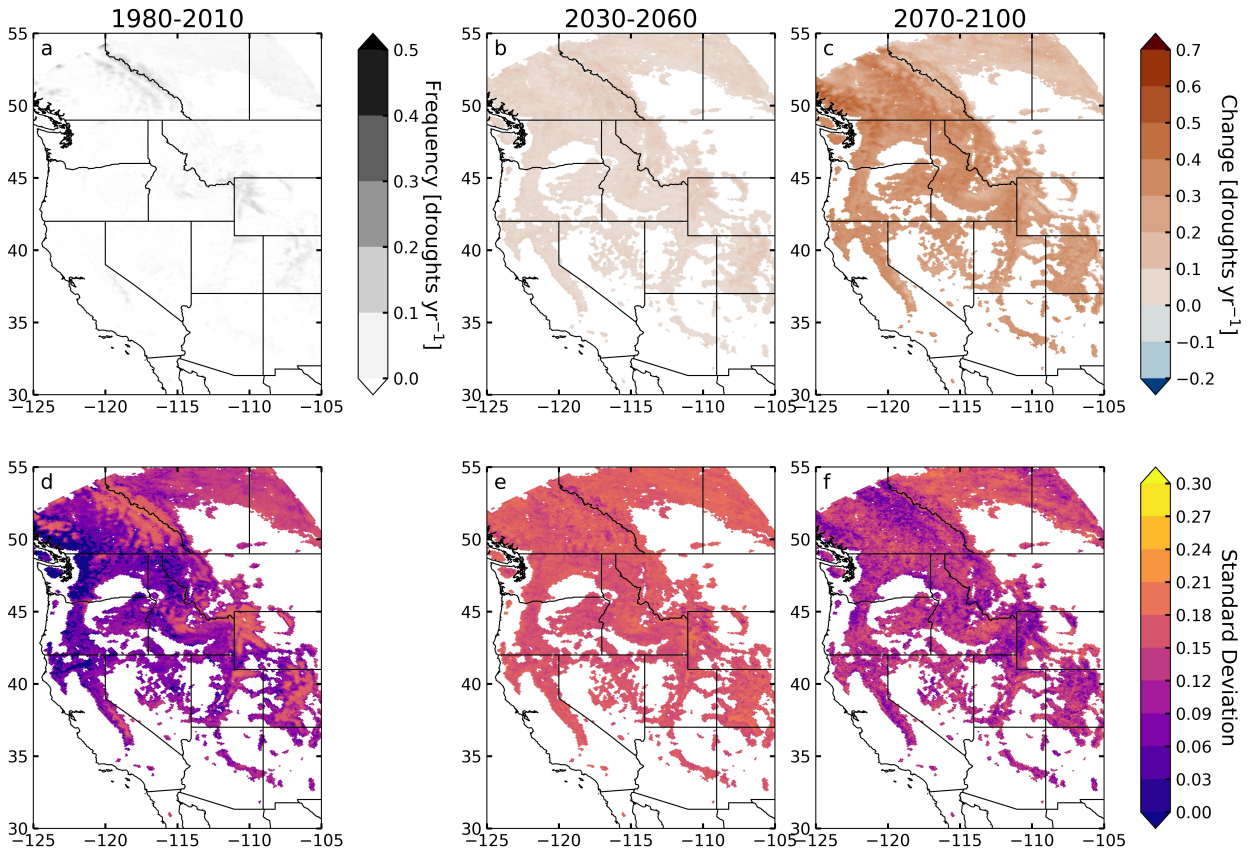

Figure 3.3: Baseline snow drought frequency (a) and change in mid-century (b) and end-of-century (c) 9-ESM mean at 9-km grid cell size. Panels d-f show standard deviation of drought frequency across the Western US for the same time periods as in a-c.

drought. As regions begin to experience more snow drought in the middle of the century, frequency can vary due to structural and internal variability. However, once a location is in a state of essentially permanent snow drought, internal variability does not affect frequency.

The frequency of snow droughts (defined by SWEI $\leq$ -0.8, Section 3.3.2) alone does not convey the snow water supply deficit. The severity, defined as the average SWEI value for snow drought events indicates the degree of deficit for the baseline period (Figure 3.4a) and the change in severity in future models (Figure 3.4b, c). The associated multi-model uncertainty, following the structure of Figure 3.3, is shown in panels d-f. A negative change indicates a more severe snow drought (i.e., pink pixels in panels b and c). While most regions experience more severe snow droughts at mid- and end-of-century, some regions show consistent decrease in severity. The standard deviation of the severity of snow droughts, shown in Figures 3.4d-f, increases with time. This increase shows the combined effects of structural and internal variability, in contrast to the decreased uncertainty in end-of-century

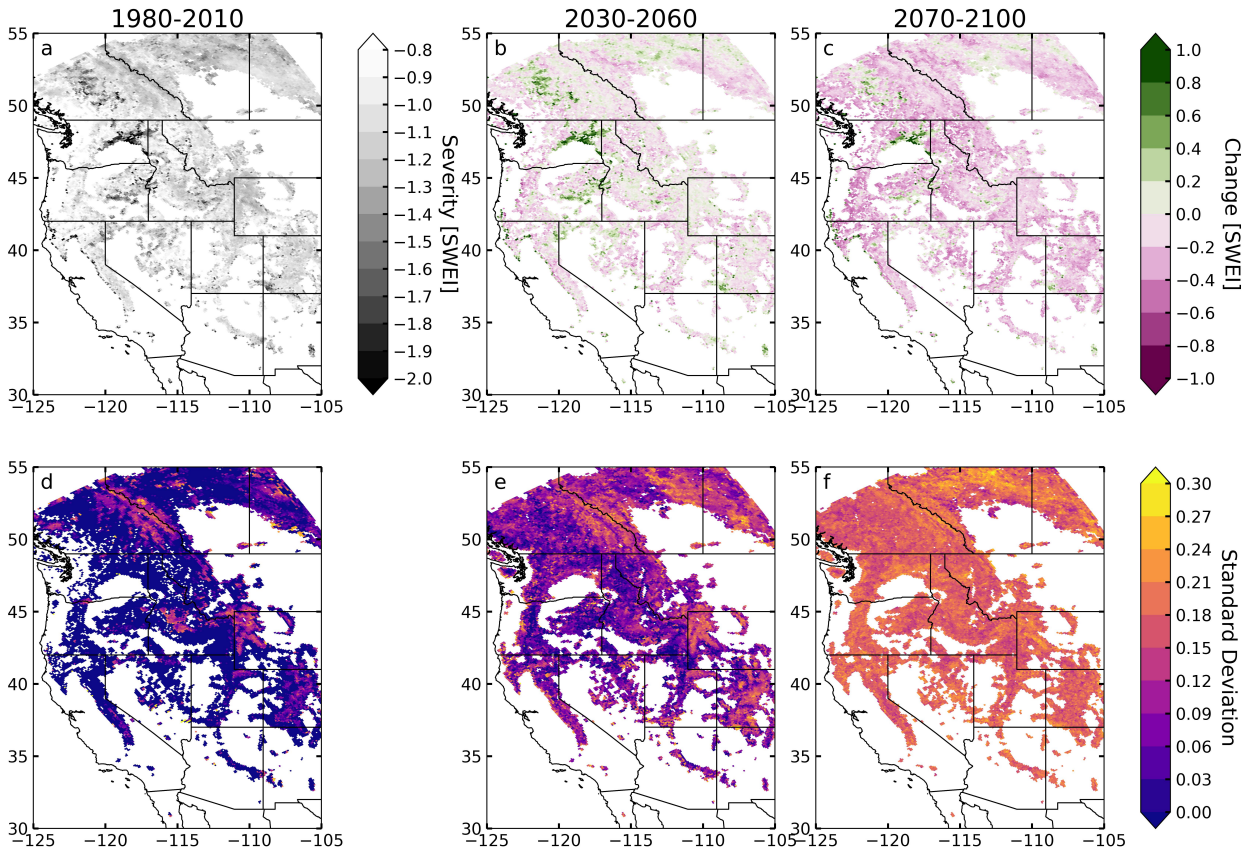

Figure 3.4: Baseline snow drought severity measured by SWEI value (a) and change in mid-century (b) and end-of-century (c) 9-ESM mean at 9-km grid cell size. Panels d-f show standard deviation in terms of drought frequency across ESMs and years for the same time periods as in a-c.

frequency.

The overall distribution of SWEI, by construction of the baseline period, shifts away from a distribution centered on zero toward more negative values by end-of-century in both study regions (Figure 3.5. This distribution shift is more extreme in the Sierra Nevada than in the Middle Rockies, but both regions see meaningful transition toward lower SWEI. The Sierra Nevada distribution (Figure 3.5a) has a higher spread within the snow drought range at end-of-century (pink lines) than the Middle Rockies (3.5b). Under such a distribution shift, if the definition of snow drought shifts with the distribution, then lower absolute values of peak SWE are allowable before triggering a drought designation.

Figure 3.6 shows, for the same time and spatial domains as in Figure 3.2, the change in annual winter-only (October-April) volume of snowfall (a,d) and rainfall (b,e), using 45-km (dashed lines) and 9-km (solid lines) grid length simulations. Sierra Nevada snowfall (a)

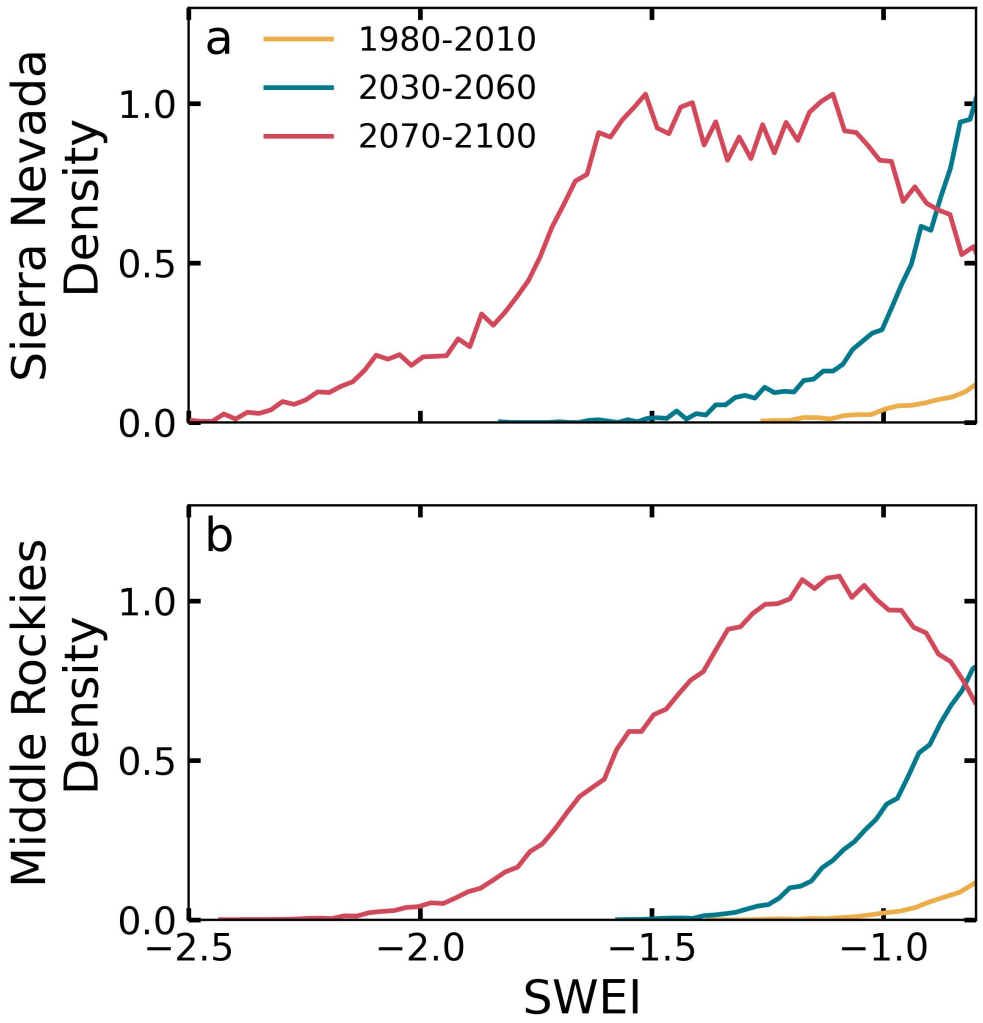

Figure 3.5: SWEI distribution for the Sierra Nevada (a) and Middle Rockies (b) only in the snow drought range (SWEI $\leq$-0.8), for 1980-2010 (yellow), 2030-2060 (blue), and 2070-2100 (pink).

decreases by 132 ± 14 mm in the 9-km outputs but only 82 ± 8 in the 45-km ouputs by 2100. Middle Rockies snowfall (d) decreases by 74 ± 20 mm in the 9-km outputs and 73 ± 12 mm in the 45-km outputs. The orientation and size of the Sierra Nevada range relative to the grid makes it so that the 45-km downscaling product is insufficient to resolve the topography of the ridge, as seen in a comparison of Figures 3.7a and c. In the Middle Rockies, the region of high elevation is larger and broader in shape, i.e., the topographic variability within a grid cell is less sensitive to resolution. Therefore, while higher-resolution ouputs enhance the details of location-specific trends, region-level statistics in the Middle Rockies are not significantly impacted by moving from 45-km to 9-km grid cells. Model resolution impacts Sierra Nevada projections more than Middle Rockies projections for snowfall. The rainfall signal has a much higher inter-model uncertainty, especially in the 9-km outputs. Sierra Nevada rainfall (b) increases by 130 ± 89 mm in the 9-km outputs and only 92 ± 50 mm in the 45-km ouptuts by 2100. Middle Rockies rainfall (e) increases by 81 ± 43mm in the 9-km outputs and 73 ± 40 mm in the 45-km outputs.

Figures 3.6c and f show the change in the proportion of precipitation that falls as snow as a function of the total precipitation change using 9-km data. The change in total precipitation is calculated as the regional-mean change from the 1980-2010 baseline period and is plotted against the snowfall-to-rainfall ratio for each region at 9-km. This relationship is ambiguous and that ambiguity is dominated by precipitation change uncertainty.

The snowfall to rainfall ratio is directly controlled by the temperature trend in WRF. From 1980 to mid-century, precipitation trends are positive while the snowfall to rainfall ratio decreases (Figure 3.6c,f); in some models, the increase in total precipitation partially compensates for the smaller fraction of precipitation that falls as snow. By 2100, the snowfall:rainfall ratio is 0.14±.02 (0.30±0.01) in Sierra Nevada (Middle Rockies). The corresponding decade's drought frequency is 41% (35%) higher than 1980-2010 for all types of droughts in the Sierra Nevada (Middle Rockies) region, as shown in Figure 3.2. Over that same time period, the percentage of droughts that occurred during a dry but not warm year dropped from 40% (54%) to 1% (2%) in the Sierra Nevada (Middle Rockies).

3.4.2 Topographic snow drought trends

SWEI, by construction, reflects a different absolute amount of snow in each location for which it is defined. Spatial patterns, then, should reflect climate-driven change and not baseline expectations of snow distribution due to elevation or local topography. Figures 3.7 and 3.8 show the multi-ESM mean peak SWE change at end-of-century (2070-2100) per degree of global warming, ΔSWE ΔT^{-1}, for the Sierra Nevada and Middle Rockies domains respectively. The global temperature signal, ΔT, from the forcing ESM is a proxy for the level of climate change experienced in a given time frame and is used to normalize other observed changes.

Figure 3.7a shows the 45-km ΔSWE ΔT^{-1} for the Sierra Nevada; Figure 3.7b shows the same but stratified by elevation band. Panels c and d show the same but at 9-km grid length, highlighting the additional information on future snow changes gained from

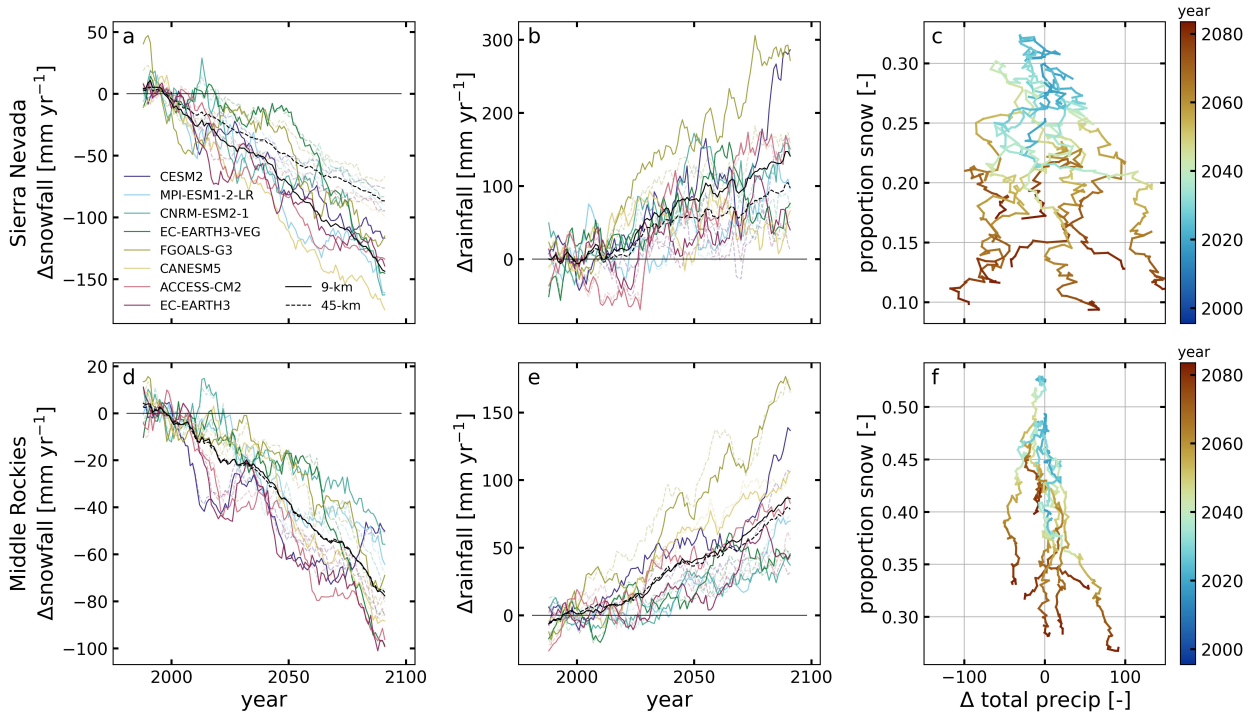

Figure 3.6: Snowfall (left) and rainfall (center) partitioned from total precipitation time series by temperature for the Sierra Nevada (top) and Middle Rockies (bottom) domains. Model results are shown at the 45- (dashed) and 9-km (solid) grid length model outputs as a 10-year rolling mean; colors indicate ESM and multi-ESM means are shown in black. Historical (1980-2010) mean value horizontal lines are indicated for each resolution. The snowfall-to-rainfall ratio is plotted against change in total precipitation compared to 1980-2010 (right) for each domain, with colors indicating the year.

increasing spatial resolution in a geographically narrow mountain range. The Sierra Nevada is much more varied across its crest than along it; due to the alignment of the WRF grid cells, this means that most high elevation areas are not represented in the 45-km outputs, therefore missing regions of ΔSWE ΔT^{-1} 1 above 2500 m a.s.l. The same comparison in the Middle Rockies (Figure 3.8) shows a smaller difference between resolutions. Higher detail and some areas of positive ΔSWE ΔT^{-1} are represented at 45-km because those regions are naturally broader.

Considering just the 9-km results for both regions (panels c and d), mid-elevations (2000-2500 m a.s.l.) represent nearly all of the snow loss, both in absolute volume and when normalized by area (Figures 3.7,3.8d). This is likely because those elevations contain more snow than lower elevations but are more likely to experience to temperatures above 0°C. Middle-to-high elevations are also the most sensitive to local snow-albedo feedback (Hernández-Henríquez

et al., 2015). Some of the highest regions of both sides, i.e., above 2500 m a.s.l., peak snow increases by several tens of mm of SWE in the last three decades of the 21st century in the 9-km models (Figures 3.7 and 3.8c,d). The 45-km model, in contrast, does not show any areas of increase, and therefore overestimates snow loss in some areas with significant snowfall (Figures 3.7 and 3.8a,b).

Coarser products may perform well over large, regional gradients, such as comparing lowlands to high plateaus. However, multi-resolution modeling of the same region with the same model does not always show agreement in overall snow volumes or even trends on aggregate or on sub-grid resolution scales. For example, in Figures 3.7 and 3.8, each Hydrologic Unit Code (HUC) 6 basin overlaps with one to three 45-km grid cells but up to 30 9-km grid cells.

3.4.3 Temperature controls on snow accumulation

We model the trend and interannual variability in annual total snowfall as a function of IVT, PDD, or both (Eqs. 3.2, 3.3, and 3.4, respectively) to quantify the relative importance of each driver on snowfall rates and therefore snow droughts. Figure 3.9 shows the pixel-wise R^2 correlation from modeling normalized snowfall trend as a function of IVT (a), PDD (b), or both (c). IVT has the highest explanatory power on leeward slopes and in the Rocky Mountains while PDD is more correlated with snowfall along the windward slope of the Cascades and Sierra Nevada. PDD is particularly powerful in the windward slope within the Pacific Northwest. The multiple linear regression of both IVT and PDD (Figure 3.9c) has less spatial variability than either single linear regression model. The regions over which IVT and PDD are strong individual predictors of snowfall are relatively complementary. In particular, leeward slopes of coastal ranges and interior mountain ranges are generally cold enough to support snowfall but are sensitive to moisture availability. In contrast, windward slopes are more moisture-saturated and therefore sensitive to temperature variations than rain-snow transitions. The multiple linear regression accounts for both processes is a better predictor of snowfall than either individual model.

However, the strength of these model predictions changes in time (Figure 3.9d). Multi-ESM spatial averages of each model performance show that the IVT and PDD multiple linear regression (green line) improves in predictive skill near the end of the century. This improvement generally tracks with the improvement in performance of the PDD-only model (yellow line). At the same time, the predictive power of the IVT-alone model (blue line) decreases. This reflects the expanding region over which the rain-snow transition controls snowfall amount.

The same set of linear models applied to the detrended signal represents the sensitivity of the snowfall signal to interannual variations, independent of the larger climate signal. Figure 3.10 shows the performance of each set of linear models, as in Figure 3.9. The interannual variability models show similar spatial trends as the trend models, albeit with slightly lower overall correlation. The transition to stronger PDD correlation at end of century occurs slightly later and is less strong, as indicated by the location of the intersection and the

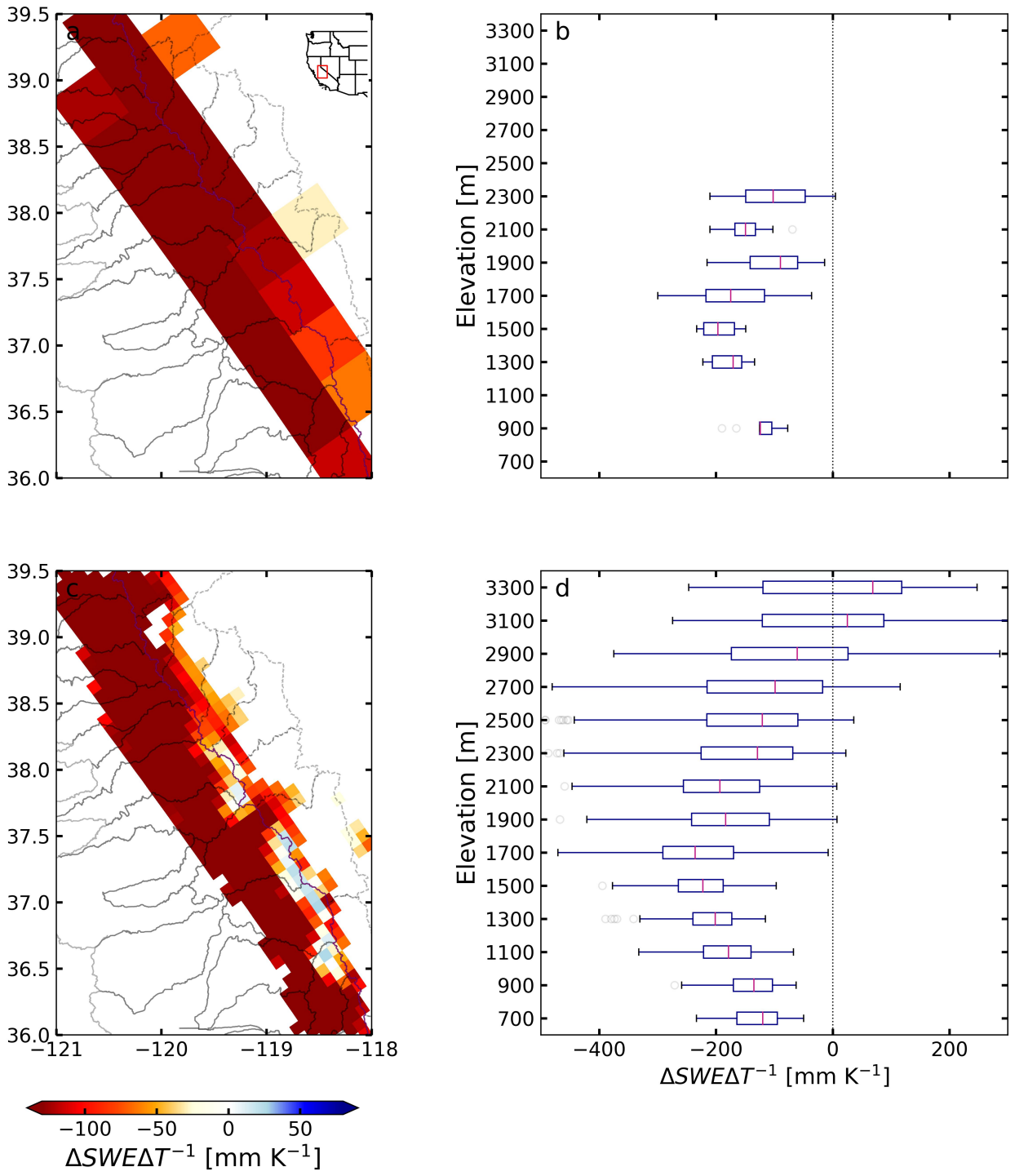

Figure 3.7: Map of ΔSWE ΔT^{-1} for the Sierra Nevada region at 45- (top), 9-km (bottom) grid length. HUC6 basins outlines are shown in gray with windward basins indicated by solid lines and leeward basins with dashed lines. Panels b and d show the distribution of ΔSWE ΔT^{-1} across elevation bands for the 45- and 9-km grid length, respectively. Box-and-whisker plot boxes indicate first and third quartiles; red vertical lines indicate medians; dots indicate outliers.

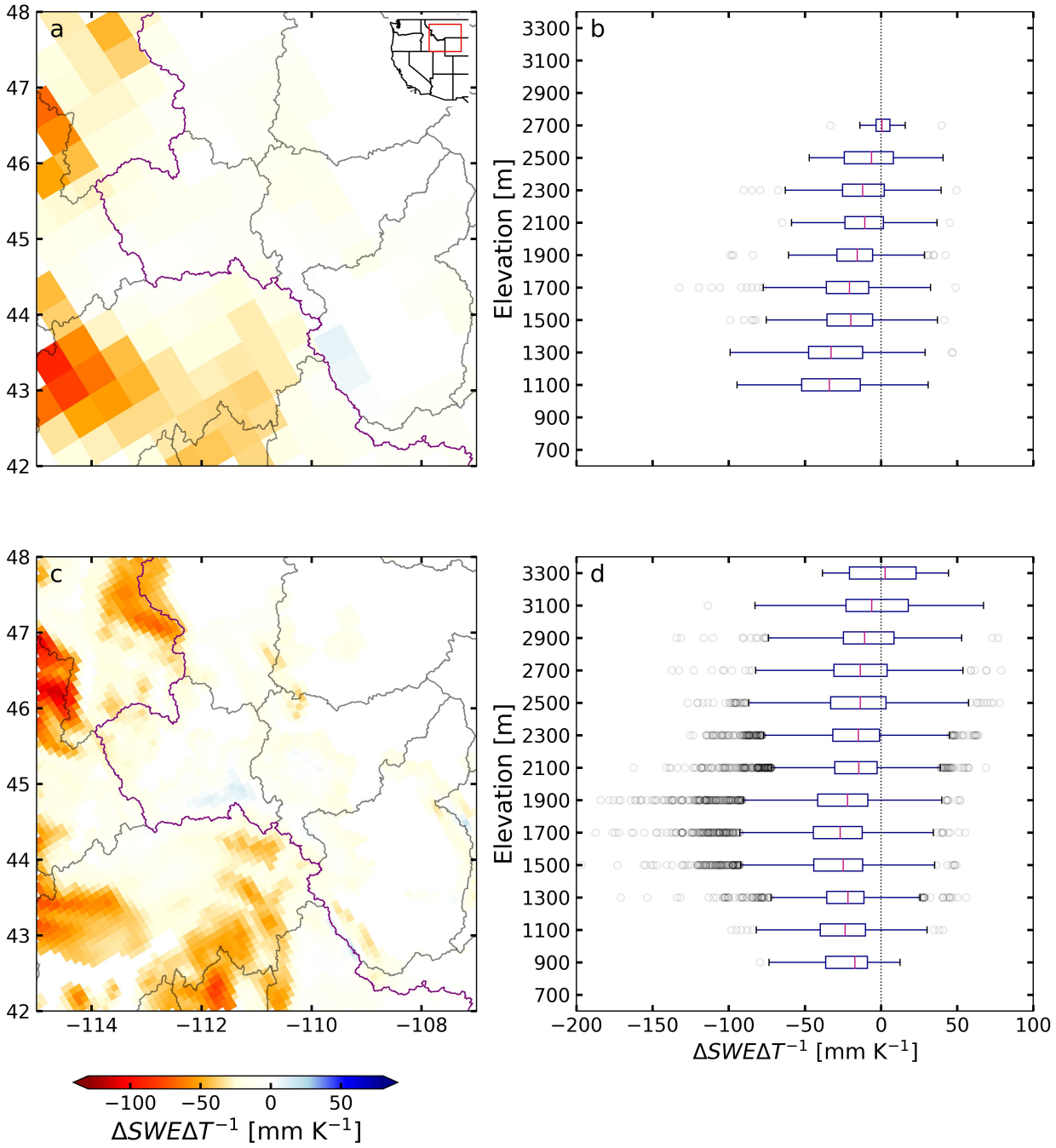

Figure 3.8: Same as Figure 3.7 but for the Middle Rockies.

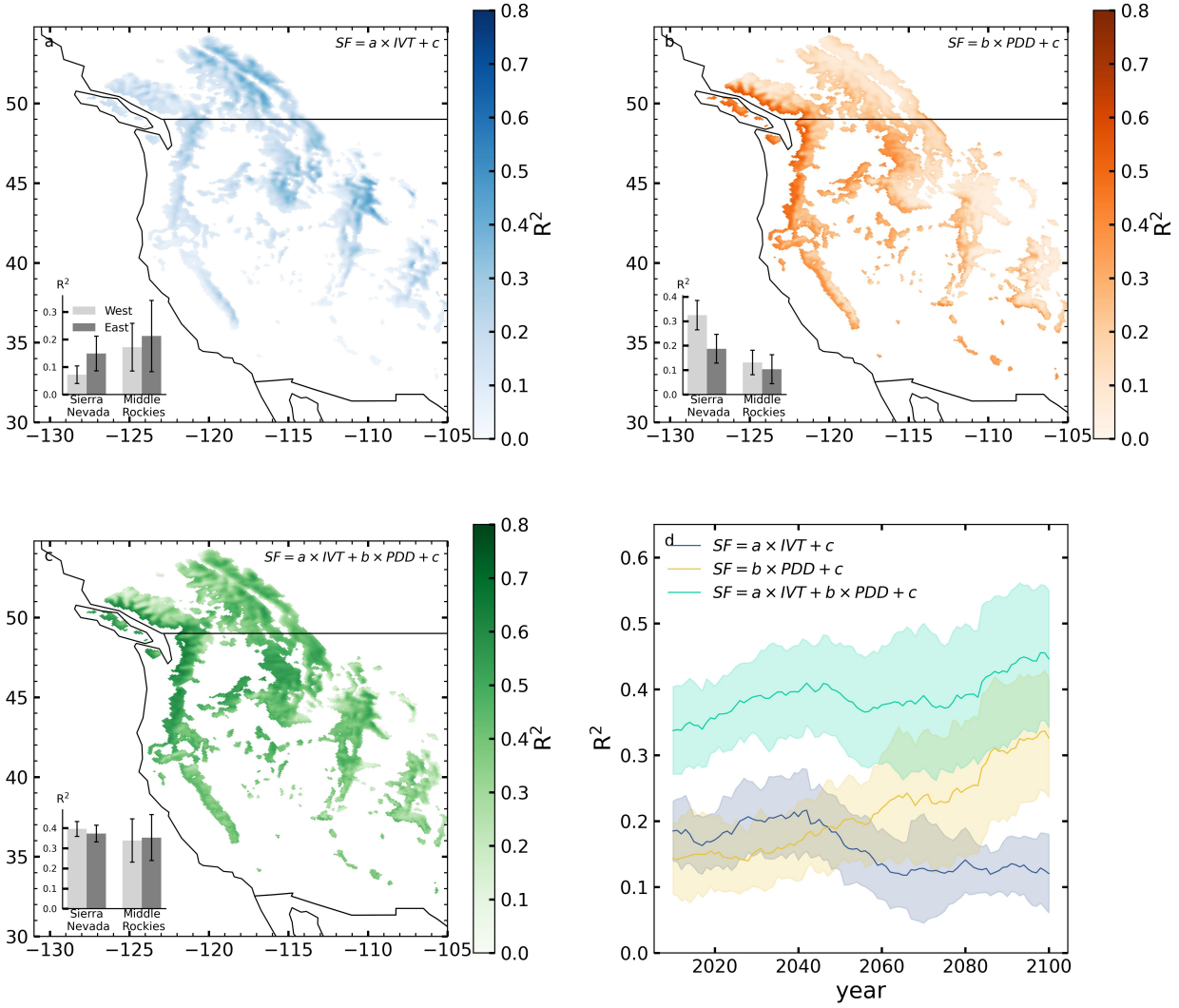

Figure 3.9: Map of correlation (R^2) for snowfall trend based on IVT (a), PDD (b), or both IVT and PDD (c). Values shown are averaged between driving ESMs and over the time period modeled. Each inset bar plot shows the average R^2 value for the western (light gray) and easter (dark gray) boundaries of the Sierra Nevada (left) and Middle Rockies (right). Uncertainty bounds are standard deviation. The change in time of the spatial mean (d) shows the IVT, PDD, and IVT-PDD models in blue, yellow, and green lines, respectively. Shading indicates one standard deviation.

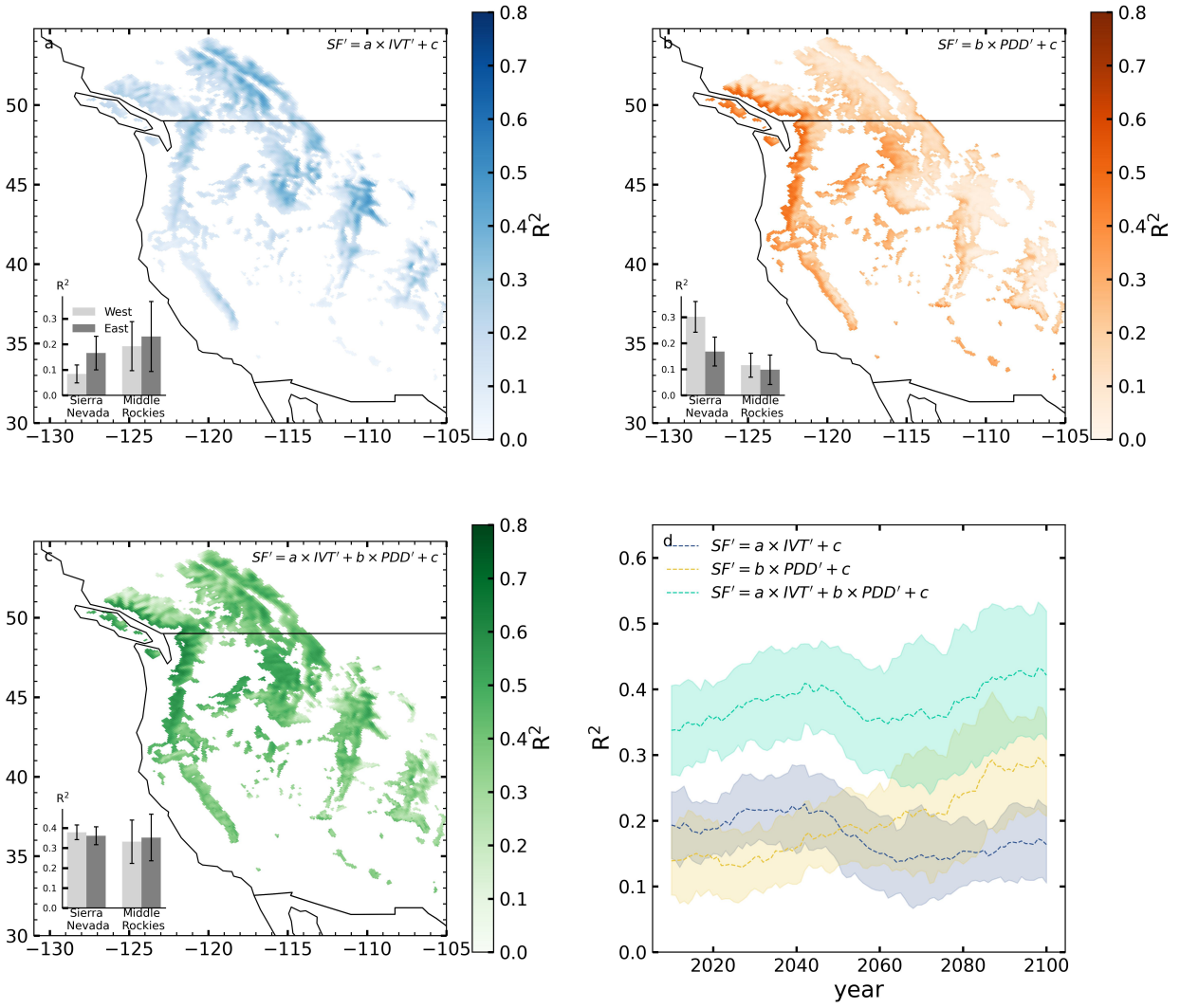

Figure 3.10: Same as Figure 3.9 but for the detrended snowfall, IVT, and PDD models.

spread between the IVT (blue) and PDD (yellow) lines in Figures 3.9d and 3.10d. While the specific time of emergence of the transition to temperature-driven annual snowfall is not possible to determine in a small ensemble, the 9-ESM downscaling experiment used here suggests 2040-2060 as a transition period for both the trend (Figure 3.9d) and interannual variability (Figure 3.10d). These mechanisms further underlie the main causes of snow drought: warm temperatures (PDD-sensitive) and low overall precipitation (IVT-sensitive).

In the Sierra Nevada's eastern slope, typically within an orographic rain shadow, IVT is more important throughout the time domain (Figure 3.9 bar plot insets), but this reliance increases with time even as the IVT signal weakens on average throughout the WUS Figure

3.9d). The drier leeward slopes respond to the increased fractional precipitation on the lee side of mountains (Siler & Roe, 2014), especially at higher (colder) elevations. On the western slope, temperature is a larger driver of interannual snowfall variability through the end of the century.

3.5 Discussion

The modeled increase in snow drought frequency alone is an expected quantification of warmer future climates, but does not necessarily imply a prediction of a drought declaration, as drought declarations typically use a moving baseline approach. In this work, trends in SWEI are used to reflect shifting distributions of water supply and storage in snowpack, which are caused by low precipitation and/or high temperatures. The emergence of warm snow droughts as a more frequent category (Figure 3.2, 3.3) represents years in which low water storage, not low water supply, may be a freshwater management challenge in the Western US. The use of temperature and precipitation to define snow drought categories may not always correspond to upper atmosphere regional temperature or IVT, as regional circulation and local microclimate produces additional variation. Therefore, we expect analyses of preceding atmospheric quantities (e.g., Figures 3.9, 3.10) to be more climate sensitive, but slightly less predictive of snow drought.

Because increasing global temperatures should increase moisture availability while increasing the proportion of liquid precipitation, a potentially contradictory climate response of snow is possible. In In Figures 3.7 and 3.8, the snow response to global temperature change is used to quantify the outputs of this balance. At higher elevations, where starting temperatures are colder, many areas see net gains in snowpack, although the interquartile range of this response spans both the positive and negative at the highest elevation bands in both regions studied. The ability of 9-km grid cell model outputs to capture the true behavior of high-elevation, complex terrain is still limited; the true response at some horizontally narrow high-elevation regions may be diminished by grid cells that also contain lower-elevation regions. Some of this range is also explainable by the additional component of orography in determining whether a location is more sensitive to the precipitation quantity or phase components of the snowfall climate response.

The relative insensitivity to IVT variations on the western slope can be explained by considering that increases in atmospheric water vapor would weakly impact precipitation intensity and the extra water would instead persist longer in the system, moving to the other side of ridge to deposit there instead of increasing local snowfall on the windward slope. However, it is important to note that these models track both increases and decreases in snowfall; the values shown here are agnostic to the sign of snowfall change.

The climate projection component of this work comes from eight CMIP6 ESM simulations of the SSP3-7.0 scenario. While climate predictions indicate decreases in snowfall fraction across all ESMs, the end-of-century total precipitation within each region increases on average but decreases in at least three ensemble members. The spread in total precipita-

tion across the ESMs can be interpreted as the structural uncertainty in precipitation change projections. Further, most of the multi-model spread in total precipitation change comes from rainfall. The contrast between consistent increases in snow drought and inconsistent changes in precipitation across models suggests that the increase in snow droughts in the SSP3-7.0 scenario is largely driven by temperature, rather than by precipitation. Precipitation trends do contribute to changes in peak snow storage, especially in the later half of the 21st century.

The snow-to-rain transition from climate change is not only a direct product of temperature increase, however, as humidity and pressure both impact hydrometeor phase (Dai, 2008; Jennings et al., 2018). In the WUS-D3 configuration, Noah MP is directly coupled to WRF (Rahimi et al., 2022) and precipitation is classified as snow or rain following the temperature thresholds of (Jordan, 1991). While a full examination of this nuance is not possible using Earth system model outputs as the snow-rain transition is prescriptive, our results lend general guidance to the types of regional snow drought patterns that could develop in future decades. Efforts were made during the modeling phase (Rahimi et al., 2024a) to address pixel-size representation of known ground measurements, especially within the SNOTEL network, but it is still not possible to evaluate subgrid variance in snow drought in the current modeling framework.

3.6 Conclusions

In this work, we evaluate predictions of future snow drought occurrence and category in a high-resolution, bias-corrected, multi-model ensemble. As in previous studies (Cowherd et al., 2023; Dierauer et al., 2019; Dierauer et al., 2021), these findings project an increase in snow drought frequency in future decades, with a greater fraction of future snow droughts co-occurring with high temperatures than with low precipitation. In other words, the snow droughts of the future are more likely to be warm than dry. This increase is clear in time series across the 9-ESM ensemble and at all resolutions modeled, for the WUS as a whole and for the two domains of focus in this work. Those trends, shown in Figure 3.2, also correspond to a change in snow drought type from mostly dry to mostly warm. As found in Cowherd et al. (2023), historical snow droughts are associated with a dry precipitation anomaly in more than 80% of cases before 2014. Between these studies, despite regional, resolution, and climate scenario differences, the transition to a snow drought profile with fewer dry snow droughts is clear and consistent. By 2100, more than 90% snow drought coincide with a warm temperature anomaly, with about half of those also corresponding to a dry precipitation anomaly. We only consider one time point per water year, the peak SWE, in order to capture a pre-spring streamflow metric of the available water resources as well as a proxy for storage. Additional work, such as exploring time-integrated volume storage within a water year as a quantity of interest for snow drought definitions (Aragon & Hill, 2024), would further capture both the water volume and storage services of snow.

Next, the multi-resolution downscaling permitted comparison between spatial scales of

snow trends. In both regions studied here – Sierra Nevada and Middle Rockies – the 9-km results show less negative change in SWE per degree of global warming at high elevations in the Western United States (Figures 3.7, 3.8). In the Sierra Nevada, the highest elevations see a positive change in peak SWE with warming; in the Middle Rockies, some high elevation areas see an increase. High elevation offset of mid- and low-elevation snow loss, or the trade-off between warming-driven precipitation increases and phase change, is a short-to-moderate-term effect; the timing of transition in a given region depends on latitude and hypsometry.

Lastly, we explore the reasons for this pattern from a statistical perspective. The impacts of temperature change on snowfall fraction (Figure 3.6c,f) are uncertain in current Earth system models, largely due to uncertainty in total precipitation. The linear regression models do not directly represent dynamical mechanisms for change, such as altered storm tracks or frequency of atmospheric rivers. However, the WUS-D3 does include global circulation change via the parent ESMs, so the data used for the regression is impacted by dynamical change. Further, uncertainty in the sign of regional total precipitation change is an ongoing challenge in Earth system modeling (e.g., Meehl et al., 2007). Statistical covariance of short-term snowfall anomalies with surface temperature anomaly and vapor transport trends (Figure 3.9) and anomalies (Figure 3.10) shows geographic variance in the importance of those mechanisms in explaining future snow patterns. This analysis focuses specifically on interannual deviation from the local mean trend, not on changing mean snowfall. However, this analysis is limited by reliance on model physics to both cause and explain the outcomes.

Hydroclimate simulations at many scales – from gauging station to global – highlight the water supply and timing challenges we may face in the future. Snow's role as source and storage in the hydrologic system means that snow drought is an important driver of other types of droughts (Barnhart et al., 2016; Van Loon & Van Lanen, 2012) and of drought predictability. In parallel to the drought risk studied here, drought predictability is threatened under warmer climates (Cowherd et al., 2024; Livneh & Badger, 2020). Further work on extreme hydroclimate events – both high and low snowfall – will further clarify the connections between the mechanisms for climate-driven mean and extreme change.

3.7 Open Research

The WUS-D3 used for this project are publicly available at Rahimi et al. (2024a). US EPA Level III ecoregions were retrieved from https://www.epa.gov/eco-research/level-iii-and-iv-ecoregions-continental-united-states. The code for this project is available at https://github.com/mariannecowherd/wus-snow-drought/.

Chapter 4

Climate change-resilient snowpack estimation in the Western United States[1]

"The real world is neither linear nor stationary; thus the inadequacy of the linear and stationary data analysis methods that strictly adhere to mathematical rigor is becoming glaringly obvious." - Norden E. Huang

4.1 Abstract

In the 21st century, warmer temperatures and changing atmospheric circulation will likely produce unprecedented changes in Western United States snowfall (Lute et al., 2015; Marshall et al., 2019; Siirila-Woodburn et al., 2021), with impacts on the timing, amount, and spatial patterns of snowpack (Barnett et al., 2005; Huning & AghaKouchak, 2018; Huss et al., 2017; López-Moreno et al., 2017). The ∼900 snow pillow stations are indispensable to water resource management by measuring snow-water equivalent (SWE, Pagano et al., 2009; Serreze et al., 1999) in strategic but fixed locations (Changnon & Kunkel, 2006; Oyler et al., 2015). However, this network may not be impacted by climate change in the same way as the surrounding area (Livneh & Badger, 2020) and thus fail to accurately represent unmeasured locations; climate change thereby threatens our ability to measure the effects of climate change on snow. In this work, we show that maintaining the current peak SWE estimation skill is nonetheless possible. We find that explicitly including spatial correlations—either from gridded observations or learned by the model—improves skill at predicting distributed snowpack from sparse observations by 184%. Existing artificial intelligence methods can

[1]This chapter is adapted from Cowherd, M., Mital, U., Rahimi, S., Girotto, M., Schwartz, A., & Feldman, D. (2024) Evolution of global snow drought characteristics from 1850 to 2100. *Communications Earth & Environment* , **5**, 337 and is reproduced here with permission of the authors.

be useful tools to harness the many available sources of snowpack information to estimate snowpack in a nonstationary climate.

4.2 Introduction

In North America, mountains comprise ¡25% of the land area yet account for 60% of the continent's snowpack (Wrzesien et al., 2018). Scientists and water managers estimate regional snow water equivalent (SWE) throughout the winter and especially at the end of winter to predict intra-annual water resources, including streamflow and groundwater recharge (Li et al., 2019a). There are no direct satellite observations of SWE, and indirect observations are either sparse in space and time (Margulis et al., 2016a) or used minimally in numerical simulations and reanalyses (Fang et al., 2022; Pagano et al., 2009). In the Western United States (WUS), the estimation of this quantity in practice relies heavily, or even exclusively, on in situ data from the more than 900 (804 excluding Alaska) automated snow pillows from the snow telemetry (SNOTEL) network and >100 additional state-based snow course networks (Serreze et al., 1999). These site-based measurements are both rich in information content regarding snow depth and density and have historically been informative as empirical predictors of catchment-wide SWE (Pagano et al., 2004), especially the end-of-winter peak of SWE that sets the initial conditions of spring snowmelt (Bohr & Aguado, 2001).

In situ, calibrated, and validated measurements of climate-sensitive observables are generally more informative about Earth system changes with longer data records (Council, 2004; Overpeck et al., 2011; Schneider et al., 2013). However, this implies stationarity in the spatial and temporal distributions over which those measurements sample (Milly et al., 2008). SNOTEL stations, most of which were installed in the 1980s, were intended to monitor the seasonal patterns of snow quantities and their interannual variability within a 20th-Century mountainous hydroclimate, not to monitor the change in that same hydroclimate. Moving the network is logistically impractical (Changnon & Kunkel, 2006), so the anthropogenic warming-induced snow change in the 21st century will fundamentally reduce the sensitivity of the SNOTEL network's ability to predict drought at a management-relevant scale (Livneh & Badger, 2020). Punctuated sensitivity degradation is likely to occur during periods of maximized aridity characterized by dry and warm spells; it is exactly these times when water security across the region will be most strained (Cook et al., 2018; Cowherd et al., 2023).

In this work, we estimate the magnitude of WUS SNOTEL and California Cooperative Snow Survey (CCSS) snow pillow network sensitivity degradation in a climate-changed world and explore new approaches to interpreting the information available in observational networks. We do so by analyzing high-resolution WUS climate projections to determine when and where novel snow patterns may emerge in the 21st century and then how in situ and remote sensing systems are sensitive to such patterns. We use the Western United States Dynamically Downscaled Dataset (WUS-D3) (Rahimi et al., 2024a), a nine-member ensemble of global climate models (GCMs) from the 6th phase of the Coupled Model Intercomparison

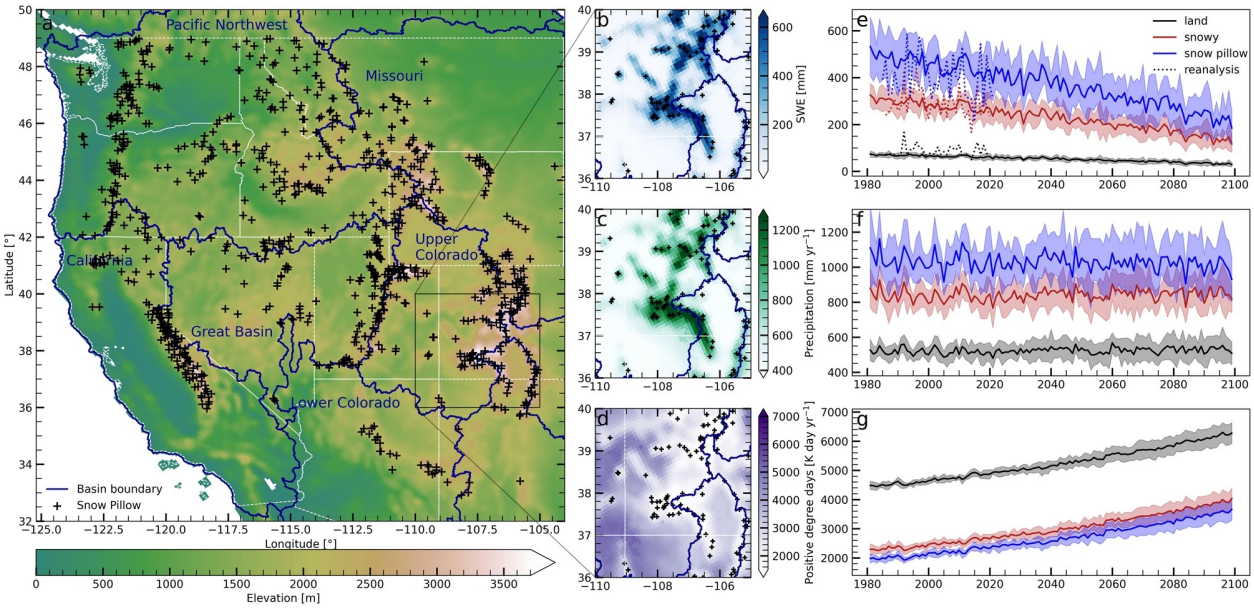

Figure 4.1: a) The locations of WUS snow pillow stations (black crosses) and HUC2 watersheds (dark blue lines). b) Upper Colorado River Basin 1981–2014 average peak SWE. c) Same as b) but for winter season cumulative precipitation. d) Same as b) but for winter season positive degree days. e) Annual- and GCM-average time series of peak SWE (solid lines) for the entire WUS domain as defined in a) (black), snowy regions (red, >100 mm average peak SWE from 1980 to 2000 to conservatively include ephemeral and seasonal snowpacks) and at the locations of SNOTEL sites (blue) with the WUS-SR product (dotted lines)17. The standard deviation of the 9 GCMs is shaded for each respective area. f) Same as e) but for winter cumulative precipitation. g) Same as e) but for annual positive degree days.

Project (CMIP6) (Eyring et al., 2016), which is dynamically downscaled with the Weather Research and Forecasting (WRF) model (Powers et al., 2017). This projection ensemble allows for high-resolution evaluation of snowpack outputs that evolve in time according to model physics. Figure 4.1 shows the WUS-D3 solution domain with locations of current WUS snow pillow sites. Insets show historical (1980–2014) and Shared Socioeconomic Pathway (SSP) 3-7.0 (2015–2100) ensemble-mean annual maximum SWE, annual cumulative precipitation, and positive degree days for an example subregion with complex terrain in the Rocky Mountains. SSP 3-7.0 is a high but plausible emissions trajectory covering 2015–2100 (O'Neill et al., 2016). This figure shows that snowpack has already declined and the temperature has already increased in the WUS, as seen by both downscaled models and reanalysis (Clow, 2010; Initiative, 2015; Mote et al., 2018; Rahimi et al., 2022). Snowpack declines and temperature increases are expected to continue, albeit unevenly, across the WUS.

4.3 Methods

4.3.1 Downscaled regional climate models

In this work, we use WUS-D3 (Rahimi et al., 2024a), a nine-member ensemble of CMIP6 GCMs, dynamically downscaled with WRF (Powers et al., 2017). Each raw GCM was accessed at its native resolution, and its temperature, humidity, horizontal winds, and geopotential fields were bias-corrected (Bruyère et al., 2014). Table A.1 lists each GCM name and variant used in this ensemble. These bias-corrected fields were then used to drive WRF simulations on a 45-km outer domain grid. One-way nesting was then used to downscale the 45-km results to a 9-km grid length inner domain over the Western United States The SWE field is obtained from directly coupling Noah-MP to WRF following methods in Rahimi et al. (2024a) and Rahimi et al. (2022). For this work, we use 9-km data, as the domain of that product covers the entire WUS land region. While this grid cell size can obscure orographic influences on snowpack, the snow product in the historical simulations of WRF with the bias correction described above showed skill in being able to reproduce observed diagnostic fields (Rahimi et al., 2022), including exhibiting skill in largely reproducing the SWE values found in historical regional snow reanalyses (Margulis et al., 2016a), as shown in Fig. 4.1. The skill of WUS-D3 SWE is further demonstrated in the snow pillow site-specific climatology shown in Figure A.1. We justify this bias correction because the biases in the corrected fields are endemic to CMIP6 GCMs and arise from unrealistic circulation biases in the northeastern Pacific Ocean. These errors, relative to the European Centre for Medium-Range Weather Forecasting Reanalysis product—version 5 (ERA5, Hersbach et al., 2020), are carried forward in future projections and must be corrected to capture realistic WUS hydroclimate.

We create a historical downscaled dataset covering 1980–2014 by downscaling the historical experiment of the suite of CMIP6 models analyzed (Eyring et al., 2016) and we create a dataset that extends from 2015 to 2100 with CMIP6 models that are forced with the Shared Socioeconomic Pathway (SSP) 3-7.0 emissions scenario (O'Neill et al., 2016). Here, the SSP3-7.0 simulations provide one scenario through which to explore the nature of future change in snowpack-related observations.

For this work, we use the 'snow' (snow water equivalent in mm), 'prec' (total precipitation in mm d^{-1}), and 't2' (2-m air temperature in K) outputs of WUS-D3. The peak SWE value at a given pixel is simply the annual maximum at that pixel, which approximately represents the total snow water storage accumulated in a particular pixel. April 1 has been a historically useful proxy for peak SWE and has been used in water supply forecasting, but we use peak SWE here because the regional and temporal drift between true peak SWE and April 1 is increasing and will continue to increase (Montoya et al., 2014).

The precipitation field was used by summing the precipitation of any phase that occurred at that pixel for that water year prior to the peak SWE at that pixel. Similarly, positive degree-day (PDD) values at a given pixel were used as a driver. We calculated this term by summing the positive-only difference between the 2-m air temperature at that pixel and 0C

for the same time period. The calendaring convention for this analysis is based on the WUS water year that begins on October 1 and is named for the calendar year of the following year (e.g., the water year 1981 is from October 1, 1980 to September 30, 1981 inclusive).

4.3.2 Currently available snow data products

The data combinations evaluated in this work were constructed to reflect actual snow-related data products. We accessed daily SNOTEL records from the Natural Resources Conservation Service (NRCS) SNOTEL data repository (Serreze et al., 1999) and other snow pillows from CCSS. For comparisons between these data and the downscaled historical simulations, we truncated the snow pillow record to the time period that overlapped between the two datasets: 1980-2014. We accessed the WUS-SR (Fang et al., 2022) SWE data post-assimilation records from the National Snow and Ice Data Center (NSIDC) and selected pixel-wise maximum SWE for each water year in the time domain 1985–2014 for comparison with modeled products in Fig. 4.1. We also used SNOTEL and WUS-SR data to evaluate the ability of the 9-km downscaled data to represent the performance of the SNOTEL network. Other work has conducted similar comparisons with positive outcomes, including for statistically downscaled, coarser-grid products (e.g., ref. (Livneh & Badger, 2020)). Figure A.1 shows daily SWE climatologies for each of the 9-km downscaled, bias-corrected WUS-D3 simulations at pixels containing at least one SNOTEL station from 1985 to 2014, compared to the same time frame with the SNOTEL record and the same pixels in WUS-SR.

Peak SWE in many watersheds of the WUS is constrained by multiple snow pillow stations, weather analyses, and satellite data (Barrett, 2003; Fang et al., 2022; Margulis et al., 2016a). The most comprehensive observations of catchment-scale SWE currently are sub-orbital: aerial lidar measurements such as the Airborne Snow Observatories (ASO, Painter et al., 2016) , or stereo-photogrammetric reconstructions of snow height at the end of winter (Vander Jagt et al., 2015) yield spatially-resolved, cloud-contamination-free SWE products because those measurements are a powerful constraint on SWE. The uncertainty in peak SWE from these measurements is driven by uncertainty in snow density (Raleigh & Small, 2017), the difficulty of measuring snow under canopies (Kostadinov et al., 2019), and off-peak observation timing. Therefore, in situ datasets, particularly from snow pillows, form the backbone of peak SWE estimation in most regions, as reflected in the snow pillow data case; sub-orbital observations are modeled in the intensive data case.

Spatially and temporally resolved gridded precipitation fields, derived from a wide range of observational datasets including ground-based gauges and radars, satellite-based radars and radiometers, and numerical weather simulation (Pradhan et al., 2022), represent another key dataset with predictive information on peak SWE in the mountains, as reflected by the gridded data case. Surface energy budgets strongly influence SWE, and measures of temperature, such as degree-days, provide practical information on snowpack processes that would negatively influence peak SWE, including snowmelt (Rango & Martinec, 1995). There are also numerous satellite datasets that are relevant to, but only loosely constrain peak SWE in high-altitude complex terrain. For example, the areal fraction of snow is readily

measured from multi-spectral radiometry on satellite-based platforms such as the MODerate resolution Imaging Spectroradiometer (MODIS) and Visible Infrared Imaging Radiometer Suite (VIIRS), but those products do not observe snow depth and density.

4.3.3 Spatial pattern repeatability

The snow pattern repeatability (Sturm & Wagner, 2010) is defined as the average R^2 between the nondimensionalized peak SWE field S; where $S = \frac{s-\mu}{\sigma}$ and s is the SWE value in a given grid box, μ is the mean for that time, and σ is the standard deviation of that time step (Fang et al., 2023); and each of the 20 previous years of the same. The 20-year moving window gives each analysis year that we analyze a wide range of interannual variability in SWE while not being directly impacted by a nonstationary climate. The metric S has been applied to higher-resolution snow data in (Sturm & Wagner, 2010) to demonstrate a high degree of pattern repeatability between years. This method of calculating pattern repeatability treats pixels as independent points without a 2-D structure because points in a basin are flattened for correlation analysis.

4.3.4 Perfect data experiments

The findings presented here, including those in Figs. 3 and 4, are derived from perfect data experiments (sometimes referred to as observing system simulation experiments, (Errico & Prive, 2018). In this framework, a number of different data models attempt to predict the underlying peak SWE value produced by one of the WUS-D3 simulations at a given time at a given location using predictors based on the atmospheric and surface state from that same WUS-D3 simulation. These data models range in algorithmic complexity and are only given incomplete information about the peak SWE of the WUS-D3 simulation that they are trying to predict. Consequently, synthetic, but realistic errors are added to the gridded precipitation, temperature, fSCA, and SWE predictors. Additionally, a range of different variables (see the section Data groups for peak SWE prediction) and algorithms (see the section Models for peak SWE prediction) were used to predict peak SWE. Finally, the construction of the perfect data models was designed to ensure that the data models only used a subset of the predictor variables in each WUS-D3 simulation that reasonably corresponds to the data that will be available to make a prediction for peak SWE (e.g., the prediction of any data model at a given time would not be aware of future predictor or predictand values). These observing system simulations are idealized but reveal the challenges, opportunities, and relationships between predictors and a predictand associated with using different observations and data processing algorithms and are used to assess the climate resiliency of peak SWE estimation approaches.

4.3.5 Synthetic gridded data

There are several synthetic, gridded data fields that are included in these perfect data experiments, including the following. The data field for the fractional snow-covered area (fSCA) is estimated from the distributed SWE field reported in WUS-D3 in order to correspond to what an optical spectroradiometric satellite observes (e.g., Landsat or MODIS Normalized Difference Snow Index (Riggs et al., 1994; Salomonson & Appel, 2006)). By imaging the same location approximately daily, the satellite instrument datasets skillfully measure snow fraction in and around peak SWE in spite of cloud contamination. For a given day, if a pixel has SWE>40 mm, then it is assigned an fSCA value of 1, otherwise 0 (Micheletty et al., 2022). To account for cloud contamination, the fSCA values are corrupted by randomly masking out 1/3 of the days between the start of the water year (October 1) and the date of peak SWE. For days that are considered cloudy, the value of fSCA is determined by considering the most recent non-cloudy day. The daily fSCA values are then averaged for the entire snow season to yield a synthetic data field of fSCA corresponding to peak SWE.

The PDD and cumulative precipitation fields are constructed from modeled values of those same quantities, with error and bias added as calculated between the WUS-D3 historical outputs and products from Parameter-elevation Regressions on Independent Slopes Model (PRISM) (Daly et al., 2008) followed by a spatial gradient smoothing step (see Figure A.2).

Lastly, the distributed April 1 SWE in the intensive data modeling case was constructed to simulate a potential SWE observation either by a future SWE satellite or a modeled product from a sub-orbital aerial system (e.g., ASO). Due to operational constraints that limit the windows when aerial data are collected, the exact timing of sub-orbital observations relative to the peak SWE timing is not guaranteed and cannot be retroactively adjusted to align with the true date of peak SWE. To account for this variance, we randomly assigned a date of synthetic sub-orbital observation by sampling from a normal distribution centered on April 1 of the water year and a standard deviation of seven days.

The synthetic future gridded temperature and precipitation datasets were developed using a statistical mapping process between the WUS-D3 outputs and historical PRISM data for the same HUC6 basin. For the 1980–2020 time period, we aggregated PRISM data for precipitation and temperature over the WUS domain and re-gridded the 4-km product to the 9-km WUS-D3 grid. For the cumulative precipitation and PDD fields, we then created a pixel-wise bias and error comparison between the PRISM data and the simulated data. We then produce synthetic gridded fields for the analysis presented in Figs. 3 and 4 by adding the same bias and error statistics we diagnosed in the historical WUS-D3 simulations to the 2015-2100 WUS-D3 simulation. The synthetic error is produced by randomly sampling from a distribution that exhibits the same bias and error statistics as the WUS-D3 historical output relative to PRISM. Because each pixel's future error was randomly sampled independently from all other pixels, we then applied a spatial smoothing algorithm (Chambolle, 2004), as implemented in Python's skimage module (Van der Walt et al., 2014). This smoothing algorithm captures the spatial correlation structure of WUS-D3 errors relative to PRISM.

Figures A.2a and c show the synthetic PRISM data for temperature and PDD, respectively, before the spatial smoothing. Figures A.2b and d show the same quantities after spatial smoothing. The smoothing algorithm does not change the overall distribution of the absolute quantities across the region, but rather creates a more realistic synthetic PRISM dataset with spatial distributions that represent what an actual PRISM dataset may look like in a future year. Due to the spatial domain of the PRISM data set, we truncated basins that cross the US–Canada border to only include pixels within the US, as it was impossible to estimate the bias and error needed to generate synthetic PRISM PDD and cumulative temperature fields in Canada.

4.3.6 Data groups for peak SWE prediction

These synthetic observational datasets were then used to train a series of different distributed SWE prediction data models. We established several dataset scenarios whereby different combinations of observational datasets are used as predictors of peak SWE, noting that these synthetic variables could very plausibly be used as predictors of peak SWE because they are all currently operationally available. The five predictors dataset groups are as follows:

1. Peak SWE at the pixel containing a snow pillow site, latitude, longitude
2. Data in (1) with added elevation, slope, and aspect
3. Data in (2) with added synthetic fractional snow-covered area (fSCA) at each pixel
4. Data in (3) with added synthetic PRISM cumulative precipitation, cumulative snowfall, PDD, and mean seasonal temperature
5. Data in (4) with added synthetic sub-orbital lidar-based SWE at April 1$\pm$ 10 days

These dataset groups were further grouped into three categories. Groups 1 and 2 ("snow pillow") represent a version of current practices in which topography and snow pillow data are the main drivers of distributed SWE estimation. Groups 3 and 4 ("gridded") represent the addition of relevant, approximately real-time remote sensing (3) and/or reanalysis (4) data but which only loosely constrain SWE estimates. These datasets, while not generally currently used in most basins to support SWE estimation, are realistically available for the entire WUS without any local expenditures or targeted measurement campaigns. Furthermore, a recent study (Mital et al., 2022b) showed that these datasets (scenarios 3 and 4) are drivers that tightly constrain the physical processes governing snow accumulation and melt in the Upper Colorado River Basin. We accumulated these variables from October 1 (i.e., the start of the water year) through April 1 (of the same water year). Lastly, dataset group 5 ("intensive") represents a heavily observed basin with significant targeted measurements. These measurements tend to be in highly researched basins with funding available to pay for

extensive campaigns (Varadharajan et al., 2019). For example, the Tuolumne River Basin in California and the East River Watershed in Colorado had near-April 1 ASO measurements in 2023 and thus have highly constrained SWE estimates (Fleming et al., 2021).

4.3.7 Models for peak SWE prediction

We established the following space of data models to explore the impact of increasing model complexity for predicting spatially distributed SWE:

1. Linear regression
2. Random forest
3. U-Net

Linear regression methods represent the simplest data model and seek to predict snowpack as a linear function of a set of input variables that are connected to and predictive of the processes that control peak SWE in a given area. Random Forest methods (Breiman, 2001) add a layer of complexity to model predictions by enabling a non-linear mapping between input(s) and peak SWE. They consist of an ensemble of regression trees, which seek to minimize the model loss by recursively partitioning the input into smaller subspaces. Each regression tree picks a random subset of data points and a random subset of input features for training. The final model output is obtained by taking an average (or ensemble) prediction of all the regression trees. We implemented random forests using Python's scikit-learn module (Pedregosa et al., 2011) and used the hyperparameter values recommended by the developers of this method (https://CRAN.R-project.org/package=randomForest). We used 500 trees, considered p/3 features when looking for the best node split (where p is the number of input features), and specified a node size of 5. Random forests have been shown to work well with these hyperparameter values for predicting snowpack (Mital et al., 2022b).

Finally, we also considered U-Nets (Ronneberger et al., 2015), which adds another layer of complexity to model predictions by imposing spatial constraints on the non-linear mapping between snowpack and input. Spatial constraints imply that pixels that are close to each other will be more correlated than pixels that are further away from each other. U-Nets achieve this by virtue of being fully convolutional neural networks. They also use an encoder-decoder architecture to ensure that only the most relevant information is considered while learning a functional mapping. U-Nets also implement skip connections between the encoding and decoding paths to ensure that there is no information loss during the encoding-decoding process. This results in the model learning a precise mapping between its inputs and its outputs. We implemented U-Nets using the `tensorflow` module in python (Abadi et al., 2015). We used an architecture similar to the original architecture with modifications as shown in Figure A.4. Since the input for a given year was a single 2-d image (with multiple channels corresponding to the number of input features), we used a bounding box around each HUC6 basin. The encoder (left side) consisted of a repeated application of two 3x3

convolutions (each padded with zeros and followed by a rectified linear unit) and a 2x2 max pooling operation to contract the input. Each downsampling step involved doubling the number of feature channels. We did three contractive iterations, which meant the bounding box for each basin needed to be expanded such that its dimensions were a multiple of 8. Additional contractions were not considered due to computational expense. The decoder (right side) consisted of a 3x3 transposed convolution that upsampled the inputs by a factor of 2 and halved the number of feature channels. This was concatenated (via a skip connection) with the corresponding hidden layer from the encoder path and then subjected to two 3x3 convolutions (as described for the encoder path). The above steps were repeated until the original height and width of the input were recovered. Following this approach, the output was obtained by subjecting the decoder output to a 1x1 convolution. The first encoder layer consisted of 64 channels, which resulted in a U-Net model with ∼8.6 million parameters. We then clipped the output to the actual basin boundaries.

Other machine learning models have been successfully implemented for distributed SWE prediction (Cui et al., 2023; Mital et al., 2022a); the choice of U-Nets for this work is motivated by the portability and 2-D nature of U-Nets, in addition to their relatively straightforward implementation. All the models were trained on the Perlmutter supercomputer CPU provided by the National Energy Research Scientific Computing Center (NERSC). For the entire study area, the linear regression models took about 20 min to train on a single core. The random forests models took 90 min to train using 128 cores. The U-Net models took 12 h to train using 2048 cores.

4.4 Results

4.4.1 Snow and snow pillow sensitivity to climate change

The ability of the snow pillow networks to represent unobserved snowpack will be increasingly impacted by changing snow, precipitation, and temperature. Figure 4.2 shows how those impacts are expected to manifest.

Figure 4.2a indicates the expected year at which the 918 snow pillow stations in the WUS (excluding Alaska) will exhibit substantial degradation in peak SWE sensitivity. The metric of degradation is when the peak SWE at that station is ¡10% of its 1980–2015 average for more than 5 of the previous 10 years, which is based on an existing percentile-based low-to-no-snow definition (Siirila-Woodburn et al., 2021) but better-suited to locations with low interannual variability within the baseline period. Figure 4.2b shows that the lower elevations (below 2000 masl) will become increasingly snow-free by mid-century, while the higher elevations will become snow-free later in the century. Figure 4.2c–h shows the rising snowline elevation at several basins across the West in three decades: 1980–90, 2050–60, and 2090–2100.

Finally, Fig. 2h–l highlights the long-term decline in snow pattern repeatability (shown in black and quantified with average R2 between current-year normalized SWE and the

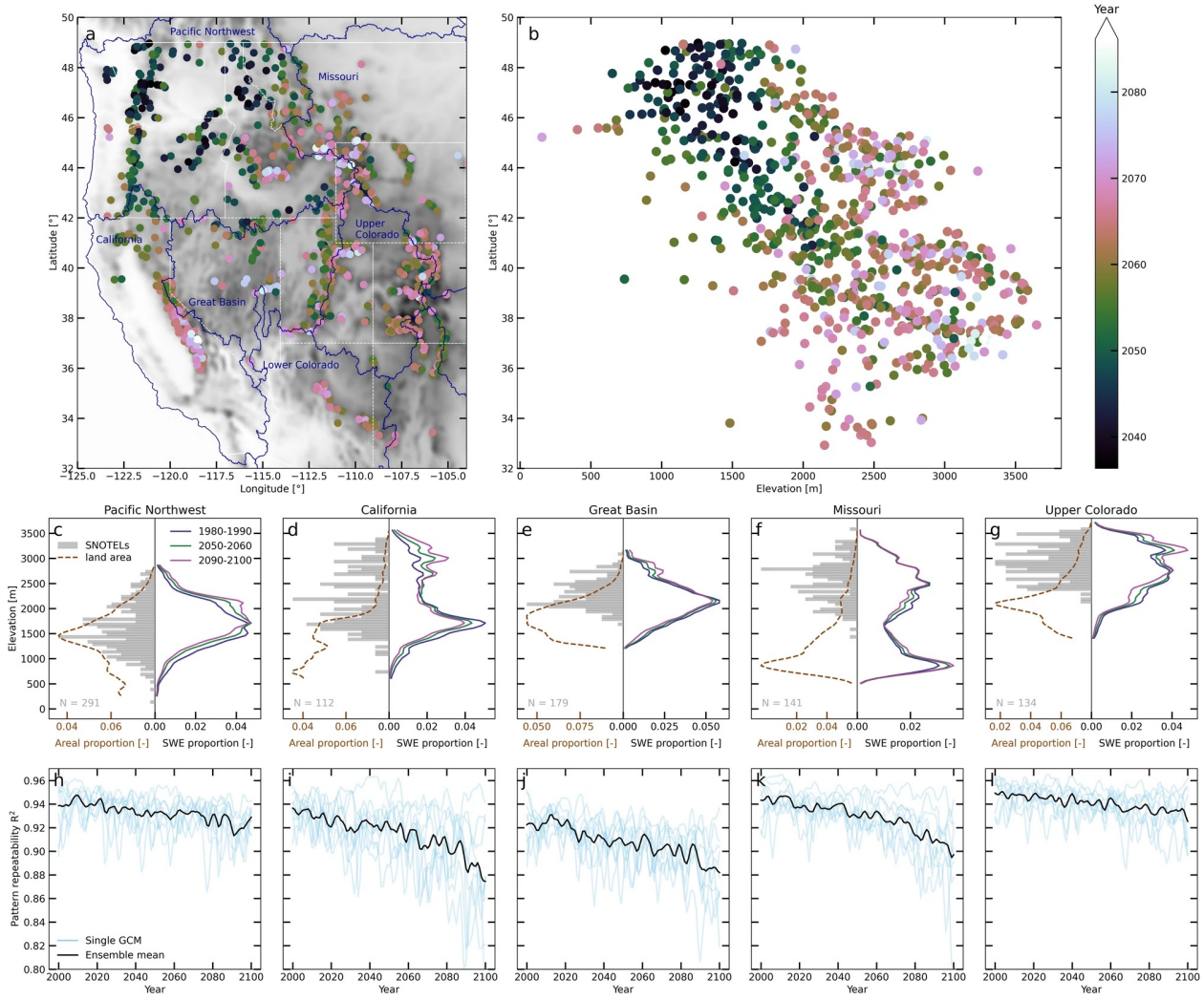

Figure 4.2: a) The year at which half of snow pillow peak SWE values are expected to be ¡10% of their historical average. b) The same metric as a but plotted as a function of elevation and latitude. The distribution of snow pillow stations (gray bars) and land (brown dashed line) with respect to elevation opposite the elevation distribution of peak SWE for 1980–1990 (blue), 2050–2060 (green), and 2090–2100 (pink), for the c) Pacific Northwest, d) California, e) Great Basin, f) Missouri, and g) Upper Colorado basins. h–l) SWE pattern repeatability for basins in c–g for each individual GCM (blue lines, mean in black).

previous 20 years of the same, see the "Methods" section for details) from 2000 to 2100, punctuated by years with far less pattern repeatability than the historical average. Across the ensemble of simulations, future years are predicted to contain different within-basin snow patterns relative to the recent past; in other words, the interannual variability in spatial SWE patterns is predicted to increase. Furthermore, Fig. 2h–l shows that the high level of peak SWE interannual pattern repeatability (Sturm & Wagner, 2010) found in the historical record (Fang et al., 2023; Pflug & Lundquist, 2020) is expected to decline, but at different rates in each region.

4.4.2 Climate-resilient peak snow estimation

We conduct experiments to determine the forcing data and model structures that will maintain SWE estimation skills in future climates. These experiments entail establishing a range of input data sets and statistical models for distributed SWE estimation and applying them to the WUS-D3. We evaluate the relative impact of snow pillow observations, ancillary datasets, and comprehensive snow survey observations (e.g., ref. (Painter et al., 2016)) on peak SWE estimation skills as used as inputs to linear regression, random forest, and U-Net convolutional neural network models.

We simulate three levels of forcing data from observations that can be used to estimate peak SWE across a basin: (1) snow pillow peak SWE observations alone, (2) snow pillow peak SWE observations augmented with gridded meteorology and (3), (1) and (2) along with intensive, gridded observational estimates of SWE (such as with remotely-sensed, high-resolution lidar data (Painter et al., 2016)). These inputs are simulated in historical and future years by extracting the relevant fields from the WUS-D3 dataset corresponding to those observational levels, creating observational drivers, and adding synthetic error to those drivers (see the "Methods" section).

We estimate pixel-wise peak SWE with three data modeling procedures in order of increasing complexity: (1) linear regression, (2) random forests (Breiman, 2001), and (3) U-Nets (Ronneberger et al., 2015). Traditionally, operational SWE and runoff forecasting in snow-dominated watersheds has relied on the first of these procedures: empirical development of linear relationships between snow measured at local (i.e., in the same watershed) snow pillow stations and distributed SWE (Zuzel & Cox, 1978). We, therefore, use linear regression to replicate the assumptions of status quo approaches. The implementation of random forests then allows for explicit non-linear relationships between input data and distributed peak SWE. Lastly, U-Nets preserve spatial correlations within the outputs in addition to capturing nonlinearity.

In reality, we expect neither observational information nor data models to be static as snow volumes and patterns change. Therefore, we trained all models on the previous 20 years of data (see the "Methods" section) to reflect current water management and drought definition practices (Garen, 1992; Pagano et al., 2009). Figures 3 and 4 show the coefficient of determination (R^2) between the WUS-D3 peak SWE value and the modeled estimate of that value for each experimental configuration (i.e., forcing data and model choice).

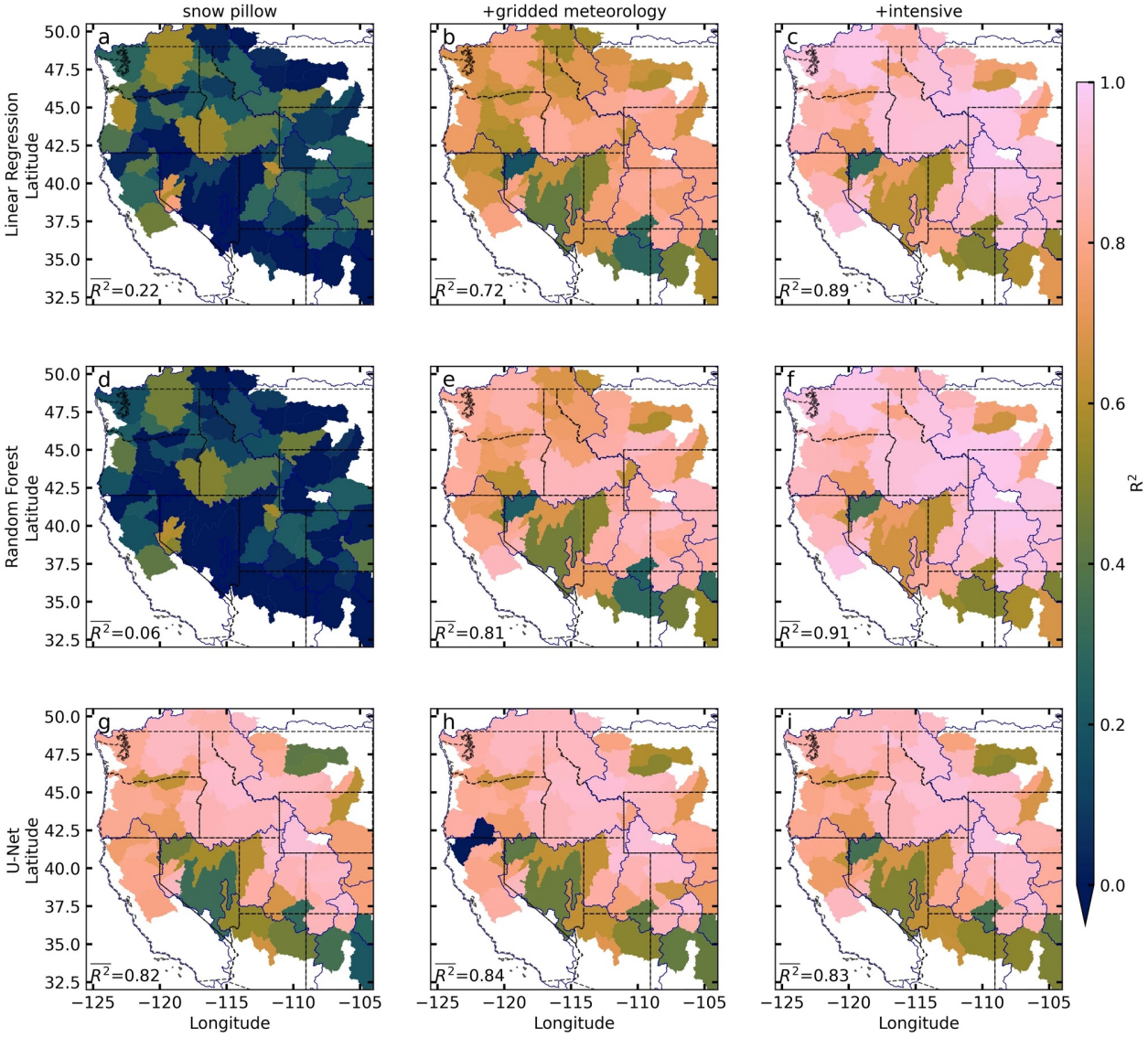

Figure 4.3: Time-averaged (1980–2100) basin-wide coefficient of determination (R2) between WUS-D3 peak SWE and the peak SWE predicted from each experimental configuration for each snowy HUC6 basin in the Western United States. Row indicates estimation model as linear regression (a–c), random forest (d–h), or U-Net (g–i); columns indicate input data as snow pillow (a, d, g), +gridded (b, e, h), or +intensive (c, f, i). Color indicates R^2 value.

Figure 4.3 shows that more observational information and/or higher data model complexity yields higher R^2 values. Consequently, the inclusion of more observations (e.g., gridded meteorology and intensive monitoring) and higher complexity models (e.g., random forest or U-Net) enables more accurate estimates of the spatial patterns of peak SWE throughout the 21st century. This figure also shows that while it will be challenging to estimate peak SWE in some catchments with low and/or intermittent snow cover (e.g., the Lower Colorado River Basin and Nevada), estimates of peak SWE can greatly benefit from additional observations and higher-complexity data models. These additional observations and complex models are able to inject information about new spatial relationships between measured and non-measured locations and the response of old spatial relationships to a new climate.

Figure 4.4 further explores the importance of observations and model complexity for peak SWE prediction across the WUS, highlighting that all predictions decrease in skill into the future as year-to-year variability in snow increases. However, the skill of the U-Net is far greater than the skill of linear regression when forced with snow pillow SWE alone or with gridded meteorology (Fig. 4.4b–d). The accordion plots in Fig. 4.4a show high skill in predictions that use a U-Net or at least gridded meteorology. The U-Net and gridded meteorology both explicitly include two-dimensional spatial patterns, while the snow pillow locations, random forest, and linear regression do not. With gridded meteorology, the added value from higher complexity models is smaller than with linear regression but still present. Intensive observations make complex modeling unnecessary or even counterproductive. Figure 4.4b–d shows time sequences of R^2 for each data-model combination, indicating that the U-Net consistently achieves higher skill. Even in future water years, the U-Net model retains R^2 generally above 0.75.

Figure 4.4e–g shows performance increases from implementing U-Nets in place of linear regression. The lower performance in the historical year (yellow) compared to the end-of-century year (blue) is consistent across forcing data categories, but the decline is lower for U-Nets (y-axis) than for linear regression (x-axis). The salient features of the random forest and U-Net are their ability to model nonlinear relationships and that the U-Net explicitly encodes spatial correlations while linear regression and random-forest models are point-specific. These findings suggest that encoding spatial correlations will become increasingly important for peak SWE estimation. While historical performance has less inter-model and inter-basin variance, the snow pillow and gridded cases show consistent improvements from U-Net implementation. Because each model is trained on the previous 20 years of data, the decline in performance toward the end of the century in all data and model cases indicates that snow distributions are changing faster than the spatial models can adapt.

4.5 Discussion

The ability of observational networks such as SNOTEL to inform estimates of distributed SWE fields in future climates is likely to decrease. As the climate warms, the snow line elevation will rise while some colder regions will receive increased snowfall, resulting in novel

spatial distributions of snow. There are substantial water resource management implications to this reduced capability (Georgakakos et al., 1998): retaining or releasing water in ways that do not reflect the true volume of snowpack can lead to misallocation. To that end, intraseasonal management choices rely on awareness of peak SWE and its spatial distribution (Barnhart et al., 2016; McCabe et al., 2017; Musselman et al., 2018). A warming climate will also shift the within-season temporal distribution of SWE; the methods evaluated here could be applied at any time during the snow season in order to optimally inform management.

We find that the challenges that existing WUS SWE estimation capabilities will face in the 21st century can be partially offset by expanding the observations used to estimate SWE, even if they only loosely constrain SWE, or by adopting data-driven, spatially aware statistical models. In this framework, each year's predictions depend on patterns learned from the previous 20 years. Declining predictive skill near end-of-century therefore reflects an acceleration of change. Even in a year with a new extreme climate, any observation in the current year can lend insight to the potentially novel pattern. However, sparse observations (e.g., snow pillows) will require nimble, 2D methods (e.g., U-Net), while dense observations (e.g., gridded meteorology) can make do with more straightforward relationships between observation and output.

We provide baseline quantification of the performance gains possible from each effort. Implementing U-Nets in the snow pillow-only data scenario improves skill more than adding gridded meteorological data to a linear regression model but less than adding intensive SWE observations. However, the U-Net models implemented here approach the performance of intensive airborne SWE measurements even using just snow pillow station measurements; adding gridded meteorological data slightly improves mean performance and decreases inter-basin variance. Implementing U-Nets in the intensive case decreases performance, likely due to overfitting.

It is important to recognize the ecological and management challenges that future extreme low water years (e.g., shown in Fig. 4e–g) will create. The importance of accurate estimation for management will be acutely greater than it has been in the past. The data-driven models and multiple modalities of datasets for SWE prediction can be quickly developed, tested, and deployed using mature software workflows. In the middle of winter in ahistorical years, rapid SWE prediction system implementation may be warranted or required. Although not explored here, we also hypothesize that similar methods could be used for intra-seasonal temporal (rather than spatial) predictions, further increasing the utility of intensive measurement campaigns.

The snow-targeting remote sensing of the future will also contribute to the solution of this problem. Achieving climate change-resilient snowpack estimation should incorporate better and more widespread observations (de Boer et al., 2023; Feldman et al., 2023) and update data-driven statistical modeling (Fleming et al., 2021). Importantly, most remote sensing relies on in situ measurements for calibration and validation. Water management is inherently local, and as such catchment-specific methods combining remote sensing, observations, and physics-based modeling (e.g., Hedrick et al., 2018) will continue to provide valuable insights. The methods developed here, however, leverage only existing measurements and, therefore,

can be broadly and immediately applied.

Lastly, the finding that more complex models are needed to maintain SWE prediction skills does not necessarily equate to a requirement to use an artificial intelligence (AI) method, such as U-Net. Conventional approaches, including observation-based reanalysis estimates, are no less relevant to peak SWE estimation than AI. Indeed, they are driven by the same observational information that would drive AI models and contain parameterized representations of causally related atmospheric and surface processes. At the same time, the community of AI practitioners is both large and nimble. In other words, AI models can be rapidly developed to emulate atmospheric and surface processes while also managing multiple observational modalities (Schneider et al., 2023). While the results of this work are not necessarily prescriptive for requiring the use of AI for WUS peak SWE estimation in the future, they are prescriptive for implementing nimble, multi-modal predictors of distributed SWE. AI algorithms, with their current capabilities, represent one such solution that can provide timely SWE information for water resource managers, scientists, and the large populations that rely on snowpack.

Figure 4.3 shows that more observational information and/or higher data model complexity yields higher R2 values. Consequently, the inclusion of more observations (e.g., gridded meteorology and intensive monitoring) and higher complexity models (e.g., random forest or U-Net) enables more accurate estimates of the spatial patterns of peak SWE throughout the 21st century. This figure also shows that while it will be challenging to estimate peak SWE in some catchments with low and/or intermittent snow cover (e.g., the Lower Colorado River Basin and Nevada), estimates of peak SWE can greatly benefit from additional observations and higher-complexity data models. These additional observations and complex models are able to inject information about new spatial relationships between measured and non-measured locations and the response of old spatial relationships to a new climate.

Figure 4.4 further explores the importance of observations and model complexity for peak SWE prediction across the WUS, highlighting that all predictions decrease in skill into the future as year-to-year variability in snow increases. However, the skill of the U-Net is far greater than the skill of linear regression when forced with snow pillow SWE alone or with gridded meteorology (Fig. 4.4b–d). The accordion plots in Fig. 4.4a show high skill in predictions that use a U-Net or at least gridded meteorology. The U-Net and gridded meteorology both explicitly include two-dimensional spatial patterns, while the snow pillow locations, random forest, and linear regression do not. With gridded meteorology, the added value from higher complexity models is smaller than with linear regression but still present. Intensive observations make complex modeling unnecessary or even counterproductive. Figure 4.4b–d shows time sequences of R2 for each data-model combination, indicating that the U-Net consistently achieves higher skill. Even in future water years, the U-Net model retains R2 generally above 0.75.

Figure 4.4e–g shows performance increases from implementing U-Nets in place of linear regression. The lower performance in the historical year (yellow) compared to the end-of-century year (blue) is consistent across forcing data categories, but the decline is lower for U-Nets (y-axis) than for linear regression (x-axis). The salient features of the random forest

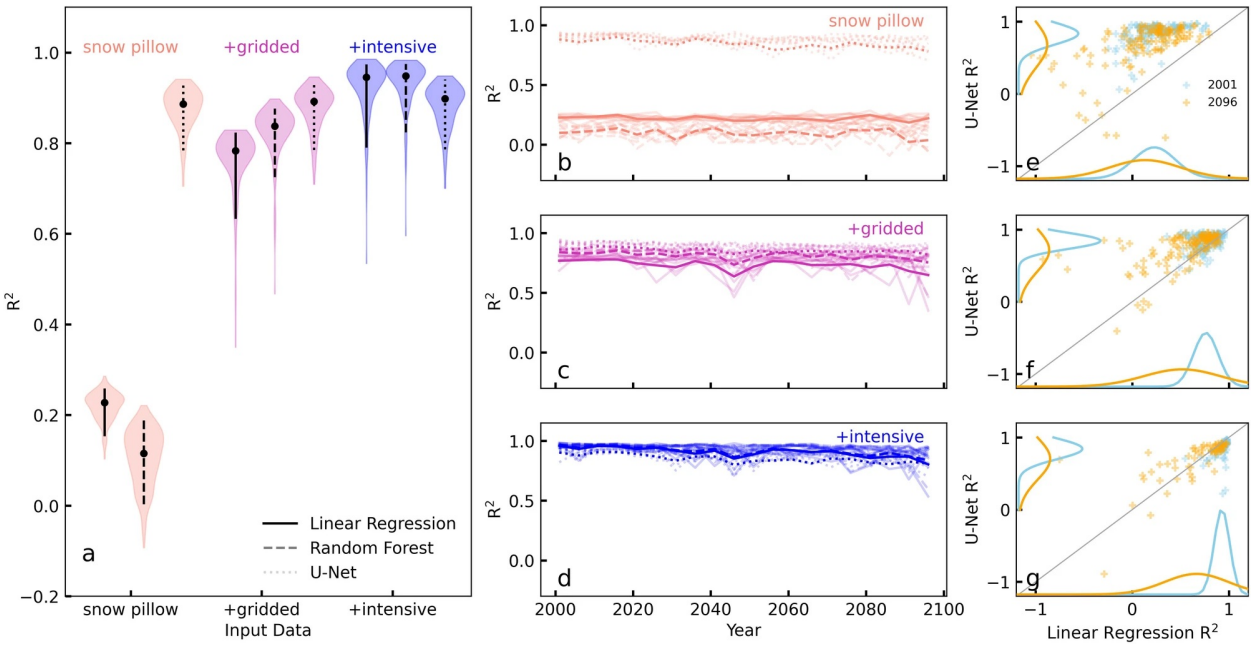

Figure 4.4: a) Average pixel-wise coefficient of determination (R^2) between predicted and WUS-D3 peak SWE for each input data level and estimation model combination tested: linear regression (solid), random forest (dashed), and U-Net (dotted); forcing data from snow pillow locations (orange), +gridded (pink), +intensive (blue); dots indicate medians, lines indicate interquartile range. b–d) Quantities in (a) as they change over time. e–g) The distribution of R2 values for the linear regression (x-axis) and U-Net (y-axis) in time, from 2001 (blue) to 2096 (yellow), for each data forcing category.

and U-Net are their ability to model nonlinear relationships and that the U-Net explicitly encodes spatial correlations while linear regression and random-forest models are point-specific. These findings suggest that encoding spatial correlations will become increasingly important for peak SWE estimation. While historical performance has less inter-model and inter-basin variance, the snow pillow and gridded cases show consistent improvements from U-Net implementation. Because each model is trained on the previous 20 years of data, the decline in performance toward the end of the century in all data and model cases indicates that snow distributions are changing faster than the spatial models can adapt.

4.6 Data availability

All data used in this project are freely available and accessible to the public. The data used in this work come from the SNOTEL network (https://www.nrcs.usda.gov/wps/portal/wcc/home/quicklinks/imap), the CCSS snow pillow network (https://cdec.water.ca.gov/snow/)

the Airborne Snow Observatories (https://data.airbornesnowobservatories.com/), the Surface Atmosphere Integrated Laboratory (https://adc.arm.gov/discovery/#/results/site_code::guc) and the PRISM project (https://www.prism.oregonstate.edu/). The ensemble of dynamically downscaled GCM outputs are detailed in Rahimi et al. (2023) and available, with overview documentation, here: https://registry.opendata.aws/wrf-cmip6/. Data products created in this project are archived at https://zenodo.org/uploads/10269717.

4.7 Code availability

The code used to generate the findings and figures in this project is available in its archived form at https://doi.org/10.5281/zenodo.11111276 and maintained at https://github.com/mariannecowherd/resilient-snowpack-estimation/.

Chapter 5

Vegetation and topographic controls on post-fire snowpack: Evidence from the 2021 Caldor Fire[1]

"The current American landscape represents the historical legacy of one worldview superimposed on another, the colonial overlaying the indigenous. Nowhere is this history more apparent than in the attitudes toward fire, attitudes made manifest on the landscape." – Robin Wall Kimmerer and Frank Kanawha Lake, Journal of Forestry, 2001

5.1 Abstract

The increase in wildland fires in recent decades due to long-term fire suppression policies and increasingly favorable climate factors has also increased the elevation range of wildland fires. In the mountainous western United States, this has led to an increasing influence of fire on landscape-level vegetation patterns in snow-dominated ecosystems. The resulting hydrological implications of these fire-driven changes in vegetation patterns are being studied. In forests, fires consume surface fuels and understory vegetation, reduce tree canopy cover, darken tree boles, and deposit ash. The combination of these impacts alters the amount and timing of snow accumulation and persistence in an area compared to pre-fire conditions. In this study, we use field measurements, remote sensing, and modeling of snow and fire conditions within the footprint of the Caldor Fire, a large wildland fire in the central Sierra Nevada, California, that burned in 2021. Our goal is to describe and explain the variability in snow accumulation and persistence and to compare these findings to the long-term measurement history at snow course stations within and near the wildfire footprint. We show that north-facing slopes at mid- to high elevation saw snowpack accumulation benefit from fire, especially in areas burned at low and moderate severity. Other elevations, aspects, and

[1]This chapter was submitted for publication in 2025 as Cowherd, M., Schwartz, A., Marks, J., Collins, B., Kim, L., Brandt, G., Stephens, S., and Girotto, M. and is reproduced here with permission of the authors.

fire severity classes experienced decreases in snowpack. Compared to established snow measurement sites, this response to fire led to deviations in the behavior of snowpack throughout the burned area. This work shows how the locations of established monitoring sites differ from the surrounding basin in their response to a major disturbance and can inform the interpretation of snow measurements in post-fire landscapes.

5.2 Introduction

The location and volume of snow are a desirable mapped quantity due to their direct relationship with ecosystem function and water resources (Molotch & Bales, 2005). Snowpack distribution has implications for melt timing, speed, and volume and resulting hazard and management implications. The difficulties in obtaining accurate distributed direct measurements require a system of point measurements through established snow measurement stations in a network, which are then used in a series of empirical models to predict distributed values (Dozier et al., 2016). Remotely sensed measurements are sometimes used in conjunction with network measurements, but are limited by their general inability to measure snow density, volume, or depth; coarse temporal and/or spatial resolution; discontinuous spatial domain; and/or cost (Bormann et al., 2018). Snow pillows, of which there are more than 1000 in the western US, provide daily snow water equivalent (SWE), depth, and meteorological measurements (Serreze et al., 1999). State agencies, including the California Department of Water Resources, operate additional measurement stations, including daily-to-monthly SWE and snow depth measurements (Natural Resources Conservation Center, 2008).

Forests are an integral component of mountain hydrological systems due to the myriad of interactions between vegetation and water in all phases. Forest-snow interactions affect snowpack storage and melt timing in large areas of the seasonal snow zone (Lundquist et al., 2013; Roturier & Roué, 2009; Varhola et al., 2010). These interactions are complex, multidirectional, and dynamic. Intense forest and/or snow disturbances, such as snow drought (Harpold et al., 2017), snow deluge (Marshall et al., 2024), and wildland fire (Kampf et al., 2022) are opportunities to study the underlying mechanisms of the forest-snow relationship as well as threats to human activity and management. The multidimensional nature of the role of vegetation in hydrology means that similar vegetation disturbance scenarios can induce opposite responses in snow distribution, volume, and melt timing (Lundquist et al., 2013; Stevens, 2017; Teich et al., 2022). In the 20th and 21st centuries in the western United States, the dominant mechanisms for wide-scale (i.e., >10,000 ha) forest structure modification are commercial timber operations and wildland fire (Hessburg & Agee, 2003; North et al., 2012).

In the western United States, forest management and climate change are increasingly affecting snow accumulation and melt. Historical frequent-fire forests are considerably denser today than at any point in history due to widespread fire suppression (Knight et al., 2022; Stephens et al., 2015). Snow that persists until spring melt is depleted by vegetation before

entering streamflow (Molotch et al., 2009). High forest canopy cover can intercept meaningful amounts of incoming snowfall, leaving snow more susceptible to midwinter sublimation (Pomeroy et al., 2002). However, snow that passes through the canopy benefits from additional shade during the spring, delaying melt and preventing sublimation from the surface (Koivusalo & Kokkonen, 2002). Warming temperatures also increase the vapor pressure deficit, in turn increasing winter sublimation, driving higher vegetation water demand, and higher surface and soil water evaporation (Sexstone et al., 2018). Physical modeling of snow-forest interactions can quantify the effects of forest characteristics on snowpack from the tree to the catchment scale (Broxton et al., 2015; Webster et al., 2016), but do not necessarily represent the response of a region to a major disturbance to soil, vegetation, and albedo, such as from wildland fire.

Fire suppression and climate change together have contributed to increases in the frequency, severity, size, and elevation range of wildland fires (Gergel et al., 2017). When these fires burn snow-fed watersheds, the impacts of the fire stretch from the treetops to the root zone. Wildland fires that occur in the seasonal snow zone almost exclusively burn in the summer and fall and then affect snowpack in the following winter and spring seasons, with declining impact over the years proportional to the post-fire recovery and/or landscape transition of the forested area (Gleason et al., 2019; Goss et al., 2020). Fires impact snow hydrology by reducing vegetation (Boisramé et al., 2017; Moeser et al., 2020) and depositing black carbon on the snow surface throughout the winter (Gleason et al., 2013). Further impacts on the fate of snowmelt, such as increasing soil hydrophobicity and worsening water quality co-occur, but do not necessarily change the amount, distribution, or timing of snow melt (Koshkin et al., 2022; Paul et al., 2022).

Case studies of post-fire snow and broader hydrologic impacts have been conducted in forests throughout the Western United States. Boisramé et al. (2018) and Boisramé et al. (2019) found an increase in snow and soil moisture retention in newly created wetlands after decades of restored lightning fire in a high-elevation watershed. The shorter-term effects of fire include increased accumulation in high severity burn patches (Collins & Stephens, 2010; Kampf et al., 2022) and albedo losses from deposition of ash and other black and brown carbon particles into and on top of snow (Gleason et al., 2013). However, the relative magnitude of these mechanisms and how they vary with topography, climate, spatial scales, and other conditions, are not fully understood (e.g. Maxwell et al., 2019; Stevens, 2017).

Covariance between drivers of energy and mass balance terms contributes to this entanglement. Stevens (2017) analyzed fine scale snow survey data from three Sierra Nevada and south Cascades fires in the 2013-14 winter; in these fire footprints, snowpack outcomes depended on the spatial scale over which they are assessed. Fire generally decreased basin-wide snow depth, but open areas tend to have higher snow depth than under-tree areas, even in burned areas. This dependence is further influenced by the region's temperature. Efforts to isolate the effects of individual components of fire impacts on snowpack, such as black carbon deposition, reveal that burned regions see a decrease in peak snow from black carbon deposition and the resulting increased radiative forcing (Gleason et al., 2019).

In the context of increasing frequency, severity, and size of wildland fires, fire is a major

source of uncertainty as to how forests are and will modulate snow accumulation and ablation in current and future climate and fire scenarios (Attiwill & Binkley, 2013; Boon, 2012; Rakhmatulina et al., 2021). The diverse documented effects of wildland fire on vegetation patterns, and subsequently on snow, necessarily interact with established systems for measuring and predicting snow distribution during the winter season. In this work, we use the 2021 Caldor Fire, which burned nearly 90,000 hectares in the central Sierra Nevada, California, to empirically explore the changes in snowpack spatial distribution after wildland fire. We draw on a suite of data products from field observations, airborne and satellite remote sensing, and established snow monitoring sites to evaluate the snow management landscape following a major disturbance.

5.3 Data and Methods

5.3.1 Study Site

The Caldor Fire ignited on 14 August, 2021 and burned 89760 hectares in El Dorado, Amador, and Alpine Counties in California, United States. Before its containment on 21 October of the same year, it breached the Echo Pass ridge from west to east and triggered evacuations of communities in the South Lake Tahoe area. At the time, it was the 15th-largest fire in California; the cause of the Caldor Fire has not been definitively determined at present.

In addition to being a megafire (>40,000 hectares burned), the Caldor Fire included large high-severity patches and a relatively large total area of high severity burn, in part due to high fuel loads in the region. Few recent fires within the burned area had occurred, except for the 2019 Caples Fire (∼1400 ha) around which the Caldor Fire burned, resulting in ample dry fuel throughout the region. The Caldor Fire burned in the South Fork American, Mokelumne, Upper Cosumnes and Lake Tahoe basins; in this study, we only consider the Caldor's effects on the South Fork American basin. This region is the largest total area burned as well as the largest snow-covered area burned. Approximately 73% of the Caldor Fire scar regularly (> 75% of years from 2000-2020) receives winter snowfall, including ∼100% of the burned area inside the South Fork American River Basin. The South Fork American is one of the headwaters of the American River system and is used as a municipal water supply for Sacramento and is a source of irrigation for the California Central Valley. All mentions of the study domain within the Caldor Fire hereafter refer to the South Fork American River basin subset of the total burned area.

5.3.2 Snow course and pillow data

Six snow course or automated snow depth sensor sites managed by the California Department of Water Resources (CADWR) within the burned area were selected for this study (Table 5.1, Figure 5.1 pink stars). At the snow course sites, manual measurements of snow depth and

mass are conducted by cooperators in the first week of each winter month (i.e., starting in January) with meaningful snow. At the Caples Lake snow course, an automated sensor and snow pillow records snow depth and SWE; at the Alpha snow course, a snow pillow records SWE. All of the snow courses in this region have data records extending to the 1960s, with most beginning between 1939 and 1941. All data were retrieved from the California Data Exchange Center (CDEC, https://cdec.water.ca.gov/) portal for the California Cooperative Snow Survey (CCSS) on November 11, 2024.

Table 5.1: Snow course or sensor name and information. Year indicates the year in which the snow course or sensor first published data; all sites are maintained to present day but may have missing data. *sites with daily automated snow depth, $^{+}$ sites with automated snow water equivalent, where there is also a snow pillow or other sensor installed at the same location as the snow course. Elevations reflect approximations made in public reporting.

Name	**Acronym**	**Latitude**	**Longitude**	**Elevation** [m]	**Year**
Lake Audrain	ABN	38.81983	-120.0393	2225	1941
Philipps	PHL	38.81800	-120.02700	2070	1941
Caples Lake$^{*,+}$	CAP	38.71079	-120.04158	2400	1939
Tamarack Flat	TMF	38.80300	-120.10300	2000	1939
Alpha^{+}	ALP	38.80414	-120.21564	2310	1965
Echo Summit	ECS	38.82852	-120.03898	2300	1940
Forni Rige$^{*,+}$	FRN	38.80397	-120.215919	2316	1980

5.3.3 Remotely sensed snow, fire, and forest data

In this work, we use airborne and satellite-based remote sensing data to retrieve snow and forest-related quantities. We use fractional snow-covered area (fSCA) products from the Moderate Resolution Imaging Spectrometer (MODIS) instrument (MOD10A1) from 2000-present at daily temporal resolution and 500-m spatial resolution (https://nsidc.org/data/mod10a1/versions/61). Quality control flags within the MOD10A1 product were used to filter low-quality images from the collection. Pixel-wise masks for cloud cover were removed from remaining high-quality images. The resulting quality controlled MOD10A1 product reports, for each pixel in the image, a value between 0 and 100 representing the fraction of that pixel that is likely covered with snow (Hall & Riggs, 2021).

Airborne Snow Observatories (ASO, Painter et al., 2016) flights over the Caldor Fire burn area occurred after the Caldor fire, on January 31, April 13, April 28, and June 2, 2023 for the 2022-23 winter. The resulting lidar-derived snow depth maps at 3- and 50-m resolution provide the most spatially complete snow depth estimates over the region. We use 50-m resolution snow depth products in this study for comparisons of snow depths between burn severity categories. Higher-resolution snow depth products would not necessarily result in greater insight when analyzed at the scale of a natively coarser burn severity map. Figure

5.2a shows average 2000-2020 winter snow cover fraction from MODIS NDSI snow cover fraction from the SnowMetrics Snow Cover Fraction product (Crumley et al., 2020).

We use burn severity data, expressed as Relativized differenced Normalized Burn Ratio (RdNBR), from the 30-m resolution Monitoring Trends in Burn Severity (MTBS, https://mtbs.gov) for the Caldor Fire. The RdNBR is calculated from the normalized burn ratio (NBR), where NBR = $\frac{\text{NIR}-\text{SWIR}}{\text{NIR}+\text{SWIR}}$; NIR = near infrared, SWIR = shortwave infrared, for pre- and post-fire satellite images: dNBR = $\text{NBR}_{\text{post}} - \text{NBR}_{\text{pre}}$. The difference of the two is normalized by the square root of the pre-fire scene: RdNBR = $\frac{\text{dNBR}}{\sqrt{|\text{NBR}_{\text{pre}}|/1000}}$ to accurately capture the impact of the fire, independent of pre-fire conditions (Miller & Thode, 2007). For the Caldor Fire, the pre-fire conditions were captured on 5 August 2021 and post-fire conditions on July 23, 2022. Figure 5.2b shows MTBS RdNBR classifications into areas of unburned, low-severity, moderate-severity, and high-severity fire, using cutoffs from Miller and Thode (2007).

We use 30-m resolution canopy cover from LANDFIRE Existing Vegetation Cover and Forest Canopy Cover (LFCC) from 2020 and 2022 (LANDFIRE, 2022; Nelson et al., 2013) to represent pre- and post-fire canopy conditions, respectively. Forest cover patch size is calculated from LFCC 2022 (post-fire) by grouping contiguous grid cells of canopy cover reported in bins of 10 percentiles. Canopy cover change is correlated to burn severity, as the high burn severity class is constructed to reflect stand-replacing fire. Post-fire snow, however, is sensitive to absolute canopy cover and black carbon deposition. Therefore, we used canopy cover to compute patch size of canopy cover classes after the fire in a way that reflects only forest structure, not other processes associated with the reason for lack of canopy cover in a particular location. Patches identified in this mapping approximately correspond to contiguous burn severity pixels, but can also be caused by other mechanisms, such as pre-fire commercial timber activity. We assessed pre-fire forest structure modifications using the Forest Service Activity Tracking System (FACTS, https://data.fs.usda.gov/geodata/edw/datasets.php) from 1995 to 2024. In the study region, approximately 40% of the total area was affected by some type of forest treatment between 1995 and 2021 (Figure S1). However, more than half of this activity took place more than ten years before the fire and the remaining recent treatments are primarily thinning (commercial thin: 6.17% of study area, mechanical thin: 4.09%), pile burn-related (piling: 2.15%, pile burn: 1.93%), or yarding (1.85%). No clear cutting or salvage logging was recorded in the study area between 2010 and 2021.

5.3.4 Field data

During the 2022-2023 winter season, we installed 26 WingScapes TimelapseCam cameras pointed at red, 5-cm diameter PVC poles (Supplementary Figure 3). All poles and cameras were installed between the 5 and 30 of November, 2022. The cameras are grouped into seven geographic areas, with plots at different burn severities in each cluster. Figure 5.1 shows the location of each site; GPS coordinates and other metadata are listed in Supplementary Table

1. At each site, the pole was installed in the ground with a metal T-post. The wildlife camera was installed on a tree facing the pole (Figure S2 shows a representative plot schematic). At each site, the geometry of the pole and camera setup was measured, including the height of the camera, the distance and direction between the pole and the camera, and the height of the pole. Site conditions, including aspect and slope, were measured with a compass, and to assess the forest condition at the site, all trees within 10m of the pole were counted, categorized as small (<10 cm diameter at breast height, diameter at breast height) or large (>10 cm diameter at breast height), and recorded as being alive, red (recently killed foliage still on the tree), or dead (Supplementary Table 2). We took photographs in each cardinal direction and directly upward at each site and conducted a gridded canopy cover survey. In the canopy cover survey, a grid of 25 2.5-m squares with the snow pole at the center was established. The cover directly over each grid point was recorded as no cover, dead tree, red tree, or live tree. All field sites are in mixed conifer forest and all individual trees evaluated are conifers, so all trees have the potential to be in the red phase after the tree has sustained damage and autumn senesence-driven reddening is unlikely (Vollenweider & Günthardt-Goerg, 2005). Half of the field sites included Onset HOBO Pendant Temp/Light 64K data loggers installed at the base of each height pole; the locations of each site and presence of a pendant logger are indicated in Figure 5.1b. Before deployment, all pendant loggers used in this study were cross-calibrated by being placed in a closed box indoors for one week to establish a same-temperature, low-light variance baseline. The cross-sensor variation was under 3% for all sensors during the baseline period.

The time-lapse cameras were programmed to take three photos per day, at 7 am, 10 am, and 3 pm Pacific Daylight Time to ensure a good daylight photo would result from the day, if possible given storm and changing light conditions. Photos are post-processed using manual annotation of the visible pole and converted to real-life depths by comparing the pixel count of the visible pole to the known height of the pole. Photos without a clearly identifiable depth pole are removed from the record. In all camera locations, the pole shifted angle throughout the winter due to extremely high snow loads. In some cases, the metal T-post was found bent at the end of the winter. To correct for this shift, we also recorded the angle of the pole within the camera frame and adjusted the snow depth calculation to account for the geometry of the pole angle. During the winter, several in situ depth measurements taken at some sites and lidar observations from ASO are used for validation of camera data.

The 2022-2023 winter in California, including in the South Fork American basin, was an anomalously high snow year (Marshall et al., 2024). The exceptionally high snow depths and water equivalent contributed to lower than expected data completeness for statewide snow data due to difficult access and sensor overload. Full winter records were only retrievable at four camera sites, primarily due to very high snow depths covering the cameras.

5.3.5 Snow disappearance date

The pendant logger time series data were extracted from the pendants using Onset HOBOware Free after retrieval. Surface air temperature and light intensity data at sites with pendant

logger are used to establish snow cover days. Both the temperature and light intensity time series show significantly depressed rolling standard deviation when covered by snow due to the insulation and albedo properties of snow (Figure S3); these low-variance time periods also correspond to near-zero absolute value of both properties. The redundancy between temperature and light intensity allows for measurement failure of one sensor and helps resolve disagreements or uncertainties between the photo record and a pendant logger record. For each quantity, we estimated snow cover status (snow-on or snow-off) on a daily basis. If the daily standard deviation is over 3 °C (1000 lux), the day is classified as snow-off based on temperature (luminosity) and vice-versa. We then established the melt out day from each quantity as the first day after February 1 where the threshold variance is met and established for more than five days. The February 1 threshold was selected to identify Spring snow disappearance even in cases of ephemeral snowpack at several low-elevation sites.

We calculate the discrepancy between the melt date estimated from the pendant logger and the MODIS remotely sensed fSCA snow covered melt date within the same pixel for the 2023 water year. This represents the difference between the snow ablation mechanisms in the area surrounding the point and the site itself. The MODIS pixel is much larger (i.e., 500 m grid size) than the measurement site, we calculated the relationship between the pendant's relative elevation within a pixel and the difference in melt-out dates observed. This identifies the role that within-pixel elevation gradient has on melt; a pendant at a higher elevation than the pixel mean should observe snow for longer than the total MODIS pixel. While the size of this discrepancy depends on the threshold used to define total snow loss in the fSCA product, there still should be a direct relationship between the threshold and the discrepancy distribution for several pendants at different elevations. The linear best fit between elevation difference and melt date discrepancy had a meaningful trend ($R^2 = 0.63$, p = 0.0003) and is therefore subtracted. We then consider the remaining discrepancy between MODIS melt date and pendant melt date to represent the non-elevation components of melt date variation, such as vegetation and microtopography.

5.3.6 Elevation and aspect mapping by burn severity and canopy patch size

Elevation and aspect are meaningful drivers of snow distribution: elevation because of lapse-driven temperature and precipitation gradients and aspect because of the amount of incoming solar radiation that is direct. We therefore compare snow depth values for locations with different burn severities but with shared elevation and aspect characteristics. For this analysis, we bin RdNBR burn severity into categories from Miller and Thode (2007) as shown in Figure 5.2b. We then match burn severity categories to snow depth values at each ASO acquisition date using $\pi/4$ radian aspect bins and 150-m elevation bins. To assess the difference across a burn severity gradient, we then difference the elevation-aspect grid from unburned regions with the same grid for low, moderate, and high-severity burn regions. The resulting values directly compare snow depths for similar topographic profiles, leaving the

burn-influenced difference remaining, along with possible noise from non-burn-related forest cover or position within broader circulation patterns.

While wildfire is a powerful mechanism for lowering vegetation density and canopy cover, it is not the only reason that a given region may have low canopy cover. We identified canopy gaps in the LFCC post-fire dataset as regions with 10% or lower canopy cover and grouped touching pixels into contiguous gaps. The size of each gap does not necessarily determine the distance of snow within that gap to the nearest canopy cover because gaps may be of many shapes, not just circles. However, the patch shapes identified in the study site are approximately equal on their major and minor axes, so no shape correction was taken. We grouped ASO snow depth data by low-cover patch size and compare elevation-aspect profiles for each acquisition date. We then group patches by their size into large and small patches; small patches are areas of low canopy cover up to 10 hectares and large patches are areas of low canopy over 400 hectares. Results for intermediate-size patches (10-400 hectares) are shown in Supplementary Materials.

5.3.7 Post-fire spatial patterns of snow covered area

We define spatial pattern of snow covered area using the standardized normal variate, a statistical formulation designed to abstract the shape of a distribution away from its magnitude. In the context of snow cover, this means the relative values of snow characteristics in any location are compared to the values at other locations in ways that are theoretically directly comparable no matter the total snowfall for that year. Snow variables have historically shown moderately high pattern repeatability (SWE, Pflug & Lundquist, 2020). Here, we compute the standardized normal variate distributions of monthly MODIS snow cover (MOD10A1, composite snow cover maps) for each winter month across a domain encompassing the Caldor Fire burned area and surrounding regions (see Figure 5.9) from 2018 to 2024, using a standardized normal variate (SNV) to adjust between years with different total snow cover: $SNV = \frac{x-\overline{x}}{\sigma}$, where x is the quantity, $\overline{X}$ is the spatial mean of the quantity on the date of acquisition, and σ is the standard deviation of the same. This standardization allows for direct comparison between winters with different snowfall amounts and seasonal patterns as well as between different months both within and between winters. However, direct comparison does not imply that observations from different periods of the winter with respect to the climatology are necessarily expected to have the same spatial pattern. Rather, this formulation allows us to observe where and when there are differences in the relative spatial distribution of snow cover.

We then compare both the absolute value of the resulting SNV map between pre- and post-fire periods to identify regions where the spatial pattern of snow cover has changed. This indicates regions where, given the same amount of regional snowfall, more or less snow cover is expected to occur. We also compare the correlation of the SNV between pairs of months in pre- and post-fire landscapes. First, we compute R^2 scores between paired pre-fire scenes to establish a baseline distribution of pattern repeatability. Then, we compute the same between each possible pair of pre- and post-fire scenes. The time frame of water years

2018-2024 was selected to consider the same number of data points in pre-fire and post-fire years.

5.3.8 Snow monitoring representativeness

The snow measurements listed in Table 5.1 comprise the basis for water management in the South Fork American River basin via their use in physical hydrological models and other estimates at the basin scale. The ability of such measurements to accurately represent snowpack within the basin is therefore directly related to water supply prediction quality. While the baseline representativeness is generally related to physiographic characteristics (Molotch & Bales, 2006), non-represented physiographic classes (such as canopy cover) can nonetheless be represented given sufficient empirical data. We first computed the canopy cover and RdNBR over the burned sites, the snow courses, and all remaining area within the study region. The distributions of these conditions demonstrates how the location of snow courses relates to the regions they represent in the context of the Caldor Fire. We use the Caples Lake sensor due to its long data record and the co-location of depth and mass sensors. To estimate the ability of the Caples Lake snow depth sensor to represent snow depths within the burned area on a daily basis, we identified each event of snow depth gain or loss within the seasons, e.g., days (or consecutive days) with snowfall, compaction, or melt. Snow depth gain is assumed to be from new snowfall (i.e., wind and gravity redistribution are not accounted for), while snow depth loss could be from compaction, sublimation, melt, or a combination of those processes. For each gain or loss event, we compared the normalized change in the Caples Lake sensor to each within-fire site. The normalized change is the percent of peak snow depth at that point for the year to account for the different snowfall expected at different elevations and aspects.

5.4 Results

5.4.1 In situ, distributed snow depth time series

Time series of snow depths across the burned South Fork American River basin from photography in this study show a series of storms and ablation periods from deployment in November 2022 to melt in June 2023 (Figure 5.3, solid lines). These time series show a range in snow depth across elevations (line color), but elevation does not fully explain snow depth variation between sites. These higher-elevation depth-pole observations also show snow depths that could not be estimated from the depth poles due to excessive depth. The Caples Lake depth sensor (black dashed line) and six monthly snow surveys (dots) measure similar depths early in the season but diverge starting in February and remain higher through the end of the season. The camera time series are correlated to the Caples Lake sensor ($R^2 = 0.65$) throughout the year, although there is meaningful variation throughout the season. The cameras see different timing of accumulation in December ($R^2 = 0.50$), but

similar responses to events in January ($R^2 = 0.93$) and February ($R^2 = 0.90$). The time series diverge in March (R^2 = -0.14), likely driven by one midwinter loss event from March 6-21, 2023 that does not appear in either the Caples Lake time series or the monthly snow course measurements but does affect the camera time series. During that time period, the Caples Lake sensor recorded a 5.1 cm snow depth gain while the four active cameras recorded an average 30.2 cm snow depth loss. Melt in April is correlated ($R^2 = 0.94$); there is insufficient snow to meaningfully interpret a correlation at the camera locations after April.

Depth time series from camera plots are not necessarily representative of the basin, but rather represent a narrow range of elevations and aspects while covering a range of burn severity. Nevertheless, the range from camera plots exceeds the range in snow depth amounts of CCSS measurements during accumulation. During Spring (i.e., after ∼April 2024), snow survey measurement values are both greater and with a broader variability than the depth pole time series. However, the range of camera records during this time is limited by the height of camera installation – all camera sites with depths over ∼2.3m could not be measured because the camera and/or pole would be covered by snow. In this time series, depth loss does not necessarily equate to snow mass loss as compaction without additional snowfall, especially accelerated by ripening (snowpack warming up until the point of melting), can cause depth loss without sublimation or melt.

End-of-season melt at each camera site is estimated in three ways: from photography, via the pendant logger temperature at the ground, and pendant logger light intensity records. All three methods for estimating snow disappearance date from the field measurements produced dates within one day. Hereafter we show results from the pendant logger temperature timeseries because it is the most complete record among sites with a pendant logger sensor as one site's luminosity sensor malfunctioned during the winter. The elevation-normalized melt-date discrepancy in Figure 5.4 represents the amount of early (below 0 on the y axis) or late (above 0 on the y axis) melt compared to the MODIS pixel that cannot be directly explained by elevation. The canopy survey number represents the amount of overhead cover from a manual survey that accounts for overhead tree presence and quality (i.e., alive, red, or dead), with higher numbers indicating more cover. Across the 17 plots with clear pendant logger time series, those with more canopy cover are more likely to melt later than the overall MODIS pixel while those with less canopy cover are more likely to melt earlier. Plots with higher canopy survey scores also had lower fractions of dead trees in the canopy (Figure 5.4, colors); some canopy cover increase came from increased presence of live canopy, not just a higher number of overhead survey points containing vegetation.

5.4.2 Aspect-dependent post-fire snow impacts

Snow depth maps from four ASO acquisitions during 2023 are used to construct elevation-aspect maps of snowpack across burn severity categories within the study region. Across acquisition dates and burn severity categories, northeast aspects at elevations between 1900 m and 2600 m experienced higher snow depth in the burned area (Figure 5.5). High severity burns had a greater volume increase in the areas for which snow depth difference is positive

and a greater aspect range over which this difference is observed. The local snowpack benefit is greatest at the 31 January acquisition (Figure 5.5a-c) and declined throughout the spring; at the June acquisition, no benefit remained except in scattered high-elevation portion of low-severity burn.

On 31 January, low severity burns showed a positive median snow depth difference of 0.043 m (q1=0.017, q3=0.095 m), with 28.84% of the aspect-elevation space positive. Moderate severity burns had a similar pattern, with a positive median of 0.044 m (q1=0.021, q3=0.090 m), covering 29.43% of the elevation-aspect space. High severity burns had positive mean of 0.075 m (q1=0.039, q3=0.115) covering 37.34% of the elevation-aspect space. Southern aspects, in contrast, experienced lower snow depth in burned regions at all dates and burn severity categories. The magnitude of snow depth loss and its aspect range expanded in time; by June almost all elevations, aspects, and burn severity categories had lower snow depth within the burn than outside of it (Figure 5.5j-l).

Median negative differences in high severity burns reached a minimum of -0.099 m (q1=-0.1824, q3=-0.0379) in January, growing to -0.24 m (q1=-0.4166 q3= -0.0716) by late April, while positive measurements peaked at the 13 April observation at 0.096 m (q1=0.008, q3=0.17) and diminished to 0.001 m by June. The difference between burned and unburned areas in the same elevation-aspect space was statistically significant (p¡0.05) only for the high severity category and only for the 13 April (p=0.0189), 28 April (p=0.0001), and 2 June (p=0.008) acquisitions. This temporal progression of increasingly statistically significant negative impacts in high severity burn areas suggests that fire-induced changes to surface energy balance and snow retention become more influential as the melt season progresses.

5.4.3 Low-canopy cover patch size

Large patches of low canopy cover (> 400 hectares) have lower snow depth than in small patches (< 10 hectares) at elevations below 2400 m at all aspects throughout the season, from accumulation (Figure 5.6a,c,e) to ablation (Figure 5.6g). At higher elevations, large patches have higher snow depth than small patches. The elevation at which the advantageous patch size transitions from small to large patches is constant at all dates observed at the 150-m elevation bin resolution. The standard deviation of this difference (Figure 5.6b,d,f,h) is higher where the effect size is highest. In this representation, the standard deviation represents the spatial variance within a given elevation-aspect bin. By the June acquisition (Figure 5.6g), the difference between small patches and large patches is small at most elevations, but is maintained at high elevations.

It is important to note that these patch calculations include patches of low canopy cover caused by the fire, patches that pre-dated the fire, and patches where fire removed canopy adjacent to a pre-existing opening. Canopy cover, or lack thereof, in a burned area can be edaphically driven or from a prior disturbance in addition to the recent fire; the burn severity indices used here respond to vegetation quantity change through a spectral index over a defined period and therefore capture some of the structural change due to fire. However, these indices are also designed to track vegetation quality change (i.e., mortality), which is

an important outcome of fire but does not necessarily result in canopy cover change. This analysis specifically shows how the size of low-canopy cover patches relates to snow depth distribution but does not capture the impacts of combustion itself (e.g., changes in snow or tree bole albedo).

5.4.4 Snow course representativeness

Snow courses, the sites measured in this study, and the entire study region experienced different impacts of the Caldor Fire. The entire study region saw a median canopy cover drop from 45% in 2020 to 25% in 2022 (Figure 5.7a, purple bars), while the interquartile range also grew from 20% to 45%. Over the same time period, the snow courses canopy cover dropped from 10% to 0% and the interquartile range fell by 10% (Figure 5.7a, red bars). The values for canopy cover are reported in units of 10 percent and cannot go below 0, so the slightly smaller interquartile range for snow survey sites post-fire is partially due to a physical boundary in the possible values. The sites established in this study had a median pre-fire canopy cover of 55% and median post-fire canopy cover of 0% (Figure 5.7a, green bars). Most of this change is caused by the fire as minimal commercial harvesting took place during this time frame and only minimal post-fire salvage logging occurred in the year immediately following the fire. The burn severity distribution of each category in Figure 5.7b shows that the snow survey sites cover the lower range of burn severities seen within the study region while the camera sites cover most of the high range of burn severities. However, the median of the distributed sites is in high-severity burn while the median snow survey burned at low severity.

This difference in burn severity and post-fire canopy cover have the potential to result in different post-fire snow measurements. Figure 5.8 shows the relationship between snow depth change (post-pre) at the Caples Lake sensor, which is in a high-elevation, open area near the 2019 Caples Fire burned area. For each gain or loss event during the winter season, the amount of snow depth change at the Caples Lake sensor (x-axis) is compared to the depth change over the same time period at all of the distributed camera sites (y-axis). The Caples Lake sensor gained a lower percentage of its annual snow during snow gain events and lost less snow during loss events than the distributed depth poles. The average distributed sensor responded to an event with triple the percent of its annual maximum snow depth compared to the Caples Lake sensor.

The Caples Lake automated snow monitoring station provides a local, temporally complete snow depth record and can therefore be compared to depth pole measurements during each snowfall or depth loss event. For each depth gain or loss event throughout the season, the Caples Lake sensor and the distributed depth poles agreed on the direction of change for more than 90% of events, but differed on magnitude. The snow courses, on the other hand, generally tracked the Caples Lake sensor throughout the winter (Figure 5.3), although the Tamarack and Philipps courses, which are at the lowest elevations, melt more quickly, as expected.

5.4.5 Snow cover spatial patterns

In addition to measuring the response of different snow measurement sites in time to different events, we can observe the spatial patterns in snow cover distribution. Figure 5.9 shows the difference in the SNV of snow cover from MOD10A1 monthly composites after fire (2022-2024) to before fire (2018-2020) in the region of the Caldor Fire. The SNV calculation normalizes for total snow cover area so the resulting comparisons show how snow cover changes relative to snow cover elsewhere in the region. Nearby regions generally experience the same storm events, so the resulting spatial distributions reflect different accumulation from mechanisms such as interception, but not different storms. These distributions also reflect different ablation, but because individual pixels are compared to themselves in the difference map, ablation variance is theoretically independent of location-specific drivers such as aspect and slope. The remaining differences are generally negative inside and directly south of the burned area and mixed-to-positive elsewhere. Notably, the strongest statistically significant pixel changes as calculated with a two-tailed Student's t-test with a significance criterion of $p < 0.05$ (indicated by stippling in the map) occur inside the burned area area. Additional positive significant changes occur in small (< 10 hectares) patches on the eastern slope of the Sierra Nevada, where snowfall is generally low due to rain shadow effects. The negative changes with the burned area indicate that for each monthly composite, the snow covered area within the burned area is significantly lower than expected from pre-fire maps, controlling for the total amount of snow cover in the region.

5.5 Discussion

5.5.1 Within-season snow depth variability

The winter season measured in this field campaign (2022-2023) was one of the deepest snowpacks on record for this location, both in terms of total accumulation and peak snowpack (depth and SWE). This snow came from a series of large storms between November 2022 and April 2023. During the winter, snow depth loss in the observational record is primarily due to compaction and some mid-season melt. In the spring, the majority of snow depth loss is from melt.

The time series of snow depths at the distributed sites in Figure 5.3 show a range of responses to accumulation and loss events throughout the season. Much of this variance in response is not explained by elevation alone. For example, from February to late-April, the site with the lowest snow depth recorded was at a higher elevation than many other active camera sites. The highest elevation sites (Figure 5.3 dark blue lines) are excluded from the record because their snow depths are above the maximum depth possible to record. One loss event in early March, 2023 occurred just after a CCSS survey date and was observed in all active time-lapse cameras, but not at the Caples Lake snow depth sensor. Events such as these are more likely to occur during midwinter dry spells and affect burned areas more

than unburned areas (Hatchett et al., 2023) and have the potential to create short, flashy streamflow peaks with little warning.

Over the course of the winter, the distributed time-lapse camera records are well-correlated to the Caples Lake snow depth sensor (Figure 5.8). The extreme high snow depths in the year of this study limit the amount of distributed snow depth values retrievable from the field campaign. However, some discrete events, such as the early-March melt, are not seen in the Caples Lake sensor record. On average, the time lapse cameras responded more dramatically to a given snow depth gain or loss event than the Caples Lake sensor, when expressed as a proportion of the total winter snow depth. The slope of the best-fit line between the relative Caples Lake snow depth change and the camera snow depth change is 3.01 and fits well for both loss and gain events. However, there is scatter between different cameras.

5.5.2 Aspect and burn severity drive post-fire depth differences

Figure 5.5 shows that burned areas on the northern aspects have higher snow depths than unburned areas or other regions in the burned area with lower severity. In low severity patches, the negative and positive differences are small. However, the location of negative and positive signals in elevation-aspect is similar to the locations of the same signals in the moderate- and high-severity cases, with positive change (i.e., more snow in the burn than outside of it) between 2000 and 2600 m a.s.l. and on northeast-aspect slopes. In the moderate- and high-severity burned areas, those regions maintained deeper snow depths than in the unburned region through the third ASO acquisition on April 28; by the June 2 flight, all elevations and aspects surveyed had more snow in the unburned area.

This burn severity-based comparison is the product of black carbon-driven albedo decline and of canopy cover loss. Snow albedo profiles from the Caldor Fire scar (Hatchett et al., 2023) show a severity-dependent albedo depression: snow in higher severity areas had a lower albedo at all wavelengths sampled with stronger impacts in the 0.4-0.8μm range than at longer wavelengths. From this, other observations of post-fire snow albedo, and visual observation during the field campaign, we expect the higher severity patches to have lower snowpack albedo due to black carbon deposition (via dropping of dead, charred branches and sloughing of charred bark); there is not currently evidence to suggest that the albedo differences change with aspect or elevation.

Aspect does, however, affect incoming shortwave radiation and therefore the importance of albedo in radiative forcing. Elevation also impacts baseline temperature and therefore whether or not the radiative forcing from black carbon is enough to induce melt. Later in the season (i.e., Figure 5.5 j-l) the solar zenith angle is more overhead and the average air temperature is warmer so albedo decrease should be relatively more important than earlier in the season. On south-facing slopes, aspect does not protect the slope from direct radiation, so short-wavelength albedo and the lack of shading from canopy are more important even earlier in the season. Reis et al. (2024) found aspect-dependent snow peak timing and melt rate impacts from wildfire, with south-facing burned slopes experiencing significantly earlier peak SWE and faster melt. Our field sites are within a small aspect range so we do not

see this impact in an analysis of the full time series ensemble. However, the four ASO lidar snow depth acquisitions provide a more complete view of snowpack distribution across physiographic and burn severity categories.

The severity-dependent magnitude of differences is likely due to both the lower black carbon deposition in areas with less-severe burn as well as the lower likelihood of open canopy in the low-severity regions. This severity-based differentiation alone, however, does not perfectly capture the impacts of canopy cover as low canopy cover can result from a several mechanisms, including those that predate the fire (e.g., unfavorable soil conditions, steep slopes, logging) or those that follow (e.g., salvage logging, windfall).

5.5.3 Canopy gaps protect snow depth at different sizes

Low canopy cover – be it from fire or another source – acts differently on snowpack at different spatial scales (Stevens, 2017). Figure 5.6 isolates the effects of low-canopy cover patch size. For larger patch sizes, the snow inside the patch experiences loss of shade and increased surface wind speed, especially farther from the edge of the low-cover patch (Varhola et al., 2010). In smaller patches, snow is more likely to experience consistent shading, but also potentially warmed by longwave radiation from nearby trees. There also may be some effects of interception and canopy drip as more of the patch is close to vegetation than in a larger patch (Stevens, 2017). We show that at lower snowy elevations, smaller low canopy cover patches have deeper snowpacks than larger patches at the same elevation and aspect. This effect is more pronounced in the April and June acquisitions than in the January acquisition, indicating that some of this difference comes from ablation, not just accumulation effects. This analysis shows highly local variation in the impacts of forest cover on snow distribution. Lundquist et al. (2013) use a global analysis to show that colder sites benefit from open forest while warmer sites see decreased in snow retention; interpreting the elevation gradient seen here as a temperature gradient implies a theoretical alignment here, with higher-elevation (colder) areas benefiting from larger canopy gaps.

In this work, we only look at patches that exist after the fire (i.e., from the 2022 LFCC product) and are inside of the fire perimeter. The time scale of canopy cover change impacts, however, is potentially longer than the black carbon radiative forcing impacts, as albedo recovery occurs on the scale of 5-10 years (Gleason et al., 2013) while canopy regrowth can take decades depending on tree species, climate, and management (Scholl & Taylor, 2006).

5.5.4 Snow cover declines after fire

Satellite observations of snow cover provide a broader view of post-fire snow patterns by permitting long-term pre- and post-fire analysis. In Figure 5.9, we show that the area within the Caldor Fire burned area saw less snow cover than would be expected given the total regional snow cover in the two years after the fire. Most of the statistically significant change in the region occurred within the burned area and of that, every pixel showed a negative change in standardized snow cover area. Other statistically significant change in

the region is either in isolated clusters of pixels or in regions on the leeward side of the Sierra Nevada ridge where the baseline snow cover is very low. No other cluster of MOD10A1 pixels in the historically high-snow region saw meaningful standardized snow cover change.

The use of standardized snow cover here specifically identifies when an area is changing more than its surroundings and accounts for the difference in total snowfall between years. Similar analysis from Hatchett et al. (2023) found that absolute snow cover days and snow cover fraction in the Caldor Fire burned area dropped when compared to the 2001-2022 mean of the MODSCAG record (Painter et al., 2009). The snow cover analysis here equally covers accumulation and ablation season but is at a much coarser resolution than MODSCAG or ASO. We therefore expect to miss some of the finer-scale or partial-season patterns, especially the aspect-dependent snow benefit shown in Figure 5.5. This full-season spatial pattern analysis may under-represent the severity of ablation impacts, such as advancing melt-out date or faster melt speed. The melt-out date discrepancy between MOD10A1 and the pendant loggers in Figure 5.4 reflects that even removing the elevation signal from within a remote sensing pixel, local vegetation condition variance can correspond to up to 15 days of snow disappearance date advancement or deferment.

5.5.5 Snow measurement representativeness

Long-term snow measurements in the Caldor Fire burned area and surrounding regions have occurred for over 100 years. The majority of these measurements are manual snow depth and water equivalent surveys carried out by CCSS cooperators at established sites. The CCSS sites are not expected to directly match the distribution of characteristics across the basin, rather they are used to track interannual variability of conditions in the basin; this is taken into account when measurements are used for operations and modeling. These sites must be easily measurable with the snow surveys method and as a result, tend to be in open, flat regions that are relatively accessible. CCSS sites also do not match the surrounding forest's canopy cover before or after the fire (Figure 5.7 a) and were not burned at the same severity as the rest of the basin (Figure 5.7b). In this context, siting requirements likely play a role in the lower burn severity at CCSS sites than across the rest of the basin. Post-fire use of CCSS values may represent basin-wide conditions differently than they would have without the impacts of fire.

Interestingly, one effect of the Caldor Fire was to bring the basin-wide canopy cover closer to the distribution directly sampled by CCSS sites. However, the albedo effects of the fire are likely not well sampled by the CCSS sites as a whole as only one CCSS site is in a high-severity region.

5.6 Conclusion

The expanding range of wildland fire into regions with significant snow water resources is likely to increase under future climate, fuels, and management scenarios. The impacts of this

expansion are many and range from the sociological to the ecological to the hydrological. In this work, we use a large, severe, montane fire to gain insight into the effects of wildland fire on snow accumulation and duration. By combining a large number of in situ sites distributed across burn severity categories together with high-resolution remote sensing products, we show that burn severity, more than burned vs. unburned categorization, impacts the snowpack response to fire. Throughout the winter, high severity regions generally held less snow than unburned regions at all elevations and aspects. This difference is exacerbated at high elevations. Low severity fire, in contrast, held more snow at high elevations and slightly less snow at low elevations. During the accumulation season, differences between burn severity categories are small. As melt proceeds, the differences are exacerbated as high-severity fire regions melt much more quickly than unburned or low-severity regions. Interestingly, our post-fire snowpack observations include an extreme wet winter (Marshall et al., 2024), which may dampen the importance of interception as canopy intercepts a higher fraction of snow in light snowfall. This heavy snowfall accumulation also resulted in poor data quality from some snow pillow stations in the Sierra Nevada region, further highlighting the importance of snow surveys for water management in extreme years.

In general, mechanisms for forests to become protective of snow accumulation and duration include transitions to heterogeneous, moderately dense forests with small, distributed canopy gaps as occurred when frequent lightning fire is restored in a watershed in the central Sierra Nevada (Boisramé et al., 2017; Collins & Stephens, 2010). The so-called triple-win condition, in which fire, water, and biodiversity interactively benefit each other (Stephens et al., 2021), is not a guaranteed outcome of fire. Rather, the odds of a broadly beneficial outcome are increased by policy and management decisions. Severity-aware analysis of effects of fire on snow show that the water benefits of low severity fire persist even in large fires. In this case, the extended melt in low-severity patches likely buffered the early melt signal from high-severity patches. The post-fire impacts, however, are strongly dependent on local burn severity, topography, and patch size of open canopy. Forest treatments before and after fire can contribute to canopy cover patterns that may not be accompanied with other characteristics of burned regions such as changing soil infiltration, low shrub cover, and black carbon deposition (Stephens et al., 2024).

5.7 Data and code availability

The automated logger data collected in this study are archived at 10.5281/zenodo.10714264. Metadata and site conditions for the distributed sites are in the Supplementary Materials. The ASO data are publicly available at https://data.airbornesnowobservatories.com/basin/american. MODIS data are available from the National Snow and Ice Data Center https://nsidc.org/data/mod10a1/versions/61. Canopy cover data are from the LANDFIRE program https://landfire.gov/data. The Caldor Fire burn severity data can be accessed via https://www.mtbs.gov/direct-download. The FACTS dataset is hosted at https://data.fs.usda.gov/geodata/edw/datasets.php. Code used in this project is available at https://github.

com/mariannecowherd/caldor-snow.

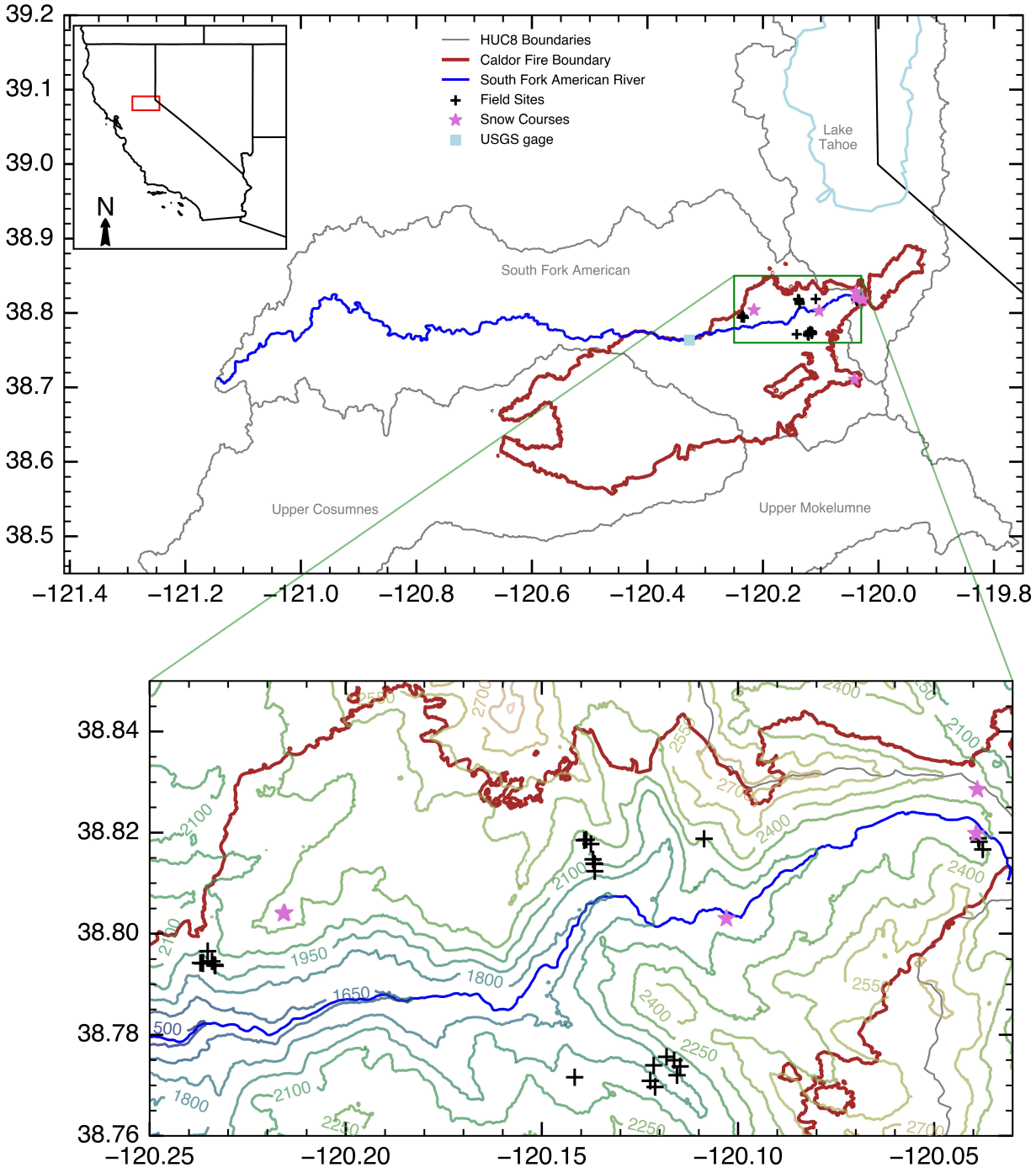

Figure 5.1: Location of the study site in the context of the Western United States (a, inset) and related natural features, including the Upper Mokelumne, Upper Cosumnes, South Fork American, and Lake Tahoe watersheds (gray), the South Fork American River (dark blue), Lake Tahoe (light blue), and Caldor Fire perimeter (red). Established snow courses and pillows (pink stars) and field plot locations in this study (black plus signs) are highlighted against topography (b). Some courses and pillows are close enough together that the stars overlap.

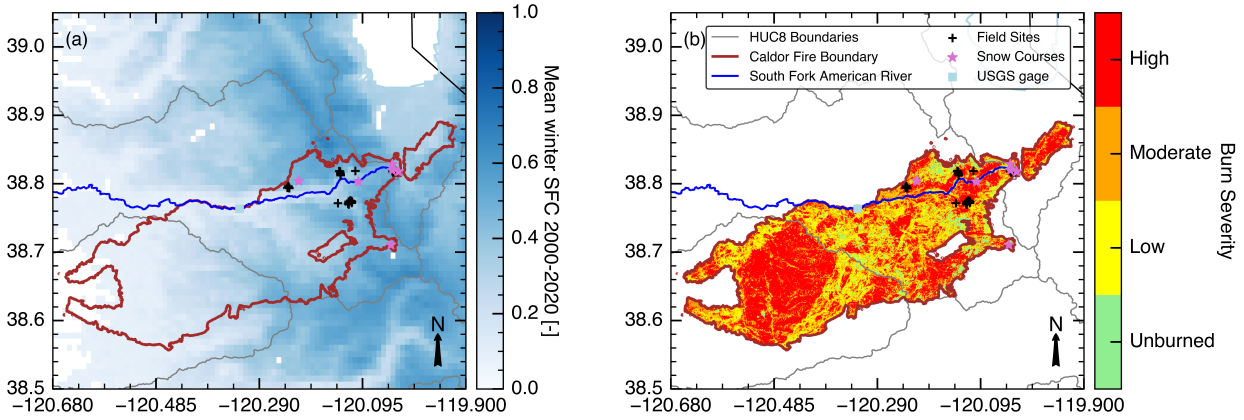

Figure 5.2: Mean winter fractional snow covered area from 2000-2020 from MODIS and Caldor Fire burn severity from MTBS.

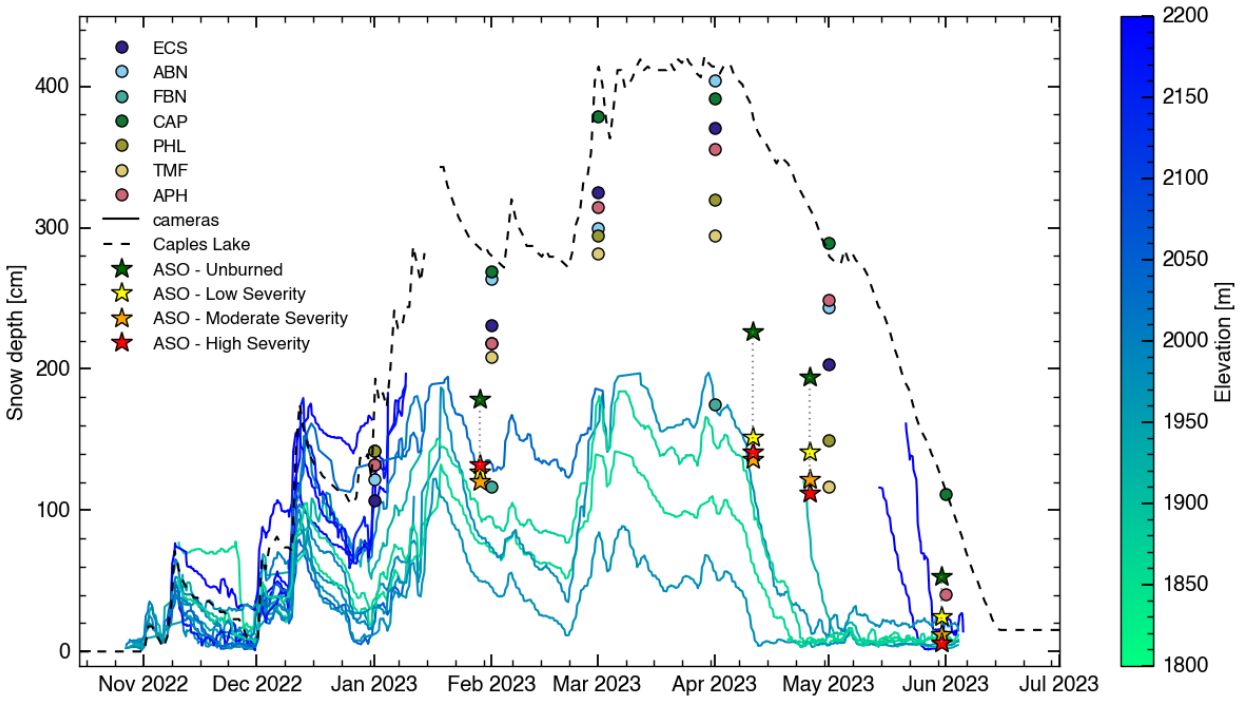

Figure 5.3: Quality-controlled snow depth time series from camera plots (line in the shades of blue), with colors indicating elevation. Local monthly snow course (points) and automated snow depth sensors (black dashed line) from CCSS and cooperators are overlain, showing the data density acquired from each source. Stars indicate mean snow depths in each burn severity category (indicated by color) across the portion of the South Fork American River burned in the Caldor Fire, from 50-m resolution ASO acquisitions of snow depth.

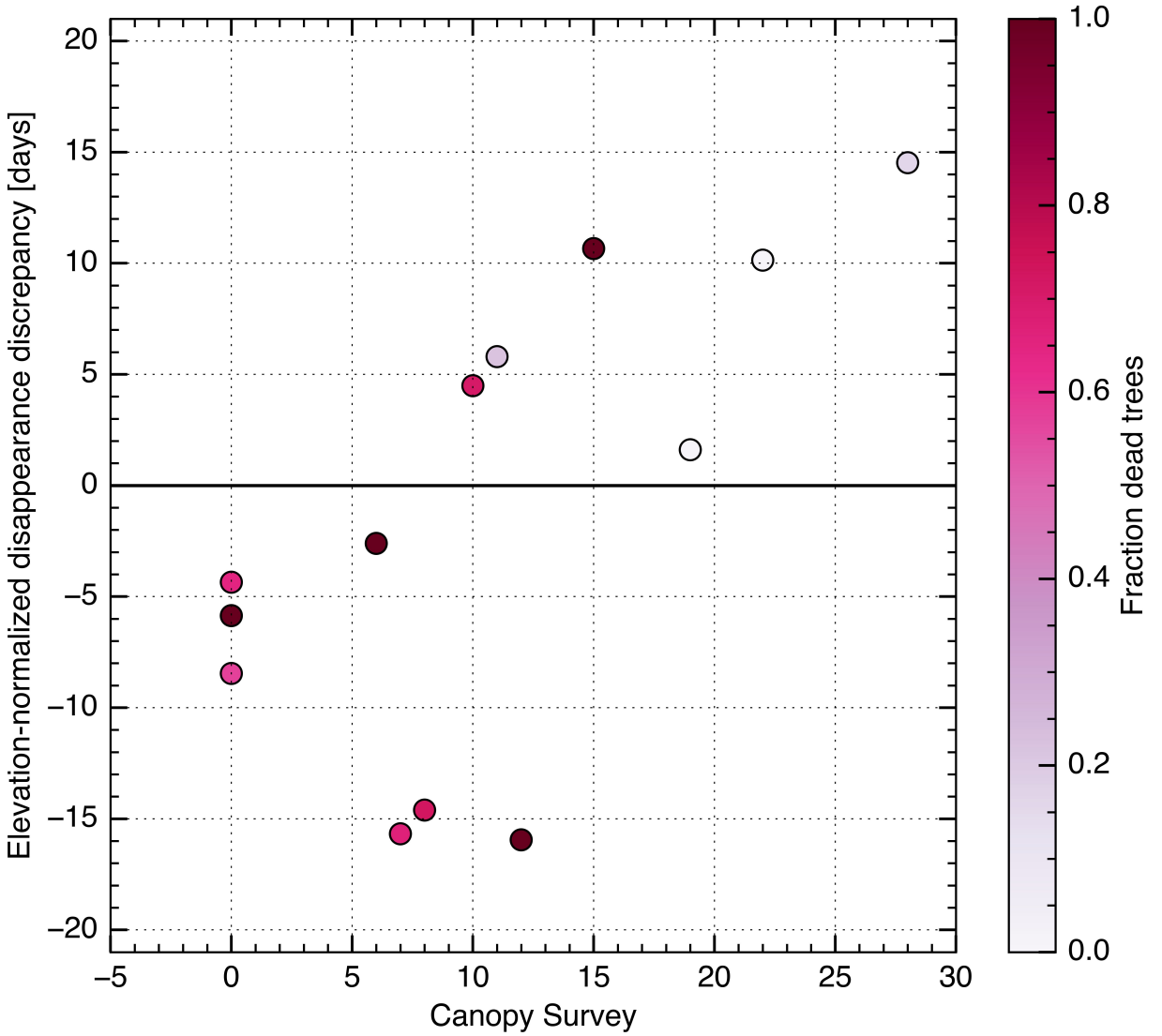

Figure 5.4: Disappearance date discrepancy (pendant logger – MODIS) with the linear elevation trend removed plotted against canopy survey score. Positive disappearance date discrepancy indicates that the monitored site retained snow longer than other locations within the same MODIS pixel. Canopy survey score is from manual overhead census of vegetation presence and health, with higher scores indicating more widespread and healthier coverage. The contribution of tree count vs. tree health to a high canopy survey score is indicated by point color: darker points have a higher fraction of dead trees and therefore greater contribution of tree count to the canopy survey score.

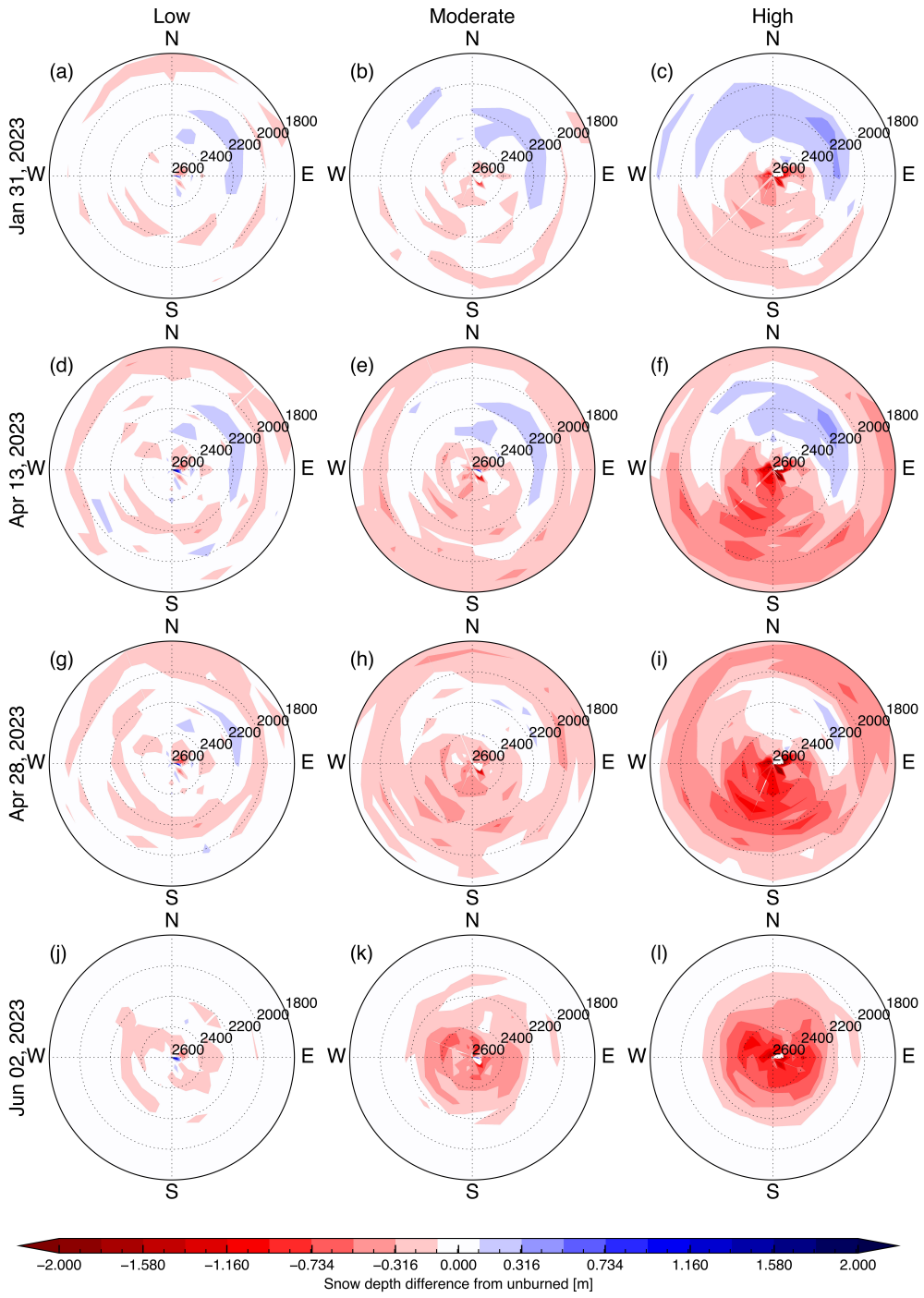

Figure 5.5: Elevation-aspect maps of ASO snow depth difference between burned and unburned portions of the American River watershed; elevation (m) is indicated by radius and aspect (degree) by angle. For each date (row) and burn severity category (column), values shown are the difference between burned pixels and unburned pixels within the same elevation and aspect bin. Each panel shows the difference between snow depth in each of three burn severity categories – low, moderate, and high – compared to unburned (control) locations of equivalent aspect (angle) and elevation (radius). Blue (red) colors indicate topographic regions where burned area snow depth is higher (lower) than in unburned areas of the same elevation and aspect.

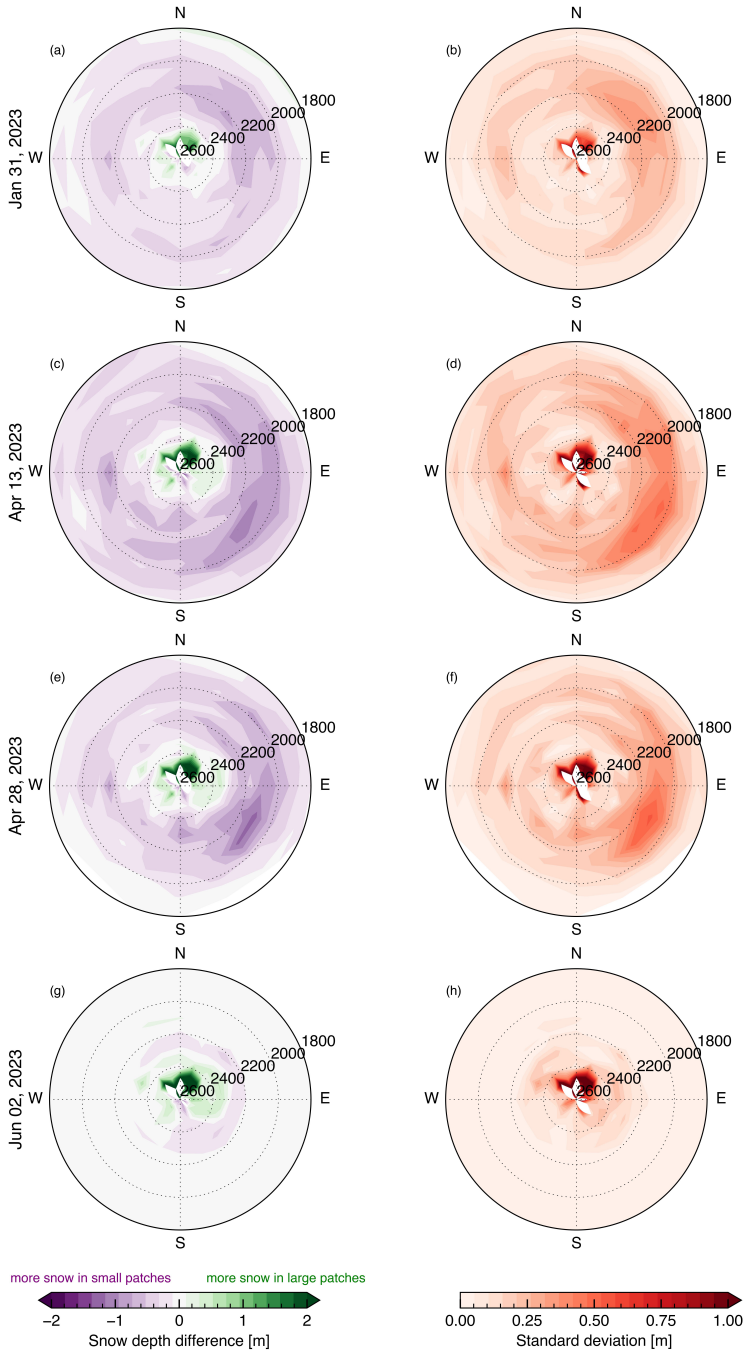

Figure 5.6: Snow depth difference between open-canopy patches with contiguous low canopy (<10%) cover in small (< 10 hectares) and large (> 400 hectares) patches. Burned and unburned areas are included, so the low canopy cover results from fire- and non-fire processes. Standard deviation of the difference for each acquisition is shown for the same elevation-aspect bins in the right column.

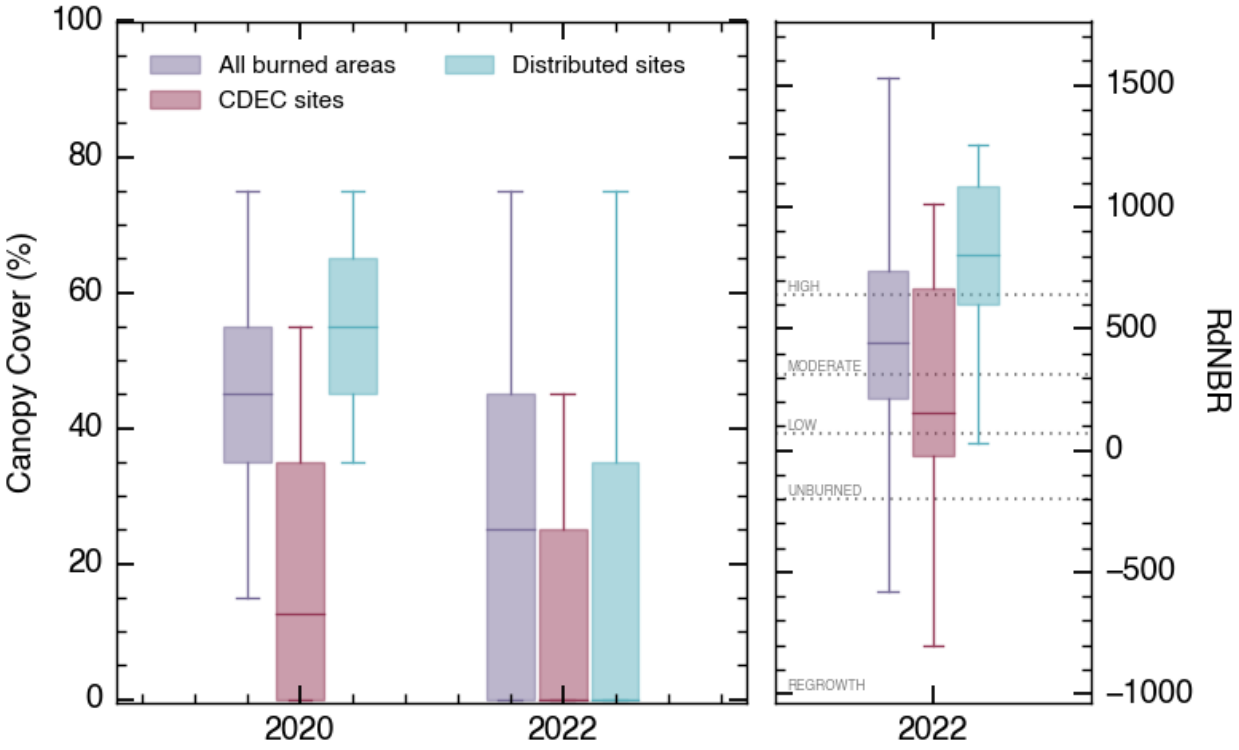

Figure 5.7: Full-region (purple), snow survey site (red), and distributed site (green) LANDFIRE canopy cover in 2020 and 2022 (a). (b) shows burn severity distribution for the same categories from MTBS.

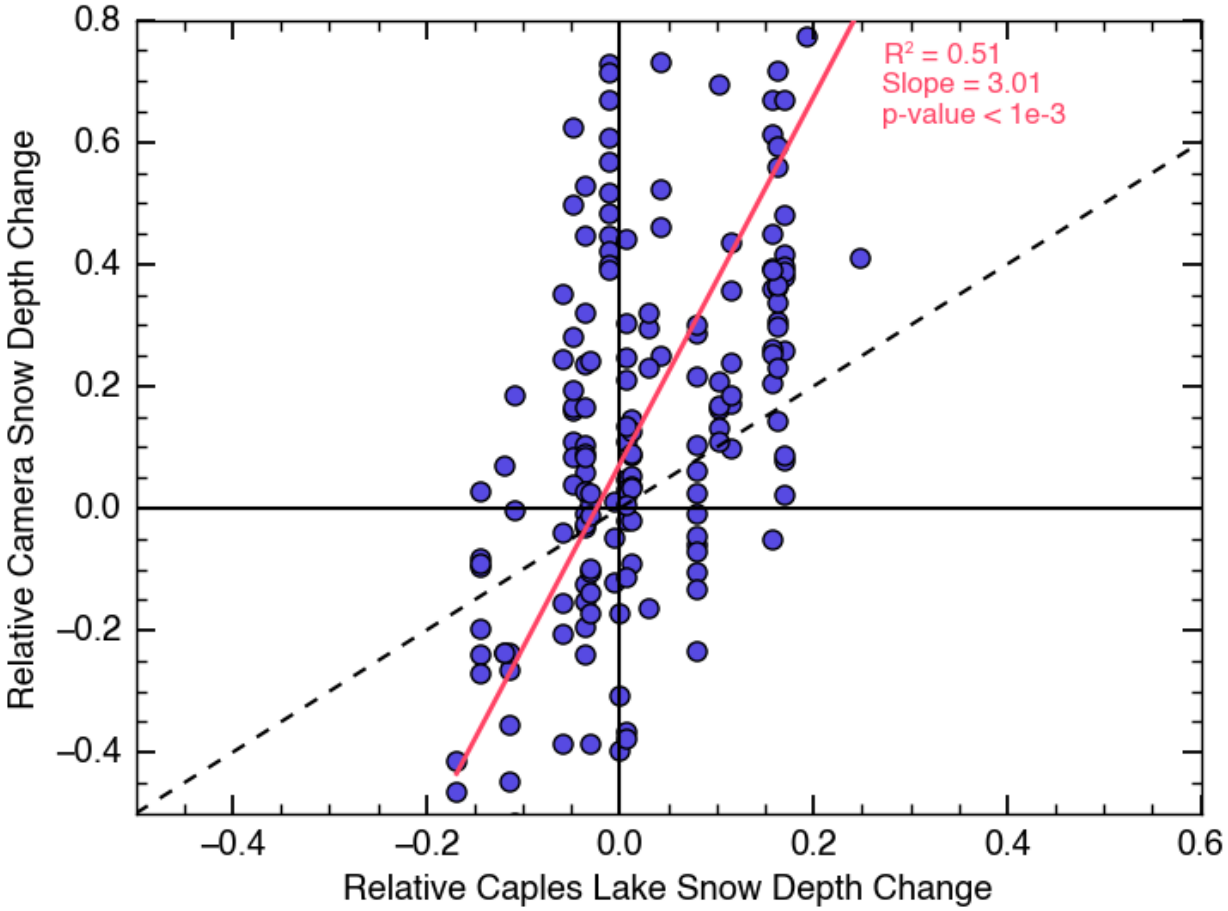

Figure 5.8: Normalized change at the Caples Lake snow depth sensor (x-axis) and all in-fire depth poles (y-axis), identified by event of continuous monotonic change during the 2022-23 winter. One-to-one line is shown in dashed black line and best-fit line for all data points is in red.

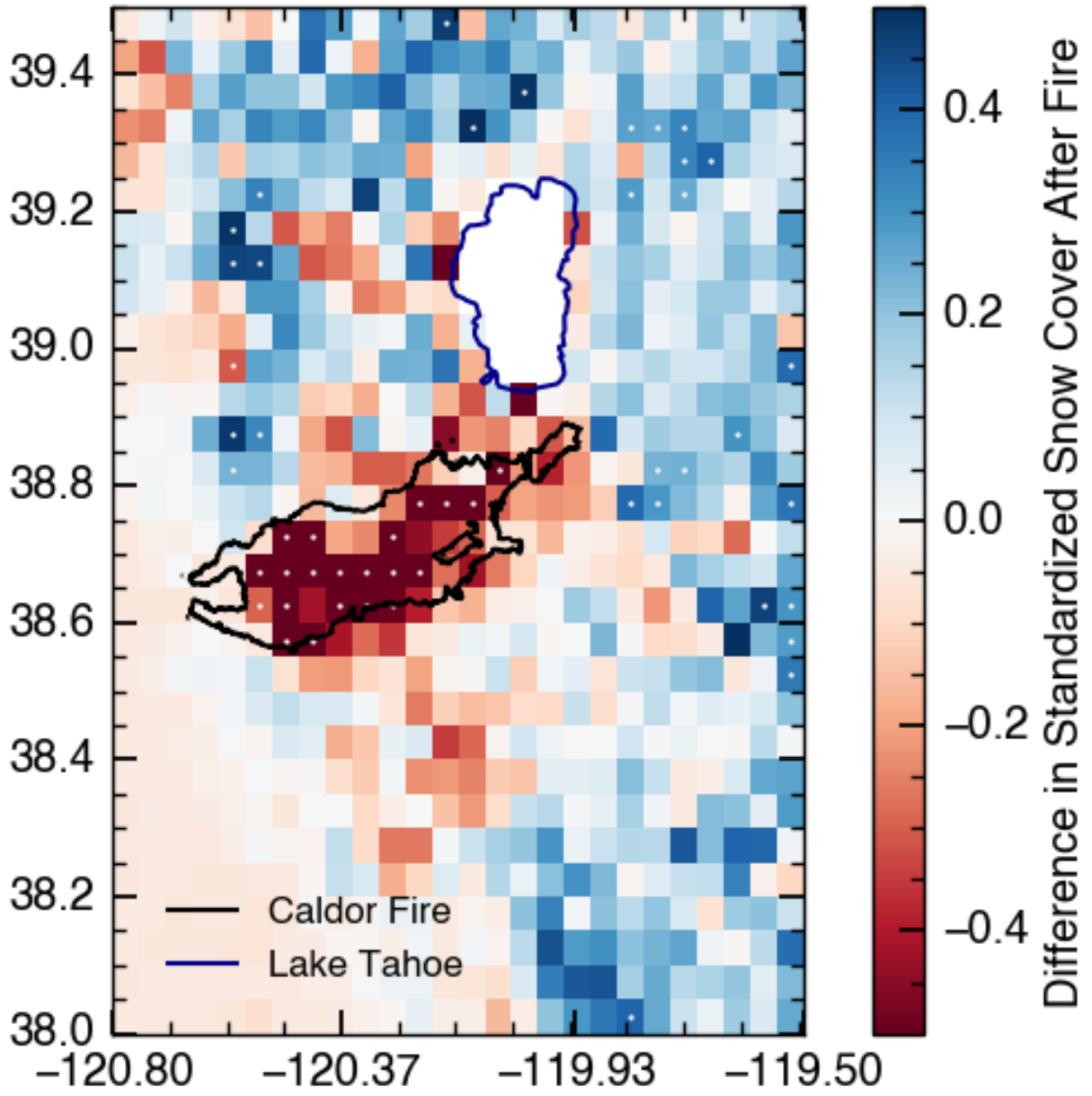

Figure 5.9: Difference in standardized normal variate MODIS fractional snow-covered area between pre-fire (2018-2020) and post-fire (2022-2024) water years using monthly composites from MOD10A1 from November through May; positive values (blue) indicates a higher snow cover compared to surrounding areas. Stippling indicates statistically significant difference.

Chapter 6

Conclusion

"In making war with nature, there was risk of loss in winning." –John McPhee

6.1 Goals of the dissertation

Snow is a global sentinel of climate change and a critical component of the climate and hydrologic systems. This dissertation addresses examples of change from climate and wildfire in the context of drought and water management. The goal of this dissertation is to study the effect of long- and short-term change in the environmental surroundings of snowy regions on snowpack quantities and on snowpack measurements. In Chapters 2 and 3, I and collaborators analyze projections of long-term, gradual change on snow quantities and drought statistics. In Chapter 4, I, with contributions from chapter co-authors, identify how snow the information acquired from snow measurements changes in multi-decade climate projections. Finally, in Chapter 5, I and co-authors use the Caldor Fire as an example of discrete, rapid change to vegetation to study the response of snowpack measurements to disturbance on short (1-2 year) time scales.

6.2 Summaries

Chapter 2 uses a current state-of-the-art climate model ensemble to quantify the statistical drift in snow as a water resource around the world. Most of this drift is attributable to temperature increase within a single year, i.e., most anomalously low snow years occur when there is also an anomalously high temperature at the same location. The same shift does not happen to dry years. In fact slightly fewer years are dry in the future compared to the past. This means that there will be more years with sufficient precipitation, but insufficient natural storage of that precipitation, leading to challenging water management years that do not show up in precipitation-based drought indices. This work underscores the need to track natural water storage in addition to gross supply when issuing short-term drought warnings.

In Chapter 2, the coarse model resolution means that any results are best taken as regional conditions, but not representative of water management in a particular basin. The dynamical downscaling in Chapter 3 allowed for basin-specific trend identification, including differentiation of the drivers of snow droughts over topographic features such as divides. Here, I found that windward slopes, which are wetter in atmospheric river-driven regions such as the western US, are more sensitive to temperature as a driver of snow drought. On the drier leeward slopes, water supply is more important and therefore some short-term climate change corresponds to increases in snow water equivalent. In the latter half of the 21st century, the benefit of added water vapor is insufficient to counter the ice-melting effects of water, and temperature becomes a stronger driver in all locations. Water resource managers should consider the role of orography in basin-specific projections of water resources. Continued investment in higher resolution climate model-based products should be accompanied by further work on identifying circulation drivers of droughts, especially in regions reliant on infrequent large storms. Shifting circulation patterns from climate change have the potential to move storm track distributions, which could present a water resources tipping point for systems like California's atmospheric river-dependent regions.

In Chapter 4, I analyzed the behavior of snow monitoring stations. These stations, of which there are over 1000 in the Western US, form the backbone of water resources management and drought warning. However, an emerging mismatch between the locations of those networks and the location of on-the-ground snowpack means that ground measurements will become less valuable for understanding distributed snowpack amounts and predicting droughts. I quantified the climate sensitivity of established snowpack measurement networks in the US. This work projects that our ability to estimate unmeasured water reserves will decline by up to 40% by 2100 because snowpack distributions in warmer years are meaningfully different from the past. However, using convolutional neural networks to learn the two-dimensional structure of snowpack distributions or introduced new remote sensing-based maps, climate-sensitive prediction quality improved by over 30% and maintained skill in warmer climates. This showed that machine learning is capable of pushing legacy observation networks to adapt to new climate regimes and motivates future work on interpreting multi-resolution neural networks. Applications to water resource management should focus on extreme low snowpack years as these are the most likely to be poorly predicted by traditional approaches. Explainability-oriented machine learning research to identify when neural networks are the most needed and which locations within basins contain the most valuable predictive information. Extensions of this work could serve to motivate the placement of new snow pillows or targeted manual measurements during extreme low-snow years.

Chapter 5 is based on a field campaign targeting post-fire hydrology with spatial and burn severity variance to understand how the representativeness of California's snow measurements were impacted by fire. Climate change and human fire suppression are increasing the frequency and severity of fires Williams et al., 2019, especially in those ecosystems adapted to frequent fire. This has a significant impact on snow hydrology and physics for years to decades after a fire. However, the character and magnitude of these changes are poorly understood: field observations in different locations often tell contradictory tales because they

fail to account for the dependence of post-fire hydrology response to topography, latitude, and vegetation. The results show that within the same fire, some mesoregions benefited from fire while others suffered. By comparing our field measurements and remote sensing data to established snow surveys, I identified a discrete shift in survey representativeness after the fire because burned areas gain and lose snow more quickly than unburned areas. Water management practices based on snow course observations in recently-burned forests should strongly consider short-term measurement expansion and update melt predictions to reflect the observed different post-fire snowpack responses. Finally, individual fires comprise a regime of fire effects and vegetation patterns from non-fire drivers. Broader management choices, such as wildland fire use policies, should continue to be studied for their hydrological outcomes with the goal of identifying place-specific land management choices that promote cultural, safety, ecological, and hydrologic goals at the same time.

6.3 Future work

Future work in this field should address the need to quantify the sensitivity of snow accumulation to warming temperatures. From the results in Chapters 2 and 3, we see that, while the overall impact of warming on snowpack is negative, sufficient regional, and local variability exists to show opposite-sign response in the same basin. Research using theoretical models and historical observations would enhance our understanding the balance between phase change and enhanced precipitation in a warmer atmosphere. Further, we must connect these outcomes to an additional driver of changing snowfall under climate change: atmospheric circulation influence on the occurrence and intensity of snow droughts and deluges. Additionally, future research should consider on the multi-reservoir nature of the water cycle as single-year snowpack as a water storage metric does not reflect the role of plants and soil as alternative partitionings of meltwater, nor of groundwater as a runoff source.

As more and more data become available, especially from remote sensing, there is a greater need to advance computational workflows to integrate higher data volumes with rapid environmental change. Chapter 4 introduced one example of a machine learning method's application to a snow prediction problem. Machine learning is a promising family of tools for this task, but should be approached with caution, as additional computing resources and training data can produce performance improvements without reflecting true predictability. Further, increasing the computational load of an operations problem should be justified to the resources available and the speed of the computation must not take longer than the necessary prediction window. Advancing applications-driven machine learning in snow hydrology should prioritize understanding how the structure of the machine learning algorithm matches the environmental process. Using explainability mapping techniques to propose new measurement sites for future climates complements and accelerates this area of work.

Bibliography

Abadi, M. et al. (2015). Tensorflow: Large-scale machine learning on heterogeneous systems [Software available from tensorflow.org]. https://www.tensorflow.org

Andradóttir, H. Ó., Arnardottir, A. R., & Zaqout, T. (2021). Rain on snow induced urban floods in cold maritime climate: Risk, indicators and trends. *Hydrological Processes*, *35*(9), e14298.

Aragon, C. M., & Hill, D. F. (2024). Changing snow water storage in natural snow reservoirs. *Hydrology and Earth System Sciences*, *28*(4), 781–800.

Argus, D. F., Landerer, F. W., Wiese, D. N., Martens, H. R., Fu, Y., Famiglietti, J. S., Thomas, B. F., Farr, T. G., Moore, A. W., & Watkins, M. M. (2017). Sustained water loss in California's mountain ranges during severe drought from 2012 to 2015 inferred from gps. *Journal of Geophysical Research: Solid Earth*, *122*(12), 10–559.

Attiwill, P., & Binkley, D. (2013). Exploring the mega-fire reality: A forest ecology and management conference. *Forest Ecology and Management*, *294*, 1–3.

Bales, R. C., Goulden, M. L., Hunsaker, C. T., Conklin, M. H., Hartsough, P. C., O'Geen, A. T., Hopmans, J. W., & Safeeq, M. (2018). Mechanisms controlling the impact of multi-year drought on mountain hydrology. *Scientific Reports*, *8*(1), 1–8.

Barnett, T. P., Adam, J. C., & Lettenmaier, D. P. (2005). Potential impacts of a warming climate on water availability in snow-dominated regions. *Nature*, *438*(7066), 303–309.

Barnhart, T. B. et al. (2016). Snowmelt rate dictates streamflow. *Geophys. Res. Lett.*, *43*, 8006–8016.

Barrett, A. (2003). National operational hydrologic remote sensing center snow data assimilation system (snodas) products at nsidc. *NSIDC Special Report 11*.

Belmecheri, S., Babst, F., Wahl, E. R., Stahle, D. W., & Trouet, V. (2016). Multi-century evaluation of Sierra Nevada snowpack. *Nature Climate Change*, *6*(1), 2–3.

Berghuijs, W., Woods, R., & Hrachowitz, M. (2014). A precipitation shift from snow towards rain leads to a decrease in streamflow. *Nature Climate Change*, *4*(7), 583–586.

Bernal, A. A., Stephens, S. L., Collins, B. M., & Battles, J. J. (2022). Biomass stocks in California's fire-prone forests: Mismatch in ecology and policy. *Environmental Research Letters*, *17*(4), 044047.

Bohr, G. S., & Aguado, E. (2001). Use of April 1 SWE measurements as estimates of peak seasonal snowpack and total cold-season precipitation. *Water Resour. Res.*, *37*, 51–60.

Boisramé, G., Thompson, S., & Stephens, S. (2018). Hydrologic responses to restored wildfire regimes revealed by soil moisture-vegetation relationships. *Advances in Water Resources*, *112*, 124–146.

Boisramé, G., Thompson, S., Kelly, M., Cavalli, J., Wilkin, K., & Stephens, S. (2017). Vegetation change during 40 years of repeated managed wildfires in the Sierra Nevada, California. *Forest Ecology and Management*, *402*, 241–252.

Boisramé, G., Thompson, S., Tague, C., & Stephens, S. (2019). Restoring a natural fire regime alters the water balance of a Sierra Nevada catchment. *Water Resources Research*, *55*, 5751–5769.

Boon, S. (2012). Snow accumulation following forest disturbance. *Ecohydrology*, *5*(3), 279–285.

Bormann, K. J., Brown, R. D., Derksen, C., & Painter, T. H. (2018). Estimating snow-cover trends from space. *Nature Climate Change*, *8*(11), 924–928.

Boucher, O., Denvil, S., Levavasseur, G., Cozic, A., Caubel, A., Foujols, M.-A., Meurdesoif, Y., Balkanski, Y., Checa-Garcia, R., Hauglustaine, D., Bekki, S., & Marchand, M. (2021). IPSL IPSL-CM6A-LR-INCA model output prepared for CMIP6 CMIP historical. https://doi.org/https://doi.org/10.22033/ESGF/CMIP6.13601

Boucher, O., Denvil, S., Levavasseur, G., Cozic, A., Caubel, A., Foujols, M.-A., Meurdesoif, Y., Cadule, P., Devilliers, M., Dupont, E., & Lurton, T. (2019a). IPSL IPSL-CM6A-LR model output prepared for CMIP6 ScenarioMIP ssp245. https://doi.org/https://doi.org/10.22033/ESGF/CMIP6.5264

Boucher, O., Denvil, S., Levavasseur, G., Cozic, A., Caubel, A., Foujols, M.-A., Meurdesoif, Y., Cadule, P., Devilliers, M., Dupont, E., & Lurton, T. (2019b). IPSL IPSL-CM6A-LR model output prepared for CMIP6 ScenarioMIP ssp585. https://doi.org/https://doi.org/10.22033/ESGF/CMIP6.5271

Box, J. E., Colgan, W. T., Christensen, T. R., Schmidt, N. M., Lund, M., Parmentier, F.-J. W., Brown, R., Bhatt, U. S., Euskirchen, E. S., Romanovsky, V. E., et al. (2019). Key indicators of Arctic climate change: 1971–2017. *Environmental Research Letters*, *14*(4), 045010.

Bozkurt, D., Rojas, M., Boisier, J. P., & Valdivieso, J. (2018). Projected hydroclimate changes over andean basins in central Chile from downscaled CMIP5 models under the low and high emission scenarios. *Climatic Change*, *150*(3), 131–147.

Breiman, L. (2001). Random forests. *Mach. Learn.*, *45*, 5–32.

Brekke, L. D., Maurer, E. P., Anderson, J. D., Dettinger, M. D., Townsley, E. S., Harrison, A., & Pruitt, T. (2009). Assessing reservoir operations risk under climate change. *Water Resources Research*, *45*(4).

Broxton, P. D., Zeng, X., & Dawson, N. (2016). Why do global reanalyses and land data assimilation products underestimate snow water equivalent? *Journal of Hydrometeorology*, *17*(11), 2743–2761.

Broxton, P., Harpold, A., Biederman, J., Troch, P., Molotch, N., & Brooks, P. (2015). Quantifying the effects of vegetation structure on snow accumulation and ablation in mixed-conifer forests. *Ecohydrology*, *8*(6), 1073–1094.

Bruyère, C. L., Done, J. M., Holland, G. J., & Fredrick, S. (2014). Bias corrections of global models for regional climate simulations of high-impact weather. *Climate Dynamics*, *43*, 1847–1856.

Cayan, D. R., Das, T., Pierce, D. W., Barnett, T. P., Tyree, M., & Gershunov, A. (2010). Future dryness in the southwest US and the hydrology of the early 21st century drought. *Proceedings of the National Academy of Sciences*, *107*(50), 21271–21276.

Chambolle, A. (2004). An algorithm for total variation minimization and applications. *J. Math. Imaging Vis.*, *20*, 89–97.

Changnon, S. A., & Kunkel, K. E. (2006). Changes in instruments and sites affecting historical weather records: A case study. *Journal of Atmospheric and Oceanic Technology*, *23*(6), 825–828.

Cho, E., McCrary, R. R., & Jacobs, J. M. (2021). Future changes in snowpack, snowmelt, and runoff potential extremes over North America. *Geophysical Research Letters*, *48*(22), e2021GL094985.

Christensen, N. S., Wood, A. W., Voisin, N., Lettenmaier, D. P., & Palmer, R. N. (2004). The effects of climate change on the hydrology and water resources of the Colorado River basin. *Climatic change*, *62*, 337–363.

Clow, D. W. (2010). Changes in the timing of snowmelt and streamflow in Colorado: A response to recent warming. *J. Clim.*, *23*, 2293–2306.

Cohen, J. L., Furtado, J. C., Barlow, M. A., Alexeev, V. A., & Cherry, J. E. (2012). Arctic warming, increasing snow cover and widespread boreal winter cooling. *Environmental Research Letters*, *7*(1), 014007.

Collins, B. M., & Stephens, S. L. (2010). Stand-replacing patches within a mixed severity fire regime: Quantitative characterization using recent fires in a long-established natural fire area. *Landscape Ecology*, *25*, 927–939.

Cook, B. I., Mankin, J. S., & Anchukaitis, K. J. (2018). Climate change and drought: From past to future. *Curr. Clim. Change Rep.*, *4*, 164–179.

Coppola, E., Raffaele, F., & Giorgi, F. (2018). Impact of climate change on snow melt driven runoff timing over the alpine region. *Climate Dynamics*, *51*(3), 1259–1273.

Council, N. R. (2004). *Climate data records from environmental satellites: Interim report*. The National Academies Press, Washington, DC.

Cowherd, M., Leung, L. R., & Girotto, M. (2023). Evolution of global snow drought characteristics from 1850 to 2100. *Environ. Res. Lett.*, *18*, 064043.

Cowherd, M., Mital, U., Rahimi, S., Girotto, M., Schwartz, A., & Feldman, D. (2024). Climate change-resilient snowpack estimation in the western United States. *Communications Earth & Environment*, *5*(1), 337.

Crumley, R., Palomaki, R., Nolin, A., Sproles, E., & Mar, E. (2020). SnowCloudMetrics: Snow information for everyone. *Remote Sensing*, *12*(20), 3341.

Cui, G., Anderson, M., & Bales, R. M. (2023). Mapping of snow water equivalent by a deep-learning model assimilating snow observations. *J. Hydrol.*, *616*, 128835.

Dai, A. (2008). Temperature and pressure dependence of the rain-snow phase transition over land and ocean. *Geophysical Research Letters*, *35*(12).

Daly, C. et al. (2008). Physiographically sensitive mapping of climatological temperature and precipitation across the conterminous United States. *Int. J. Climatol.*, *28*, 2031–2064.

Daly, C., Conklin, D. R., & Unsworth, M. H. (2010). Local atmospheric decoupling in complex topography alters climate change impacts. *International Journal of Climatology*, *30*(12), 1857–1864.

Danabasoglu, G. (2019a). NCAR CESM2 model output prepared for CMIP6 CMIP historical. https://doi.org/10.22033/ESGF/CMIP6.7627

Danabasoglu, G. (2019b). NCAR CESM2 model output prepared for CMIP6 ScenarioMIP ssp370. https://doi.org/10.22033/ESGF/CMIP6.7753

Danabasoglu, G. (2019c). NCAR CESM2-WACCM model output prepared for CMIP6 ScenarioMIP ssp245. https://doi.org/https://doi.org/10.22033/ESGF/CMIP6.10101

Danabasoglu, G. (2019d). NCAR CESM2-WACCM model output prepared for CMIP6 ScenarioMIP ssp585. https://doi.org/https://doi.org/10.22033/ESGF/CMIP6.10115

Danabasoglu, G. (2019e). NCAR CESM2-WACCM-FV2 model output prepared for CMIP6 CMIP historical. https://doi.org/https://doi.org/10.22033/ESGF/CMIP6.11298

de Boer, G. et al. (2023). Supporting advancement in weather and water prediction in the Upper Colorado river basin: The SPLASH campaign. *Bull. Am. Meteorol. Soc.*, *104*, E1853–E1874.

Dierauer, J. R., Allen, D. M., & Whitfield, P. H. (2019). Snow drought risk and susceptibility in the western United States and southwestern Canada. *Water Resources Research*, *55*(4), 3076–3091.

Dierauer, J. R., Allen, D., & Whitfield, P. (2021). Climate change impacts on snow and streamflow drought regimes in four ecoregions of British Columbia. *Canadian Water Resources Journal/Revue canadienne des ressources hydriques*, *46*(4), 168–193.

Dierauer, J. R., Whitfield, P. H., & Allen, D. M. (2018). Climate controls on runoff and low flows in mountain catchments of WesternNorth America. *Water Resources Research*, *54*(10), 7495–7510.

Dix, M., Bi, D., Dobrohotoff, P., Fiedler, R., Harman, I., Law, R., Mackallah, C., Marsland, S., O'Farrell, S., Rashid, H., Srbinovsky, J., Sullivan, A., Trenham, C., Vohralik, P., Watterson, I., Williams, G., Woodhouse, M., Bodman, R., Dias, F. B., ... Yang, R. (2019a). Csiro-arccss access-cm2 model output prepared for CMIP6 scenariomip ssp370. https://doi.org/10.22033/ESGF/CMIP6.4323

Dix, M., Bi, D., Dobrohotoff, P., Fiedler, R., Harman, I., Law, R., Mackallah, C., Marsland, S., O'Farrell, S., Rashid, H., Srbinovsky, J., Sullivan, A., Trenham, C., Vohralik, P., Watterson, I., Williams, G., Woodhouse, M., Bodman, R., Dias, F. B., ... Yang, R. (2019b). Csiro-arccss access-cm2 model output prepared for CMIP6 scenariomip ssp585. https://doi.org/10.22033/ESGF/CMIP6.4332

Dix, M., Bi, D., Dobrohotoff, P., Fiedler, R., Harman, I., Law, R., Mackallah, C., Marsland, S., O'Farrell, S., Rashid, H., Srbinovsky, J., Sullivan, A., Trenham, C., Vohralik, P., Watterson, I., Williams, G., Woodhouse, M., Bodman, R., Dias, F. B., ... Yang, R. (2019c). CSIRO-ARCCSS ACCESS-CM2 model output prepared for CMIP6 CMIP historical. https://doi.org/10.22033/ESGF/CMIP6.4271

Dix, M., Bi, D., Dobrohotoff, P., Fiedler, R., Harman, I., Law, R., Mackallah, C., Marsland, S., O'Farrell, S., Rashid, H., Srbinovsky, J., Sullivan, A., Trenham, C., Vohralik, P., Watterson, I., Williams, G., Woodhouse, M., Bodman, R., Dias, F. B., ... Yang, R. (2019d). CSIRO-ARCCSS ACCESS-CM2 model output prepared for CMIP6 ScenarioMIP ssp245. https://doi.org/10.22033/ESGF/CMIP6.4321

Dix, M., Bi, D., Dobrohotoff, P., Fiedler, R., Harman, I., Law, R., Mackallah, C., Marsland, S., O'Farrell, S., Rashid, H., Srbinovsky, J., Sullivan, A., Trenham, C., Vohralik, P., Watterson, I., Williams, G., Woodhouse, M., Bodman, R., Dias, F. B., ... Yang, R. (2019e). CSIRO-ARCCSS ACCESS-CM2 model output prepared for CMIP6 ScenarioMIP ssp585. https://doi.org/https://doi.org/10.22033/ESGF/CMIP6.4332

Dozier, J., Bair, E. H., & Davis, R. E. (2016). Estimating the spatial distribution of snow water equivalent in the world's mountains. *Wiley Interdisciplinary Reviews: Water*, *3*(3), 461–474.

EC-Earth-Consortium. (2019a). EC-Earth-Consortium EC-Earth3 model output prepared for CMIP6 CMIP historical. https://doi.org/10.22033/ESGF/CMIP6.4700

EC-Earth-Consortium. (2019b). EC-Earth-Consortium EC-Earth3 model output prepared for CMIP6 ScenarioMIP ssp370. https://doi.org/10.22033/ESGF/CMIP6.4700

EC-Earth-Consortium. (2019c). EC-Earth-Consortium EC-Earth3-Veg model output prepared for CMIP6 ScenarioMIP ssp370. https://doi.org/10.22033/ESGF/CMIP6.4886

EC-Earth-Consortium. (2020). EC-Earth-Consortium EC-Earth3-Veg-LR model output prepared for CMIP6 CMIP historical. https://doi.org/10.22033/ESGF/CMIP6.4707

Ekström, M., Grose, M. R., & Whetton, P. H. (2015). An appraisal of downscaling methods used in climate change research. *Wiley Interdisciplinary Reviews: Climate Change*, *6*(3), 301–319.

Emori, S., & Brown, S. (2005). Dynamic and thermodynamic changes in mean and extreme precipitation under changed climate. *Geophysical Research Letters*, *32*(17).

Errico, R. M., & Prive, N. C. (2018). *Some general and fundamental requirements for designing observing system simulation experiments (osses)* (tech. rep. GSFC-E-DAA-TN69069). World Meteorological Organization.

Eyring, V., Bony, S., Meehl, G. A., Senior, C. A., Stevens, B., Stouffer, R. J., & Taylor, K. E. (2016). Overview of the Coupled Model Intercomparison Project phase 6 (CMIP6) experimental design and organization. *Geoscientific Model Development*, *9*(5), 1937–1958.

Fang, Y., Liu, Y., Li, D., Sun, H., & Margulis, S. A. (2023). Spatiotemporal snow water storage uncertainty in the midlatitude American Cordillera. *The Cryosphere*, *17*, 5175–5195.

Fang, Y., Liu, Y., & Margulis, S. A. (2022). A western United States snow reanalysis dataset over the Landsat era from water years 1985 to 2021. *Scientific Data*, *9*(1), 677.

Feldman, D. R. et al. (2023). The Surface Atmosphere Integrated Field Laboratory (SAIL) campaign. *Bull. Am. Meteorol. Soc.*, *104*, E2192–E2222.

Finnegan, J. M., & Miller, J. R. (2022). Elevation dependence of projected hydro-climatic change in eastern Siberia. *Environmental Research Letters*, *17*(11), 114002.

Fleming, S. W., Vesselinov, V. V., & Goodbody, A. G. (2021). Augmenting geophysical interpretation of data-driven operational water supply forecast modeling for a western US river using a hybrid machine learning approach. *J. Hydrol.*, *597*, 126327.

Flint, L. E., Flint, A. L., Mendoza, J., Kalansky, J., & Ralph, F. (2018). Characterizing drought in California: New drought indices and scenario-testing in support of resource management. *Ecological processes*, *7*(1), 1–13.

Garen, D. C. (1992). Improved techniques in regression-based streamflow volume forecasting. *J. Water Resour. Plan. Manag.*, *118*. https://doi.org/10.1061/(ASCE)0733-9496(1992)118:6(654)

Georgakakos, A. P., Yao, H., Mullusky, M. G., & Georgakakos, K. P. (1998). Impacts of climate variability on the operational forecast and management of the Upper Des Moines River Basin. *Water Resour. Res.*, *34*, 799–821.

Gergel, D. R., Nijssen, B., Abatzoglou, J. T., Lettenmaier, D. P., & Stumbaugh, M. R. (2017). Effects of climate change on snowpack and fire potential in the western USA. *Climatic Change*, *141*(2), 287–299.

Gidden, M. J., Riahi, K., Smith, S. J., Fujimori, S., Luderer, G., Kriegler, E., Van Vuuren, D. P., Van Den Berg, M., Feng, L., Klein, D., et al. (2019). Global emissions pathways under different socioeconomic scenarios for use in CMIP6: A dataset of harmonized emissions trajectories through the end of the century. *Geoscientific model development*, *12*(4), 1443–1475.

Gleason, K. E., McConnell, J. R., Arienzo, M. M., Chellman, N., & Calvin, W. M. (2019). Four-fold increase in solar forcing on snow in western US burned forests since 1999. *Nature communications*, *10*(1), 2026.

Gleason, K. E., Nolin, A. W., & Roth, T. R. (2013). Charred forests increase snowmelt: Effects of burned woody debris and incoming solar radiation on snow ablation. *Geophysical Research Letters*, *40*(17), 4654–4661.

Good, P., Sellar, A., Tang, Y., Rumbold, S., Ellis, R., Kelley, D., & Kuhlbrodt, T. (2019). MOHC UKESM1.0-LL model output prepared for CMIP6 ScenarioMIP ssp370. https://doi.org/10.22033/ESGF/CMIP6.6347

Goss, M., Swain, D. L., Abatzoglou, J. T., Sarhadi, A., Kolden, C. A., Williams, A. P., & Diffenbaugh, N. S. (2020). Climate change is increasing the likelihood of extreme autumn wildfire conditions across California. *Environmental Research Letters*, *15*(9), 094016.

Gottlieb, A. R., & Mankin, J. S. (2021). Observing, measuring, and assessing the consequences of snow drought. *Bulletin of the American Meteorological Society*.

Gottlieb, A. R., & Mankin, J. S. (2024). Evidence of human influence on Northern Hemisphere snow loss. *Nature*, *625*(7994), 293–300.

Gringorten, I. I. (1963). A plotting rule for extreme probability paper. *Journal of Geophysical Research*, *68*(3), 813–814.

Guo, H., John, J. G., Blanton, C., McHugh, C., Nikonov, S., Radhakrishnan, A., Rand, K., Zadeh, N. T., Balaji, V., Durachta, J., Dupuis, C., Menzel, R., Robinson, T., Underwood, S., Vahlenkamp, H., Bushuk, M., Dunne, K. A., Dussin, R., Gauthier,

P. P. G., ... Zhang, R. (2018a). NOAA-GFDL GFDL-CM4 model output historical. https://doi.org/https://doi.org/10.22033/ESGF/CMIP6.8594

Guo, H., John, J. G., Blanton, C., McHugh, C., Nikonov, S., Radhakrishnan, A., Rand, K., Zadeh, N. T., Balaji, V., Durachta, J., Dupuis, C., Menzel, R., Robinson, T., Underwood, S., Vahlenkamp, H., Dunne, K. A., Gauthier, P. P. G., Ginoux, P., Griffies, S. M., ... Zhang, R. (2018b). NOAA-GFDL GFDL-CM4 model output prepared for CMIP6 ScenarioMIP ssp245. https://doi.org/https://doi.org/10.22033/ESGF/CMIP6.9263

Guo, H., John, J. G., Blanton, C., McHugh, C., Nikonov, S., Radhakrishnan, A., Rand, K., Zadeh, N. T., Balaji, V., Durachta, J., Dupuis, C., Menzel, R., Robinson, T., Underwood, S., Vahlenkamp, H., Dunne, K. A., Gauthier, P. P. G., Ginoux, P., Griffies, S. M., ... Zhang, R. (2018c). NOAA-GFDL GFDL-CM4 model output prepared for CMIP6 ScenarioMIP ssp585. https://doi.org/https://doi.org/10.22033/ESGF/CMIP6.9268

Hale, K. E., Jennings, K. S., Musselman, K. N., Livneh, B., & Molotch, N. P. (2023). Recent decreases in snow water storage in western North America. *Communications Earth & Environment*, *4*(1), 170.

Hall, A. (2004). The role of surface albedo feedback in climate. *Journal of climate*, *17*(7), 1550–1568.

Hall, D., & Riggs, G. (2021). MODIS/Terra Snow Cover Daily L3 Global 500m SIN Grid, version 61. https://doi.org/10.5067/MODIS/MOD10A1.061

Hanak, E., & Lund, J. R. (2012). Adapting California's water management to climate change. *Climatic Change*, *111*(1), 17–44.

Harpold, A., Dettinger, M. D., & Rajagopal, S. (2017). Defining snow drought and why it matters. *Eos*, *98*.

Harpold, A. A., & Brooks, P. D. (2018). Humidity determines snowpack ablation under a warming climate. *Proceedings of the National Academy of Sciences*, *115*(6), 1215–1220.

Hatchett, B. J., Koshkin, A., Guirguis, K., Rittger, K., Nolin, A. W., Heggli, A., Rhoades, A., A.E., E., Siirila-Woodburn, E., Brandt, W., & Gershunov, A. (2023). Midwinter dry spells amplify post-fire snowpack decline. *Geophysical Research Letters*, *50*(3), e2022GL101235.

Hatchett, B. J., & McEvoy, D. J. (2018). Exploring the origins of snow drought in the northern sierra nevada, California. *Earth Interactions*, *22*(2), 1–13.

Hawkins, E., & Sutton, R. (2011). The potential to narrow uncertainty in projections of regional precipitation change. *Climate dynamics*, *37*, 407–418.

He, C., Chen, F., Barlage, M., Liu, C., Newman, A., Tang, W., Ikeda, K., & Rasmussen, R. (2019). Can convection-permitting modeling provide decent precipitation for offline high-resolution snowpack simulations over mountains? *Journal of Geophysical Research: Atmospheres*, *124*(23), 12631–12654.

Hedrick, A. R. et al. (2018). Direct insertion of NASA Airborne Snow Observatory-derived snow depth time series into the iSnobal energy balance snow model. *Water Resour. Res.*, *54*, 8045–8063.

Heldmyer, A. J., Bjarke, N. R., & Livneh, B. (2023). A 21st-century perspective on snow drought in the Upper Colorado river basin. *JAWRA Journal of the American Water Resources Association*, *59*(2), 396–415.

Henderson, G. R., Peings, Y., Furtado, J. C., & Kushner, P. J. (2018). Snow–atmosphere coupling in the Northern Hemisphere. *Nature Climate Change*, *8*(11), 954–963.

Hernández-Henríquez, M. A., Déry, S. J., & Derksen, C. (2015). Polar amplification and elevation-dependence in trends of Northern Hemisphere snow cover extent, 1971–2014. *Environmental Research Letters*, *10*(4), 044010.

Hersbach, H. et al. (2020). The ERA5 global reanalysis. *Q. J. R. Meteorol. Soc.*, *146*, 1999–2049.

Hessburg, P. F., & Agee, J. K. (2003). An environmental narrative of inland northwest United States forests, 1800–2000. *Forest Ecology and Management*, *178*(1-2), 23–59.

Huning, L. S., & AghaKouchak, A. (2018). Mountain snowpack response to different levels of warming. *Proc. Natl Acad. Sci. USA*, *115*, 10932–10937.

Huning, L. S., & AghaKouchak, A. (2020). Global snow drought hot spots and characteristics. *Proceedings of the National Academy of Sciences*, *117*(33), 19753–19759.

Huss, M. et al. (2017). Toward mountains without permanent snow and ice. *Earth's Future*, *5*, 418–435.

Immerzeel, W. W., Lutz, A. F., Andrade, M., Bahl, A., Biemans, H., Bolch, T., Hyde, S., Brumby, S., Davies, B., Elmore, A., et al. (2020). Importance and vulnerability of the world's water towers. *Nature*, *577*(7790), 364–369.

Immerzeel, W. W., Van Beek, L. P., & Bierkens, M. F. (2010). Climate change will affect the Asian water towers. *science*, *328*(5984), 1382–1385.

Initiative, M. .-. M. R. (2015). Elevation-dependent warming in mountain regions of the world. *Nature Climate Change*, *5*(5), 424–430.

Jennings, K. S., Winchell, T. S., Livneh, B., & Molotch, N. P. (2018). Spatial variation of the rain–snow temperature threshold across the Northern Hemisphere. *Nature communications*, *9*(1), 1148.

John, J. G., Blanton, C., McHugh, C., Radhakrishnan, A., Rand, K., Vahlenkamp, H., Wilson, C., Zadeh, N. T., Dunne, J. P., Dussin, R., Horowitz, L. W., Krasting, J. P., Lin, P., Malyshev, S., Naik, V., Ploshay, J., Shevliakova, E., Silvers, L., Stock, C., ... Zeng, Y. (2018a). NOAA-GFDL GFDL-ESM4 model output prepared for CMIP6 ScenarioMIP ssp245. https://doi.org/https://doi.org/10.22033/ESGF/CMIP6.8686

John, J. G., Blanton, C., McHugh, C., Radhakrishnan, A., Rand, K., Vahlenkamp, H., Wilson, C., Zadeh, N. T., Dunne, J. P., Dussin, R., Horowitz, L. W., Krasting, J. P., Lin, P., Malyshev, S., Naik, V., Ploshay, J., Shevliakova, E., Silvers, L., Stock, C., ... Zeng, Y. (2018b). NOAA-GFDL GFDL-ESM4 model output prepared for CMIP6 ScenarioMIP ssp585. https://doi.org/https://doi.org/10.22033/ESGF/CMIP6.8706

Jordan, R. E. (1991). *A one-dimensional temperature model for a snow cover: Technical documentation for sntherm. 89*. Cold Regions Research; Engineering Laboratory (US).

Kampf, S. K., McGrath, D., Sears, M. G., Fassnacht, S. R., Kiewiet, L., & Hammond, J. C. (2022). Increasing wildfire impacts on snowpack in the western US. *Proceedings of the National Academy of Sciences*, *119*(39), e2200333119.

Kim, J., Waliser, D. E., Neiman, P. J., Guan, B., Ryoo, J.-M., & Wick, G. A. (2013). Effects of atmospheric river landfalls on the cold season precipitation in California. *Climate dynamics*, *40*, 465–474.

Knight, C. A., Anderson, L., Bunting, M. J., Champagne, M., Clayburn, R. M., Crawford, J. N., Klimaszewski-Patterson, A., Knapp, E. E., Lake, F. K., Mensing, S. A., et al. (2022). Land management explains major trends in forest structure and composition over the last millennium in California's Klamath Mountains. *Proceedings of the National Academy of Sciences*, *119*(12), e2116264119.

Koivusalo, H., & Kokkonen, T. (2002). Snow processes in a forest clearing and in a coniferous forest. *Journal of Hydrology*, *262*(1-4), 145–164.

Konapala, G., Mishra, A. K., Wada, Y., & Mann, M. E. (2020). Climate change will affect global water availability through compounding changes in seasonal precipitation and evaporation. *Nature Communications*, *11*(1), 3044.

Koshkin, A. L., Hatchett, B. J., & Nolin, A. W. (2022). Wildfire impacts on western United States snowpacks. *Frontiers in Water*, *4*, 971271.

Kostadinov, T. S. et al. (2019). Watershed-scale mapping of fractional snow cover under conifer forest canopy using lidar. *Remote Sens. Environ.*, *222*, 34–49.

Kouki, K., Räisänen, P., Luojus, K., Luomaranta, A., & Riihelä, A. (2022). Evaluation of Northern Hemisphere snow water equivalent in CMIP6 models during 1982–2014. *The Cryosphere*, *16*(3), 1007–1030.

Kraaijenbrink, P. D., Stigter, E. E., Yao, T., & Immerzeel, W. W. (2021). Climate change decisive for Asia's snow meltwater supply. *Nature Climate Change*, *11*(7), 591–597.

Krasting, J. P., Broccoli, A. J., Dixon, K. W., & Lanzante, J. R. (2013). Future changes in Northern Hemisphere snowfall. *Journal of Climate*, *26*(20), 7813–7828.

Krasting, J. P., John, J. G., Blanton, C., McHugh, C., Nikonov, S., Radhakrishnan, A., Rand, K., Zadeh, N. T., Balaji, V., Durachta, J., Dupuis, C., Menzel, R., Robinson, T., Underwood, S., Vahlenkamp, H., Dunne, K. A., Gauthier, P. P. G., Ginoux, P., Griffies, S. M., ... Zhao, M. (2018). NOAA-GFDL GFDL-ESM4 model output prepared for CMIP6 CMIP historical. https://doi.org/https://doi.org/10.22033/ESGF/CMIP6.8597

LANDFIRE. (2022). Landfire forest canopy cover layer.

Lapp, S., Byrne, J., Townshend, I., & Kienzle, S. (2005). Climate warming impacts on snowpack accumulation in an alpine watershed. *International Journal of Climatology: A Journal of the Royal Meteorological Society*, *25*(4), 521–536.

Leung, L. R., & Ghan, S. J. (1998). Parameterizing subgrid orographic precipitation and surface cover in climate models. *Monthly Weather Review*, *126*(12), 3271–3291.

Li, D., Lettenmaier, D. P., Margulis, S. A., & Andreadis, K. (2019a). The value of accurate high-resolution and spatially continuous snow information to streamflow forecasts. *Journal of Hydrometeorology*, *20*(4), 731–749.

Li, D., Wrzesien, M. L., Durand, M., Adam, J., & Lettenmaier, D. P. (2017). How much runoff originates as snow in the western United States, and how will that change in the future? *Geophysical Research Letters*, *44*(12), 6163–6172.

Li, L., Yu, Y., Tang, Y., Lin, P., Xie, J., Song, M., Dong, L., Zhou, T., Liu, L., Wang, L., Pu, Y., Chen, X., Chen, L., Xie, Z., Liu, H., Zhang, L., Huang, X., Feng, T., Zheng, W., ... Wei, J. (2019b). CAS FGOALS-g3 model output prepared for CMIP6 CMIP historical. https://doi.org/10.22033/ESGF/CMIP6.3356

Li, L., Yu, Y., Tang, Y., Lin, P., Xie, J., Song, M., Dong, L., Zhou, T., Liu, L., Wang, L., Pu, Y., Chen, X., Chen, L., Xie, Z., Liu, H., Zhang, L., Huang, X., Feng, T., Zheng, W., ... Wei, J. (2019c). CAS FGOALS-g3 model output prepared for CMIP6 ScenarioMIP ssp370. https://doi.org/10.22033/ESGF/CMIP6.3480

Li, Z., Chen, Y., Li, Y., & Wang, Y. (2020). Declining snowfall fraction in the alpine regions, Central Asia. *Scientific reports*, *10*(1), 3476.

Lievens, H., Brangers, I., Marshall, H.-P., Jonas, T., Olefs, M., & De Lannoy, G. (2021). Sentinel-1 snow depth retrieval at sub-kilometer resolution over the European Alps. *The Cryosphere Discussions*, *2021*, 1–25.

Livneh, B., & Badger, A. M. (2020). Drought less predictable under declining future snowpack. *Nature Climate Change*, *10*(5), 452–458.

López-Moreno, J. I., Callow, N., McGowan, H., Webb, R., Schwartz, A., Bilish, S., Revuelto, J., Gascoin, S., Deschamps-Berger, C., & Alonso-González, E. (2024). Marginal snowpacks: The basis for a global definition and existing research needs. *Earth-Science Reviews*, 104751.

López-Moreno, J. I., Gascoin, S., Herrero, J., Sproles, E., Pons, M., Alonso-González, E., Hanich, L., Boudhar, A., Musselman, K. N., & Moliné, N. A. (2017). Different sensitivities of snowpacks to warming in mediterranean climate mountain areas. *Environmental Research Letters*, *12*(7), 074006.

López-Moreno, J. I., Pomeroy, J., Morán-Tejeda, E., Revuelto, J., Navarro-Serrano, F., Vidaller, I., & Alonso-González, E. (2021). Changes in the frequency of global high mountain rain-on-snow events due to climate warming. *Environmental Research Letters*, *16*(9), 094021.

Lundquist, J. D., Dickerson-Lange, S. E., Lutz, J. A., & Cristea, N. C. (2013). Lower forest density enhances snow retention in regions with warmer winters: A global framework developed from plot-scale observations and modeling. *Water Resources Research*, *49*(10), 6356–6370.

Lute, A. C., Abatzoglou, J. T., & Hegewisch, K. C. (2015). Projected changes in snowfall extremes and interannual variability of snowfall in the western United States. *Water Resour. Res.*, *51*, 960–972.

Mankin, J. S., Viviroli, D., Singh, D., Hoekstra, A. Y., & Diffenbaugh, N. S. (2015). The potential for snow to supply human water demand in the present and future. *Environmental Research Letters*, *10*(11), 114016.

Margulis, S. A., Cortés, G., Girotto, M., & Durand, M. (2016a). A landsat-era Sierra Nevada snow reanalysis (1985–2015). *Journal of Hydrometeorology*, *17*(4), 1203–1221.

Margulis, S. A., Cortés, G., Girotto, M., Huning, L. S., Li, D., & Durand, M. (2016b). Characterizing the extreme 2015 snowpack deficit in the Sierra Nevada (USA) and the implications for drought recovery. *Geophysical Research Letters*, *43*(12), 6341–6349.

Marshall, A. M., Abatzoglou, J. T., Link, T. E., & Tennant, C. J. (2019). Projected changes in interannual variability of peak snowpack amount and timing in the Western United States. *Geophys. Res. Lett.*, *46*, 8882–8892.

Marshall, A. M., Abatzoglou, J. T., Rahimi, S., Lettenmaier, D. P., & Hall, A. (2024). California's 2023 snow deluge: Contextualizing an extreme snow year against future climate change. *Proceedings of the National Academy of Sciences*, *121*(20), e2320600121.

Maxwell, J. D., Call, A., & Clair, S. B. S. (2019). Wildfire and topography impacts on snow accumulation and retention in montane forests. *Forest ecology and management*, *432*, 256–263.

McCabe, G. J., Wolock, D. M., Pederson, G. T., Woodhouse, C. A., & McAfee, S. (2017). Evidence that recent warming is reducing Upper Colorado river flows. *Earth Interact.*, *21*, 1–14.

McCabe, G. J., Clark, M. P., & Hay, L. E. (2007). Rain-on-snow events in the western united states. *Bulletin of the American Meteorological Society*, *88*(3), 319–328.

McGowan, H., Callow, J. N., Soderholm, J., McGrath, G., Campbell, M., & Zhao, J.-x. (2018). Global warming in the context of 2000 years of Australian alpine temperature and snow cover. *Scientific Reports*, *8*(1), 1–8.

Meehl, G. A., Senior, C. A., Eyring, V., Flato, G., Lamarque, J.-F., Stouffer, R. J., Taylor, K. E., & Schlund, M. (2020). Context for interpreting equilibrium climate sensitivity and transient climate response from the CMIP6 Earth system models. *Science Advances*, *6*(26), eaba1981.

Meehl, G. A., Stocker, T. F., Collins, W. D., Friedlingstein, P., Gaye, A. T., Gregory, J. M., Kitoh, A., Knutti, R., Murphy, J. M., Noda, A., Raper, S. C., Watterson, I. G., Weaver, A. J., & Zhao, Z. C. (2007). Global climate projections. chapter 10.

Meinshausen, M., Nicholls, Z. R., Lewis, J., Gidden, M. J., Vogel, E., Freund, M., Beyerle, U., Gessner, C., Nauels, A., Bauer, N., et al. (2020). The shared socio-economic pathway (SSP) greenhouse gas concentrations and their extensions to 2500. *Geoscientific Model Development*, *13*(8), 3571–3605.

Micheletty, P., Perrot, D., Day, G., & Rittger, K. (2022). Assimilation of ground and satellite snow observations in a distributed hydrologic model for water supply forecasting. *J. Am. Water Resour. Assoc.*, *58*, 1030–1048.

Miller, J. D., & Thode, A. E. (2007). Quantifying burn severity in a heterogeneous landscape with a relative version of the delta Normalized Burn Ratio (dNBR). *Remote Sensing of Environment*, *109*(1), 66–80.

Miller, J. D., Safford, H., Crimmins, M., & Thode, A. E. (2009). Quantitative evidence for increasing forest fire severity in the sierra nevada and southern Cascade Mountains, California and Nevada, USA. *Ecosystems*, *12*(1), 16–32.

Milly, P. C., Betancourt, J., Falkenmark, M., Hirsch, R. M., Kundzewicz, Z. W., Lettenmaier, D. P., & Stouffer, R. J. (2008). Stationarity is dead: Whither water management? *Science*, *319*(5863), 573–574.

Mital, U., Dwivedi, D., Brown, J. B., & Steefel, C. I. (2022a). Downscaled hyperresolution (400 m) gridded datasets of daily precipitation and temperature (2008–2019) for the East–Taylor subbasin (western United States). *Earth Syst. Sci. Data*, *14*, 4949–4966.

Mital, U., Dwivedi, D., Özgen-Xian, I., Brown, J. B., & Steefel, C. I. (2022b). Modeling spatial distribution of snow water equivalent by combining meteorological and satellite data with lidar maps. *Artif. Intell. Earth Syst.*, *1*, e220010.

Moeser, C. D., Broxton, P. D., Harpold, A., & Robertson, A. (2020). Estimating the effects of forest structure changes from wildfire on snow water resources under varying meteorological conditions. *Water Resources Research*, *56*(11), e2020WR027071.

Molotch, N. P., & Bales, R. C. (2005). Scaling snow observations from the point to the grid element: Implications for observation network design. *Water Resources Research*, *41*(11).

Molotch, N. P., & Bales, R. C. (2006). SNOTEL representativeness in the Rio Grande headwaters on the basis of physiographics and remotely sensed snow cover persistence. *Hydrological Processes: An International Journal*, *20*(4), 723–739.

Molotch, N. P., Brooks, P. D., Burns, S. P., Litvak, M., Monson, R. K., McConnell, J. R., & Musselman, K. (2009). Ecohydrological controls on snowmelt partitioning in mixed-conifer sub-alpine forests. *Ecohydrology: Ecosystems, Land and Water Process Interactions, Ecohydrogeomorphology*, *2*(2), 129–142.

Montoya, E. L., Dozier, J., & Meiring, W. (2014). Biases of April 1 snow water equivalent records in the sierra nevada and their associations with large-scale climate indices. *Geophys. Res. Lett.*, *41*, 5912–5918.

Mote, P. W. et al. (2018). Dramatic declines in snowpack in the western us. *Clim. Atmos. Sci.*, *1*, 2.

Mote, P. W. (2006). Climate-driven variability and trends in mountain snowpack in westernNorth America. *Journal of Climate*, *19*(23), 6209–6220.

Mudryk, L., Santolaria-Otín, M., Krinner, G., Ménégoz, M., Derksen, C., Brutel-Vuilmet, C., Brady, M., & Essery, R. (2020). Historical Northern Hemisphere snow cover trends and projected changes in the CMIP6 multi-model ensemble. *The Cryosphere*, *14*(7), 2495–2514.

Muñoz-Sabater, J., Dutra, E., Agustí-Panareda, A., Albergel, C., Arduini, G., Balsamo, G., Boussetta, S., Choulga, M., Harrigan, S., Hersbach, H., et al. (2021). ERA5-Land: A

state-of-the-art global reanalysis dataset for land applications. *Earth System Science Data*, *13*(9), 4349–4383.

Musselman, K. N. et al. (2018). Projected increases and shifts in rain-on-snow flood risk over western North America. *Nat. Clim. Change*, *8*, 808–812.

Musselman, K. N., Clark, M. P., Liu, C., Ikeda, K., & Rasmussen, R. (2017). Slower snowmelt in a warmer world. *Nature Climate Change*, *7*(3), 214–219.

Natural Resources Conservation Center. (2008). The history of snow survey and water supply forecasting. https://www.nrcs.usda.gov/sites/default/files/2022-09/History-Of-Snow-Survey.pdf

Nelson, K. J., Connot, J., Peterson, B., & Martin, C. (2013). The LANDFIRE refresh strategy: Updating the national dataset. *Fire Ecology*, *9*, 80–101.

North, M., Collins, B. M., & Stephens, S. (2012). Using fire to increase the scale, benefits, and future maintenance of fuels treatments. *Journal of Forestry*, *110*(7), 392–401.

O'Gorman, P. A. (2014). Contrasting responses of mean and extreme snowfall to climate change. *Nature*, *512*(7515), 416–418.

O'Gorman, P. A., & Schneider, T. (2009). The physical basis for increases in precipitation extremes in simulations of 21st-century climate change. *Proceedings of the National Academy of Sciences*, *106*(35), 14773–14777.

Oki, T., & Kanae, S. (2006). Global hydrological cycles and world water resources. *science*, *313*(5790), 1068–1072.

Ombadi, M., Risser, M. D., Rhoades, A. M., & Varadharajan, C. (2023). A warming-induced reduction in snow fraction amplifies rainfall extremes. *Nature*, *619*(7969), 305–310.

O'Neill, B. C. et al. (2016). The Scenario Model Intercomparison Project (ScenarioMIP) for CMIP6. *Geosci. Model Dev.*, *9*, 3461–3482.

O'Neill, B. C., Tebaldi, C., Van Vuuren, D. P., Eyring, V., Friedlingstein, P., Hurtt, G., Knutti, R., Kriegler, E., Lamarque, J.-F., Lowe, J., et al. (2016). The scenario model intercomparison project (ScenarioMIP) for CMIP6. *Geoscientific Model Development*, *9*(9), 3461–3482.

Overpeck, J. T., Meehl, G. A., Bony, S., & Easterling, D. R. (2011). Climate data challenges in the 21st century. *Science*, *331*(6018), 700–702.

Oyler, J. W., Ballantyne, A., Jencso, K., Sweet, M., & Running, S. W. (2015). Creating a topoclimatic daily air temperature dataset for the conterminous United States using homogenized station data and remotely sensed land skin temperature. *Int. J. Climatol.*, *35*, 2258–2279.

Pagano, T. C., Garen, D. C., Perkins, T. R., & Pasteris, P. A. (2009). Daily updating of operational statistical seasonal water supply forecasts for the western U.S. *J. Am. Water Resour. Assoc.*, *45*, 767–778.

Pagano, T., Garen, D., & Sorooshian, S. (2004). Evaluation of official western US seasonal water supply outlooks, 1922–2002. *Journal of Hydrometeorology*, *5*(5), 896–909.

Painter, T. H., Berisford, D. F., Boardman, J. W., Bormann, K. J., Deems, J. S., Gehrke, F., Hedrick, A., Joyce, M., Laidlaw, R., Marks, D., et al. (2016). The airborne snow observatory: Fusion of scanning lidar, imaging spectrometer, and physically-based

modeling for mapping snow water equivalent and snow albedo. *Remote Sensing of Environment*, *184*, 139–152.

Painter, T. H., Rittger, K., McKenzie, C., Slaughter, P., Davis, R. E., & Dozier, J. (2009). Retrieval of subpixel snow covered area, grain size, and albedo from MODIS. *Remote Sensing of Environment*, *113*(4), 868–879.

Palazzi, E., Mortarini, L., Terzago, S., & Von Hardenberg, J. (2019). Elevation-dependent warming in global climate model simulations at high spatial resolution. *Climate Dynamics*, *52*(5-6), 2685–2702.

Paul, M., LeDuc, S., Lassiter, M., Moorhead, L., Noyes, P., & Leibowitz, S. (2022). Wildfire induces changes in receiving waters: A review with considerations for water quality management. *Water Resources Research*, *58*(9), e2021WR030699.

Pavelsky, T. M., Sobolowski, S., Kapnick, S. B., & Barnes, J. B. (2012). Changes in orographic precipitation patterns caused by a shift from snow to rain. *Geophysical Research Letters*, *39*(18).

Pedregosa, F. et al. (2011). Scikit-learn: Machine learning in python. *J. Mach. Learn. Res.*, *12*, 2825–2830.

Pedro-Monzonís, M., Solera, A., Ferrer, J., Estrela, T., & Paredes-Arquiola, J. (2015). A review of water scarcity and drought indexes in water resources planning and management. *Journal of Hydrology*, *527*, 482–493.

Pfahl, S., O'Gorman, P. A., & Fischer, E. M. (2017). Understanding the regional pattern of projected future changes in extreme precipitation. *Nature Climate Change*, *7*(6), 423–427.

Pflug, J., & Lundquist, J. (2020). Inferring distributed snow depth by leveraging snow pattern repeatability: Investigation using 47 lidar observations in the Tuolumne watershed, Sierra Nevada, California. *Water Resources Research*, *56*(9), e2020WR027243.

Pomeroy, J., Gray, D., Hedstrom, N., & Janowicz, J. (2002). Prediction of seasonal snow accumulation in cold climate forests. *Hydrological Processes*, *16*(18), 3543–3558.

Pongratz, J., Hartung, K., Wieners, K.-H., Giorgetta, M., Jungclaus, J., Reick, C., Esch, M., Bittner, M., Legutke, S., Schupfner, M., Wachsmann, F., Gayler, V., Haak, H., de Vrese, P., Raddatz, T., Mauritsen, T., von Storch, J.-S., Behrens, J., Brovkin, V., ... Roeckner, E. (2019). MPI-M MPI-ESM1.2-LR model output prepared for CMIP6 LUMIP ssp370-ssp126Lu. https://doi.org/10.22033/ESGF/CMIP6.6696

Powers, J. G., Klemp, J. B., Skamarock, W. C., Davis, C. A., Dudhia, J., Gill, D. O., Coen, J. L., Gochis, D. J., Ahmadov, R., Peckham, S. E., et al. (2017). The weather research and forecasting model: Overview, system efforts, and future directions. *Bulletin of the American Meteorological Society*, *98*(8), 1717–1737.

Pradhan, R. K., Markonis, Y., Vargas Godoy, M. R., Villalba-Pradas, A., & Andreadis, K. M. (2022). Review of GPM IMERG performance: A global perspective. *Remote Sensing of Environment*, *268*, 112754.

Qin, Y., Abatzoglou, J. T., Siebert, S., Huning, L. S., AghaKouchak, A., Mankin, J. S., Hong, C., Tong, D., Davis, S. J., & Mueller, N. D. (2020). Agricultural risks from changing snowmelt. *Nature Climate Change*, *10*(5), 459–465.

Rahimi, S. et al. (2024a). An overview of the western United States dynamically downscaled dataset (wus-d3). *Geosci. Model Dev.*, *17*, 2265–2286.

Rahimi, S., Huang, L., Norris, J., Hall, A., Goldenson, N., Risser, M., Feldman, D. R., Lebo, Z. J., Dennis, E., & Thackeray, C. (2024b). Understanding the cascade: Removing GCM biases improves dynamically downscaled climate projections. *Geophysical Research Letters*, *51*(9), e2023GL106264.

Rahimi, S., Krantz, W., Lin, Y.-H., Bass, B., Goldenson, N., Hall, A., Lebo, Z. J., & Norris, J. (2022). Evaluation of a reanalysis-driven configuration of WRF4 over the western United States from 1980 to 2020. *Journal of Geophysical Research: Atmospheres*, *127*(4), e2021JD035699.

Rakhmatulina, E., Boisramé, G., Stephens, S. L., & Thompson, S. (2021). Hydrological benefits of restoring wildfire regimes in the sierra nevada persist in a warming climate. *Journal of Hydrology*, *593*, 125808.

Raleigh, M. S., & Small, E. E. (2017). Snowpack density modeling is the primary source of uncertainty when mapping basin-wide SWE with lidar. *Geophys. Res. Lett.*, *44*, 3700–3709.

Rango, A., & Martinec, J. (1995). Revisiting the degree-day method for snowmelt computations. *J. Am. Water Resour. Assoc.*, *31*, 657–669.

Rasmusson, E. M. (1967). Atmospheric water vapor transport and the water balance ofNorth America: Part I. characteristics of the water vapor flux field. *Monthly Weather Review*, *95*(7), 403–426.

Reis, W., McGrath, D., Elder, K., Kampf, S., & Rey, D. (2024). Quantifying aspect-dependent snowpack response to high-elevation wildfire in the Southern Rocky Mountains. *Water Resources Research*, *60*(9), e2023WR036539.

Rhoades, A. M., Hatchett, B. J., Risser, M. D., Collins, W. D., Bambach, N. E., Huning, L. S., McCrary, R., Siirila-Woodburn, E. R., Ullrich, P. A., Wehner, M. F., et al. (2022). Asymmetric emergence of low-to-no snow in the midlatitudes of the American cordillera. *Nature Climate Change*, 1–9.

Rhoades, A. M., Huang, X., Ullrich, P. A., & Zarzycki, C. M. (2016). Characterizing sierra nevada snowpack using variable-resolution cesm. *Journal of Applied Meteorology and Climatology*, *55*(1), 173–196.

Rhoades, A. M., Ullrich, P. A., & Zarzycki, C. M. (2018). Projecting 21st century snowpack trends in western USA mountains using variable-resolution CESM. *Climate Dynamics*, *50*(1), 261–288.

Riggs, G. A., Hall, D. K., & Salomonson, V. V. (1994). A snow index for the Landsat thematic mapper and moderate resolution imaging spectroradiometer. *Proc. IGARSS'94-1994 IEEE International Geoscience and Remote Sensing Symposium*, *4*, 1942–1944.

Risser, M. D., Rahimi, S., Goldenson, N., Hall, A., Lebo, Z. J., & Feldman, D. R. (2024). Is bias correction in dynamical downscaling defensible? *Geophysical Research Letters*, *51*(10), e2023GL105979.

Roberts-Pierel, B., Raleigh, M., & Kennedy, R. (2024). Tracking the evolution of snow drought in the US Pacific Northwest at variable scales. *Water Resources Research*, *60*(7), e2023WR034588.

Robinne, F.-N., Hallema, D. W., Bladon, K. D., Flannigan, M. D., Boisramé, G., Bréthaut, C. M., Doerr, S. H., Di Baldassarre, G., Gallagher, L. A., Hohner, A. K., et al. (2021). Scientists' warning on extreme wildfire risks to water supply. *Hydrological Processes*, *35*(5), e14086.

Ronneberger, O., Fischer, P., & Brox, T. (2015). U-net: Convolutional networks for biomedical image segmentation. *International Conference on Medical Image Computing and Computer-Assisted Intervention*, 234–241.

Roturier, S., & Roué, M. (2009). Of forest, snow and lichen: Sámi reindeer herders' knowledge of winter pastures in northern sweden. *Forest Ecology and Management*, *258*(9), 1960–1967.

Salomonson, V. V., & Appel, I. (2006). Development of the Aqua MODIS NDSI fractional snow cover algorithm and validation results. *IEEE Trans. Geosci. Remote Sens.*, *44*, 1747–1756.

Schneider, D. P., Deser, C., Fasullo, J., & Trenberth, K. E. (2013). Climate data guide spurs discovery and understanding. *Eos Transactions AGU*, *94*(13), 121–122.

Schneider, T. et al. (2023). Harnessing AI and computing to advance climate modelling and prediction. *Nat. Clim. Change*, *13*, 887–889.

Scholl, A. E., & Taylor, A. H. (2006). Regeneration patterns in old-growth red fir–western white pine forests in the northern Sierra Nevada, Lake Tahoe, USA. *Forest Ecology and Management*, *235*(1-3), 143–154.

Seferian, R. (2018). CNRM-CERFACS CNRM-ESM2-1 model output prepared for CMIP6 CMIP historical. https://doi.org/10.22033/ESGF/CMIP6.4068

Segura, C. (2021). Snow drought reduces water transit times in headwater streams. *Hydrological Processes*, *35*(12), e14437.

Serreze, M. C., Clark, M. P., Armstrong, R. L., McGinnis, D. A., & Pulwarty, R. S. (1999). Characteristics of the western United States snowpack from snowpack telemetry (SNOTEL) data. *Water Resources Research*, *35*(7), 2145–2160.

Sexstone, G. A., Clow, D. W., Fassnacht, S. R., Liston, G. E., Hiemstra, C. A., Knowles, J. F., & Penn, C. A. (2018). Snow sublimation in mountain environments and its sensitivity to forest disturbance and climate warming. *Water Resources Research*, *54*(2), 1191–1211.

Shim, S., Lim, Y.-J., Byun, Y.-H., Seo, J., Kwon, S., & Kim, B.-H. (2020). NIMS-KMA UKESM1.0-LL model output prepared for CMIP6 ScenarioMIP ssp245. https://doi.org/https://doi.org/10.22033/ESGF/CMIP6.8436

Shim, S., Lim, Y.-J., Byun, Y.-H., Seo, J., Kwon, S., & Kim, B.-H. (2021). NIMS-KMA UKESM1.0-LL model output prepared for CMIP6 ScenarioMIP ssp585. https://doi.org/https://doi.org/10.22033/ESGF/CMIP6.8457

Shiogama, H., Abe, M., & Tatebe, H. (2019a). MIROC MIROC6 model output prepared for CMIP6 ScenarioMIP ssp245. https://doi.org/https://doi.org/10.22033/ESGF/CMIP6.5746

Shiogama, H., Abe, M., & Tatebe, H. (2019b). MIROC MIROC6 model output prepared for CMIP6 ScenarioMIP ssp585. https://doi.org/https://doi.org/10.22033/ESGF/CMIP6.5771

Shrestha, R. R., Bonsal, B. R., Bonnyman, J. M., Cannon, A. J., & Najafi, M. R. (2021). Heterogeneous snowpack response and snow drought occurrence across river basins of northwestern North America under 1.0° c to 4.0° c global warming. *Climatic Change*, *164*(3), 1–21.

Siirila-Woodburn, E. R., Rhoades, A. M., Hatchett, B. J., Huning, L. S., Szinai, J., Tague, C., Nico, P. S., Feldman, D. R., Jones, A. D., Collins, W. D., et al. (2021). A low-to-no snow future and its impacts on water resources in the western United States. *Nature Reviews Earth & Environment*, *2*(11), 800–819.

Siler, N., & Roe, G. (2014). How will orographic precipitation respond to surface warming? an idealized thermodynamic perspective. *Geophysical Research Letters*, *41*(7), 2606–2613.

Staudinger, M., Stahl, K., & Seibert, J. (2014). A drought index accounting for snow. *Water Resources Research*, *50*(10), 7861–7872.

Stephens, S. L., Foster, D. E., Battles, J. J., Bernal, A. A., Collins, B. M., Hedges, R., Moghaddas, J. J., Roughton, A. T., & York, R. A. (2024). Forest restoration and fuels reduction work: Different pathways for achieving success in the Sierra Nevada. *Ecological Applications*, *34*(2), e2932.

Stephens, S. L., Lydersen, J. M., Collins, B. M., Fry, D. L., & Meyer, M. D. (2015). Historical and current landscape-scale ponderosa pine and mixed-conifer forest structure in the southern Sierra Nevada. *Ecosphere*, *6*(5), 1–63.

Stephens, S. L., Thompson, S., Boisramé, G., Collins, B. M., Ponisio, L. C., Rakhmatulina, E., Steel, Z. L., Stevens, J. T., van Wagtendonk, J. W., & Wilkin, K. (2021). Fire, water, and biodiversity in the Sierra Nevada: A possible triple win. *Environmental Research Communications*, *3*(8), 081004.

Stevens, J. T. (2017). Scale-dependent effects of post-fire canopy cover on snowpack depth in montane coniferous forests. *Ecological Applications*, *27*(6), 1888–1900.

Sturm, M., & Wagner, A. M. (2010). Using repeated patterns in snow distribution modeling: An Arctic example. *Water Resour. Res.*, *46*, W12549.

Sturm, M., Goldstein, M. A., & Parr, C. (2017). Water and life from snow: A trillion dollar science question. *Water Resources Research*, *53*(5), 3534–3544.

Swart, N. C., Cole, J. N., Kharin, V. V., Lazare, M., Scinocca, J. F., Gillett, N. P., Anstey, J., Arora, V., Christian, J. R., Jiao, Y., Lee, W. G., Majaess, F., Saenko, O. A., Seiler, C., Seinen, C., Shao, A., Solheim, L., von Salzen, K., Yang, D., ... Sigmond, M. (2019a). CCCma CanESM5 model output prepared for CMIP6 CMIP historical. https://doi.org/10.22033/ESGF/CMIP6.3610

Swart, N. C., Cole, J. N., Kharin, V. V., Lazare, M., Scinocca, J. F., Gillett, N. P., Anstey, J., Arora, V., Christian, J. R., Jiao, Y., Lee, W. G., Majaess, F., Saenko, O. A., Seiler, C., Seinen, C., Shao, A., Solheim, L., von Salzen, K., Yang, D., ... Sigmond, M. (2019b). CCCma CanESM5 model output prepared for CMIP6 ScenarioMIP ssp370. https://doi.org/10.22033/ESGF/CMIP6.3690

Tang, Y., Rumbold, S., Ellis, R., Kelley, D., Mulcahy, J., Sellar, A., Walton, J., & Jones, C. (2019a). MOHC UKESM1.0-LL model output prepared for CMIP6 CMIP historical. https://doi.org/https://doi.org/10.22033/ESGF/CMIP6.6113

Tang, Y., Rumbold, S., Ellis, R., Kelley, D., Mulcahy, J., Sellar, A., Walton, J., & Jones, C. (2019b). MOHC UKESM1.0-LL model output prepared for CMIP6 CMIP historical. https://doi.org/10.22033/ESGF/CMIP6.6113

Tatebe, H., & Watanabe, M. (2018). MIROC MIROC6 model output prepared for CMIP6 CMIP historical. https://doi.org/https://doi.org/10.22033/ESGF/CMIP6.5603

Teich, M., Becker, K. M., Raleigh, M. S., & Lutz, J. A. (2022). Large-diameter trees affect snow duration in post-fire old-growth forests. *Ecohydrology*, *15*(3), e2414.

Trenberth, K. E. (2011). Changes in precipitation with climate change. *Climate research*, *47*(1-2), 123–138.

Ukkola, A. M., De Kauwe, M. G., Roderick, M. L., Abramowitz, G., & Pitman, A. J. (2020). Robust future changes in meteorological drought in CMIP6 projections despite uncertainty in precipitation. *Geophysical Research Letters*, *47*(11), e2020GL087820.

Van der Walt, S. et al. (2014). Scikit-image: Image processing in python. *PeerJ*, *2*, e453.

Van Loon, A. F., & Van Lanen, H. A. (2012). A process-based typology of hydrological drought. *Hydrology and Earth System Sciences*, *16*(7), 1915–1946.

Vander Jagt, B., Lucieer, A., Wallace, L., Turner, D., & Durand, M. (2015). Snow depth retrieval with UAS using photogrammetric techniques. *Geosciences*, *5*, 264–285.

Varadharajan, C. et al. (2019). Challenges in building an end-to-end system for acquisition, management, and integration of diverse data from sensor networks in watersheds: Lessons from a Mountainous Community Observatory in East River, Colorado. *IEEE Access*, *7*, 182796–182813.

Varhola, A., Coops, N. C., Weiler, M., & Moore, R. D. (2010). Forest canopy effects on snow accumulation and ablation: An integrative review of empirical results. *Journal of Hydrology*, *392*(3-4), 219–233.

Vergara-Temprado, J., Ban, N., & Schär, C. (2021). Extreme sub-hourly precipitation intensities scale close to the Clausius-Clapeyron rate over Europe. *Geophysical Research Letters*, *48*(3), e2020GL089506.

Voldoire, A. (2019). CNRM-CERFACS CNRM-ESM2-1 model output prepared for CMIP6 ScenarioMIP ssp370. https://doi.org/10.22033/ESGF/CMIP6.4199

Vollenweider, P., & Günthardt-Goerg, M. S. (2005). Diagnosis of abiotic and biotic stress factors using the visible symptoms in foliage. *Environmental Pollution*, *137*(3), 455–465.

Vorosmarty, C. J., Green, P., Salisbury, J., & Lammers, R. B. (2000). Global water resources: Vulnerability from climate change and population growth. *Science*, *289*(5477), 284–288.

Walton, D., Berg, N., Pierce, D., Maurer, E., Hall, A., Lin, Y.-H., Rahimi, S., & Cayan, D. (2020). Understanding differences in California climate projections produced by dynamical and statistical downscaling. *Journal of Geophysical Research: Atmospheres*, *125*(19), e2020JD032812.

Wang, Y., Leung, L. R., McGREGOR, J. L., Lee, D.-K., Wang, W.-C., Ding, Y., & Kimura, F. (2004). Regional climate modeling: Progress, challenges, and prospects. *Journal of the Meteorological Society of Japan. Ser. II*, *82*(6), 1599–1628.

Webster, C., Rutter, N., Zahner, F., & Jonas, T. (2016). Modeling subcanopy incoming longwave radiation to seasonal snow using air and tree trunk temperatures. *Journal of Geophysical Research: Atmospheres*, *121*(3), 1220–1235.

Wieners, K.-H., Giorgetta, M., Jungclaus, J., Reick, C., Esch, M., Bittner, M., Legutke, S., Schupfner, M., Wachsmann, F., Gayler, V., Haak, H., de Vrese, P., Raddatz, T., Mauritsen, T., von Storch, J.-S., Behrens, J., Brovkin, V., Claussen, M., Crueger, T., ... Roeckner, E. (2019). MPI-M MPI-ESM1.2-LR model output prepared for CMIP6 CMIP historical. https://doi.org/10.22033/ESGF/CMIP6.6595

Williams, A. P., Abatzoglou, J. T., Gershunov, A., Guzman-Morales, J., Bishop, D. A., Balch, J. K., & Lettenmaier, D. P. (2019). Observed impacts of anthropogenic climate change on wildfire in California. *Earth's Future*, *7*(8), 892–910.

Williams, A. P., McKinnon, K. A., Anchukaitis, K. J., Gershunov, A., Varuolo-Clarke, A. M., Clemesha, R. E., & Liu, H. (2024). Anthropogenic intensification of cool-season precipitation is not yet detectable across the western United States. *Journal of Geophysical Research: Atmospheres*, *129*(12), e2023JD040537.

Wrzesien, M. L., Durand, M. T., Pavelsky, T. M., Kapnick, S. B., Zhang, Y., Guo, J., & Shum, C. K. (2018). A new estimate ofNorth American mountain snow accumulation from regional climate model simulations. *Geophysical Research Letters*, *45*(3), 1423–1432.

Wu, T., Chu, M., Dong, M., Fang, Y., Jie, W., Li, J., Li, W., Liu, Q., Shi, X., Xin, X., Yan, J., Zhang, F., Zhang, J., Zhang, L., & Zhang, Y. (2018). BCC BCC-CSM2MR model output prepared for CMIP6 CMIP historical. https://doi.org/https://doi.org/10.22033/ESGF/CMIP6.2948

Xin, X., Wu, T., Shi, X., Zhang, F., Li, J., Chu, M., Liu, Q., Yan, J., Ma, Q., & Wei, M. (2019a). BCC BCC-CSM2MR model output prepared for CMIP6 ScenarioMIP ssp245. https://doi.org/https://doi.org/10.22033/ESGF/CMIP6.3030

Xin, X., Wu, T., Shi, X., Zhang, F., Li, J., Chu, M., Liu, Q., Yan, J., Ma, Q., & Wei, M. (2019b). BCC BCC-CSM2MR model output prepared for CMIP6 ScenarioMIP ssp585. https://doi.org/https://doi.org/10.22033/ESGF/CMIP6.3050

Xu, Z., Han, Y., Tam, C.-Y., Yang, Z.-L., & Fu, C. (2021). Bias-corrected CMIP6 global dataset for dynamical downscaling of the historical and future climate (1979–2100). *Scientific Data*, *8*(1), 293.

Xue, Y., Janjic, Z., Dudhia, J., Vasic, R., & De Sales, F. (2014). A review on regional dynamical downscaling in intraseasonal to seasonal simulation/prediction and major factors that affect downscaling ability. *Atmospheric research*, *147*, 68–85.

Yamada, T. J., Farukh, M. A., Fukushima, T., Inatsu, M., Sato, T., Pokhrel, Y. N., & Oki, T. (2014). Extreme precipitation intensity in future climates associated with the clausius-clapeyron-like relationship. *Hydrological Research Letters*, *8*(4), 108–113.

You, Q., Zhang, Y., Xie, X., & Wu, F. (2019). Robust elevation dependency warming over the tibetan plateau under global warming of 1.5 c and 2 c. *Climate Dynamics*, *53*, 2047–2060.

Yukimoto, S., Koshiro, T., Kawai, H., Oshima, N., Yoshida, K., Urakawa, S., Tsujino, H., Deushi, M., Tanaka, T., Hosaka, M., Yoshimura, H., Shindo, E., Mizuta, R., Ishii, M., Obata, A., & Adachi, Y. (2019a). MRI MRI-ESM2.0 model output prepared for CMIP6 CMIP historical. https://doi.org/10.22033/ESGF/CMIP6.6842

Yukimoto, S., Koshiro, T., Kawai, H., Oshima, N., Yoshida, K., Urakawa, S., Tsujino, H., Deushi, M., Tanaka, T., Hosaka, M., Yoshimura, H., Shindo, E., Mizuta, R., Ishii, M., Obata, A., & Adachi, Y. (2019b). MRI MRI-ESM2.0 model output prepared for CMIP6 ScenarioMIP ssp245. https://doi.org/10.22033/ESGF/CMIP6.6910

Yukimoto, S., Koshiro, T., Kawai, H., Oshima, N., Yoshida, K., Urakawa, S., Tsujino, H., Deushi, M., Tanaka, T., Hosaka, M., Yoshimura, H., Shindo, E., Mizuta, R., Ishii, M., Obata, A., & Adachi, Y. (2019c). MRI MRI-ESM2.0 model output prepared for CMIP6 ScenarioMIP ssp585. https://doi.org/10.22033/ESGF/CMIP6.6929

Zhao, Z., Di, P., Chen, S.-h., Avise, J., Kaduwela, A., & DaMassa, J. (2020). Assessment of climate change impact over California using dynamical downscaling with a bias correction technique: Method validation and analyses of summertime results. *Climate Dynamics*, *54*(7-8), 3705–3728.

Zhu, X., Lee, S.-Y., Wen, X., Wei, Z., Ji, Z., Zheng, Z., & Dong, W. (2021). Historical evolution and future trend of Northern Hemisphere snow cover in CMIP5 and CMIP6 models. *Environmental Research Letters*, *16*(6), 065013.

Zuzel, J. F., & Cox, L. M. (1978). A review of operational water supply forecasting techniques in areas of seasonal snowcover. In B. A. Shafer (Ed.), *Proc. 46th annual western snow conference* (pp. 18–20). Colorado State University.

Appendix A

Supplementary material for Chapter 4

Table A.1: GCM specification used in the multi-model ensemble of bias-corrected, dynamically downscaled GCM solutions used in this work, including the equilibrium climate sensitivity (ECS Meehl et al., 2020) of each raw GCM. Full details and raw GCM references can be found in the original WUS-D3 release (Rahimi et al., 2024a).

GCM	Variant	ECS [K/2xCO_2]
ACCESS-CM2	r5i1p1f1	4.7
CANESM5	r1i1p2f1	5.6
CESM2	r11i1p1f1	5.3
CNRM-ESM2-1	r1i1p1f2	4.6
EC-EARTH3	r1i1p1f1	4.3
EC-EARTH3-VEG	r1i1p1f1	4.3
FGOALS-G3	r1i1p1f1	2.8
MPI-ESM1-2-LR	r7i1p1f1	2.8
UKESM1-0-LL	r2i1p1f2	5.3

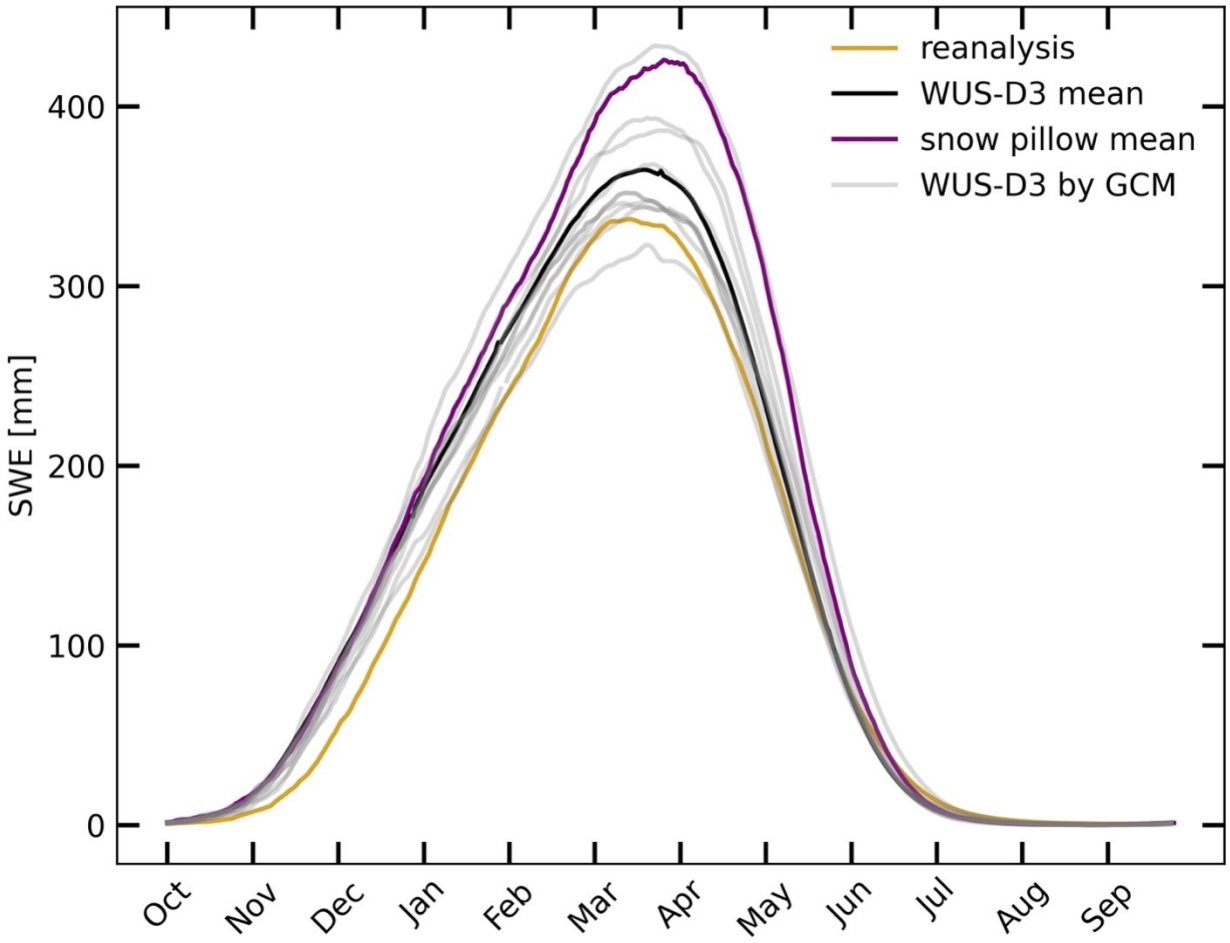

Figure A.1: Average daily snow water equivalent at WUS (excluding Alaska) SNOTEL stations from 1985-2014 from each individual WRF-downscaled GCM (gray), the multi-model mean of the WRF-downscaled GCMs (black), SNOTEL observations (purple), and the UCLA WUS reanalysis product (yellow). The WRF-downscaled GCMs and WUS reanalysis values are from the pixel of those respective products closest to each SNOTEL station.

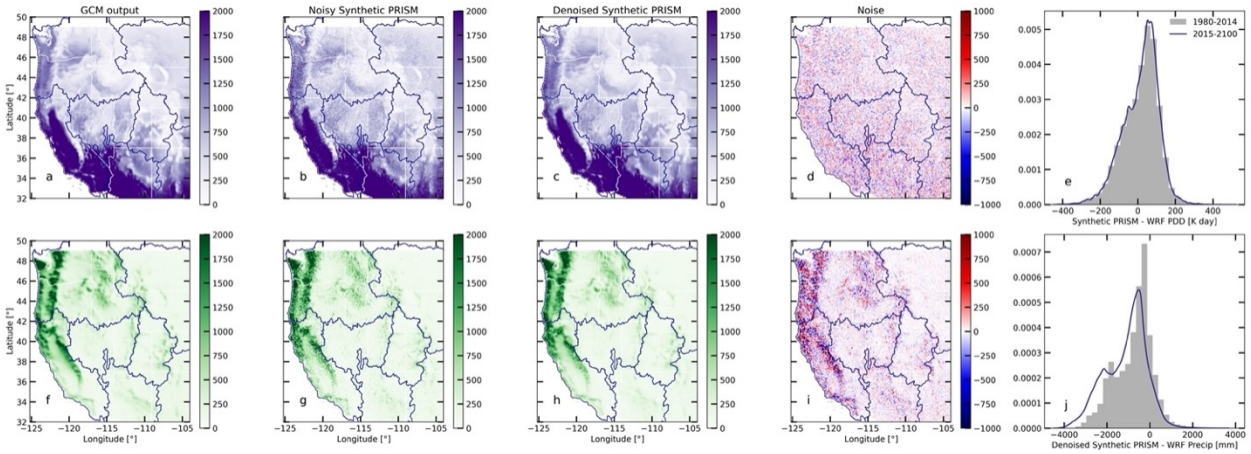

Figure A.2: Synthetic PRISM data generated from WUS-D3 solutions for temperature (top row, in units of positive degree days (°C starting October 1) and cumulative winter precipitation (bottom row, in units of mm starting October 1). Data shown are for 2001 as an example year with ACCESS-CM2 as the example GCM. Panels a and f show the WRF-downscaled GCM solution. The second column (b, g) shows the synthetic PRISM product with synthetic error added (see Methods). The third column (c, h) shows the final synthetic PRISM product after spatial denoising. The fourth column (d, i) shows the distribution of the synthetic noise, i.e., the difference between columns 3 and 2 (c-b, h-g). The fifth column (e, j) shows the distribution of pixel-wise differences between the final synthetic PRISM product (after denoising) and the original WUS-D3, for the historical experiment period (1980-2014) and the SSP3-7.0 experiment period (2015-2100).

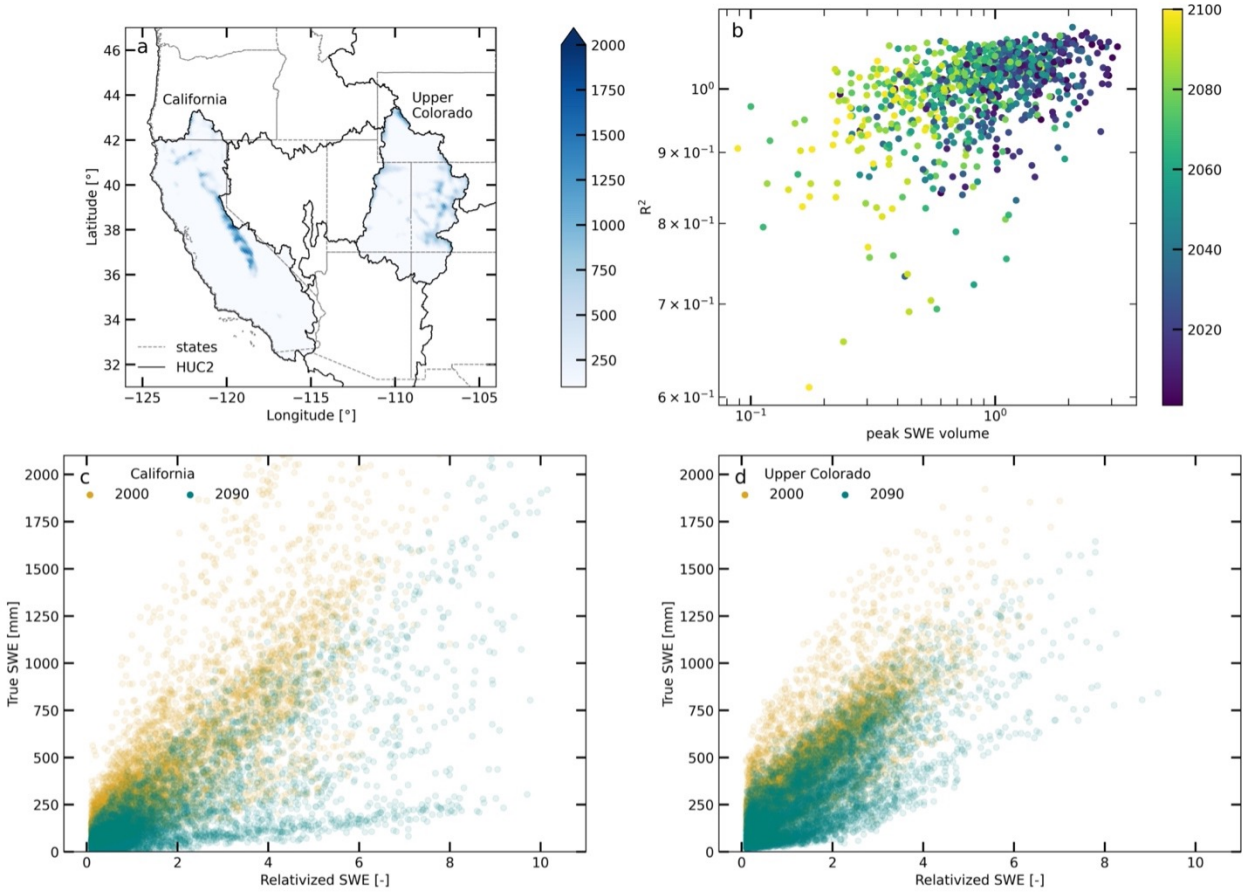

Figure A.3: Simulated (WUS-D3) peak SWE (a) in the California and Upper Colorado basins for an example year of 2000. For each basin, the true SWE [mm] is plotted as a function of relativized SWE [-] for 2000 and 2090; the spread of each distribution is proportional to the pattern repeatability as quantified by the R2 between the two for each GCM in the WUS-D3. Panel b shows the R^2 for each of the 9-GCM ensemble as a function of the sum of peak SWE for the year.

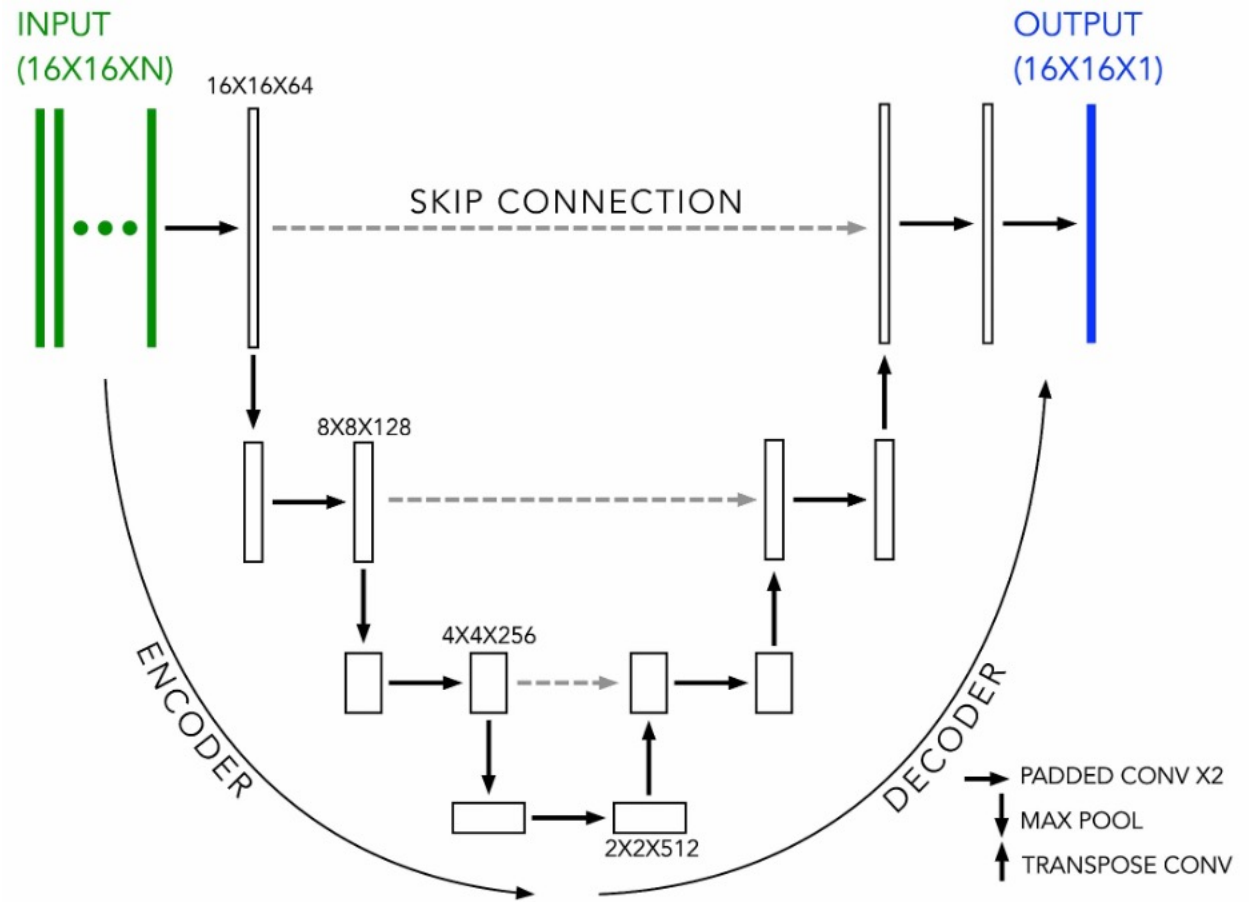

Figure A.4: U-Net architecture scheme using an example input of 16x16 pixels, and N predictors (true U-Net architecture varies with basin size). The architecture consists of three contractions and is otherwise identical to that of the original published method (Ronneberger et al., 2015). Dimensions of some intermediate layers are denoted in order to represent the scale of each contraction. Each arrow denotes a specific operation as indicated by the direction, with repeated padded convolutions indicated by right arrows, maximum pooling indicated by downward arrows, and transpose convolutions indicated by upward errors.

Appendix B

Supplementary material for Chapter 5

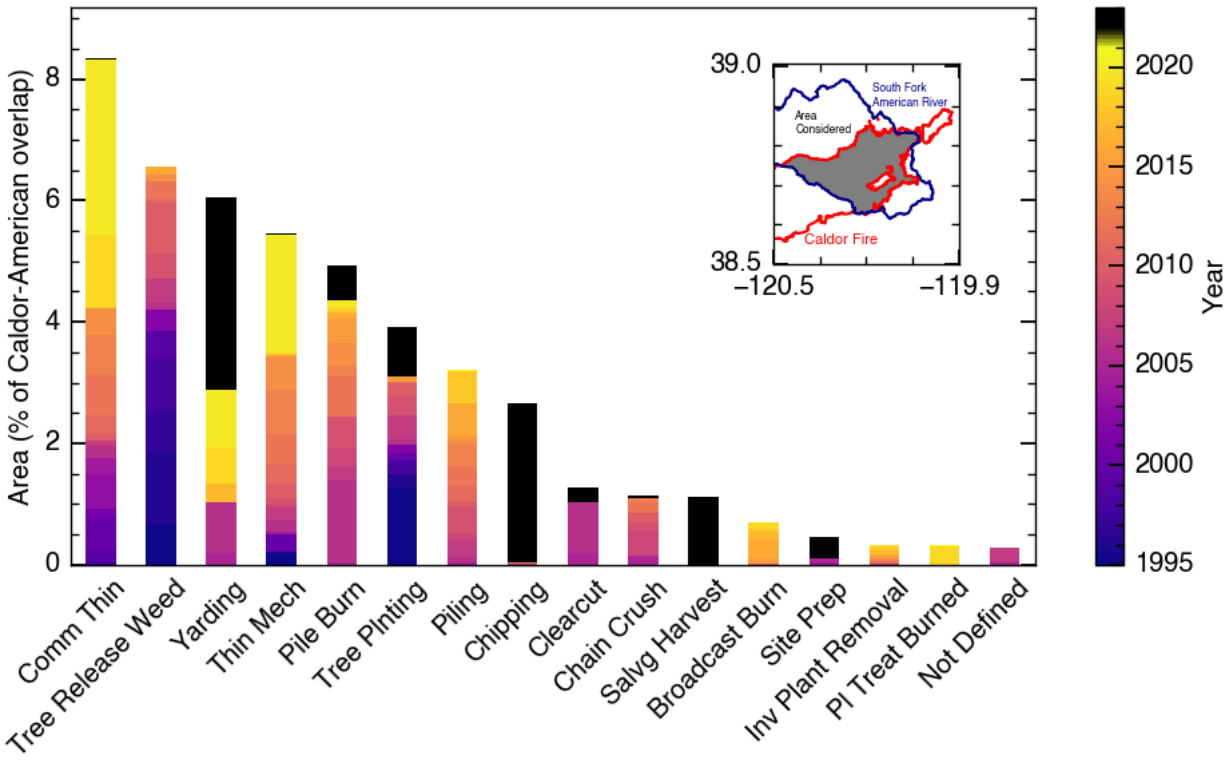

Figure B.1: Forest treatment reporting categories from FACTS from 1994-2024. Post-fire (2021-2024) contributions are shaded in black, all other years are indicated by the color scale. Values are reported as a percentage of the study area, indicated in the gray inset.

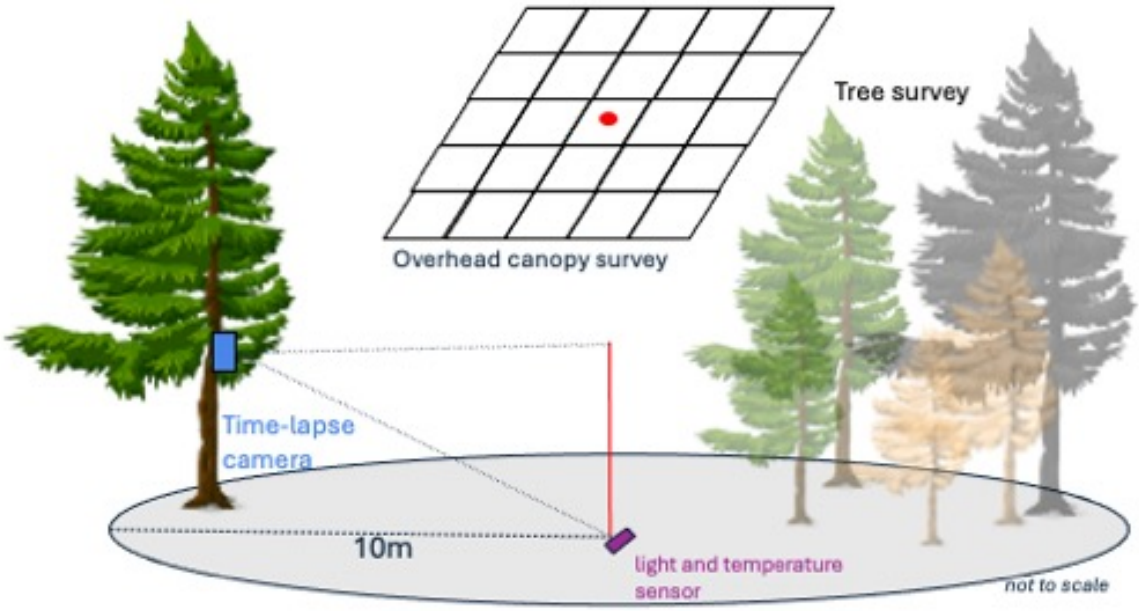

Figure B.2: Schematic of field plots showing time lapse camera and depth pole setup, placement of light and temperature sensor, and auxiliary measurements recorded when establishing the plot.

Figure B.3: Example photo from one time lapse image.

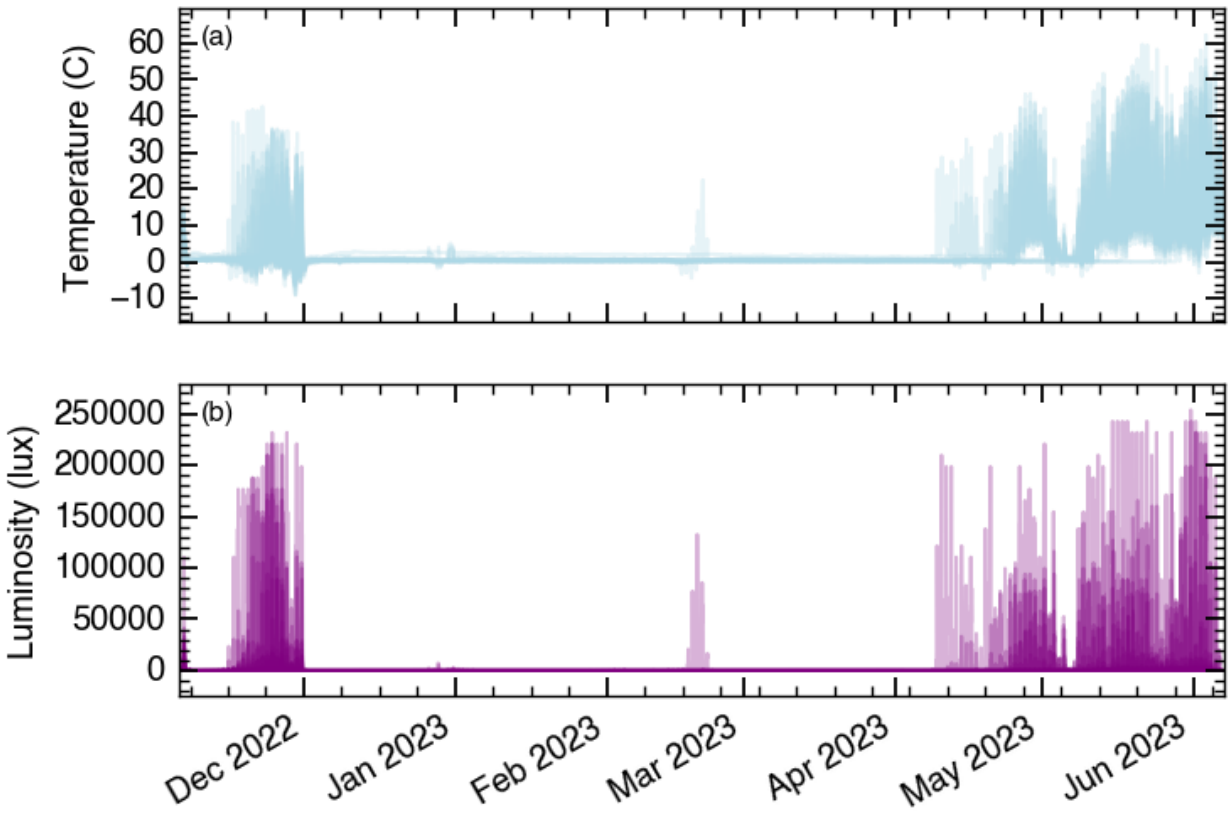

Figure B.4: All HOBO sensor time series of temperature (a) and luminosity (b) for the study period. For both timeseries, extended periods of low variance indicate that the sensor was covered by snow. Springtime increase in signal variance indicate the snow disappearance date at that sensor location.

Table B.1: Plot metadata. Latitude and longitude are in degrees, slope (θ) is in degrees, aspect (ψ) is in degrees, and elevation is in meters.

Plot	**Date In**	**Group**	**Lat.** [°]	**Lon.** [°]	θ [°]	ψ [°]	**Elev. [m]**
1	10/25/22	Strawberry E.	38.77565	-120.1182	11	201	2002
2	10/25/22	Strawberry E.	38.77497	-120.1163	16	186	2002
3	10/25/22	Strawberry E.	38.77201	-120.1156	9	207	1987
4	10/25/22	Strawberry E.	38.77374	-120.1148	17	210	1984
5	10/25/22	Strawberry E.	38.7716	-120.1417	11	201	1947
6	10/25/22	Strawberry W.	38.7697	-120.1212	5	30	1981
7	10/25/22	Strawberry W.	38.77089	-120.1224	13	0	1972
8	10/25/22	Strawberry W.	38.77397	-120.1215	18	7	1923
9	11/5/22	Audrain	38.81887	-120.0388	1	324	2251
10	11/5/22	Audrain	38.8188	-120.1087	3	254	2253
11	11/5/22	Audrain	38.8182	-120.0386	29	228	2248
12	11/5/22	Audrain	38.8167	-120.0376	21	209	2239
13	11/5/22	Pyramid	38.81379	-120.1366	21	228	2037
14	11/5/22	Pyramid	38.81385	-120.1367	21	227	2034
15	11/5/22	Pyramid	38.81472	-120.137	22	212	2051
16	11/5/22	Pyramid	38.81777	-120.1375	22	217	2164
17	11/5/22	Pyramid	38.81849	-120.1392	22	207	2183
18	11/5/22	Pyramid	38.81862	-120.1387	15	167	2183
19	11/5/22	Pyramid	38.81235	-120.1366	15	202	1988
20	11/6/22	Wrights	38.79422	-120.2371	14	102	1858
21	11/6/22	Wrights	38.79422	-120.2364	19	214	1867
22	11/6/22	Wrights	38.79414	-120.2364	8	195	1867
23	11/6/22	Wrights	38.79654	-120.2352	28	241	1995
24	11/6/22	Wrights	38.79452	-120.2341	24	235	1973
25	11/6/22	Wrights	38.79386	-120.2334	10	210	1979
26	11/6/22	Wrights	38.79367	-120.2333	17	232	1979

Table B.2: Plot tree survey data. Counts of live, red, and dead trees categorized as large (L; DBH $\geq$ 10 cm) or small (S; DBH $<$ 10 cm) and canopy reports of overhead coverage (0 = no cover, 1 = dead, 2 = red, 3 = live), reported following the grid in Figure S1 starting in the northwest corner of the grid.

	Live		**Red**		**Dead**		
Plot	**Large**	**Small**	**Large**	**Small**	**Large**	**Small**	**Canopy**
1	0	0	0	0	20	7	10100000000000000000010100
2	0	0	0	0	21	4	00000100100000000000101001
3	0	0	11	0	3	4	00002200020000000202020200
4	0	0	5	6	5	1	20200222000020002002002002
5	11	30	4	0	0	0	02000003323333333333333333
6	23	5	0	0	0	0	00220022222202222220020020
7	0	0	9	23	3	2	20022000200000000202002222
8	0	0	0	0	11	5	10011001001000010001011100
9	1	1	1	0	2	2	00000000000000000000000000
10	0	0	6	1	2	0	00000001020002220000000200
11	0	0	0	0	3	1	00000000000000000000000000
12	0	0	12	0	0	0	00022002220002200022000022
13	0	0	3	0	7	1	10000001100001000011110000
14	0	0	0	0	17	7	10010111101100010000010101
15	0	0	22	2	0	0	22222202222002222222222222
16	0	0	1	0	2	0	00000011000100001001100010
17	0	0	2	0	0	0	12222222220000000000000000
18	0	0	0	0	7	2	00100000100001001110001010
19	18	2	6	0	0	0	00000200000302233330333333
20	0	0	0	0	8	12	00000010110001100001000000
21	0	0	8	0	2	17	00220000000000000020000022
22	0	0	15	1	3	0	02000022202202220202002222
23	13	2	2	1	0	0	03333333333333333333333333
24	0	0	20	0	0	0	22222202220022222002222222
25	0	0	6	0	2	9	00000000000000000000000000
26	0	0	0	0	23	0	11101011011101101010011100